Acoustic Methods for Histotripsy Feedback

by

Jonathan J. Macoskey

A dissertation submitted in partial fulfillment
of the requirements for the degree of
Doctor of Philosophy
(Biomedical Engineering and Scientific Computing)
in the University of Michigan
2019

Doctoral Committee:

Associate Professor Zhen Xu, Chair
Professor Charles A. Cain
Dr. Timothy L. Hall
Associate Professor Eric Johnsen
Professor Eric Michielssen
Associate Professor Raj Rao Nadakuditi

My Heart is in the Work.

-Andrew Carnegie

Jonathan J. Macoskey

macoskey@umich.edu

ORCID iD: 0000-0002-2776-230X

Dedication

To the mentors who have guided me,

to the peers against which I have competed,

and to the students I have taught.

Acknowledgements

As alluded to in my dedication, there are many mentors, peers, and younger students who deserve my acknowledgement. I would first like to acknowledge my two most important mentors in graduate school: Zhen and Tim. Zhen Xu, my advisor, has not only supported all of my professional goals but also has given me the ability to have research autonomy that to my knowledge is unparalleled in graduate school. She has always been there when I need her, but has also given me the space to satisfy my academic curiosity when I desire. I was also fortunate to have virtually unlimited research resources, and she is to thank for that. Tim Hall, my long-term carpool buddy and number one technical mentor, has taught me everything I know about hardware development and so much more. Without him, much of the work in this dissertation would have been an impossibility for me to accomplish. His guidance and consistent morning schedule have undoubtedly been major contributors to my success and happiness in graduate school.

I wish to thank all of my peers who I have worked with throughout both undergrad and graduate school. My original BME homework crew at Rochester – Jarvis, Keith, Maura, Silverstein, and Katie – kept late nights in the stacks finishing up problem sets somehow really enjoyable. I also wish to thank some of my friends outside of the classroom including James, Sevi, Nick, Sharkey, Pat, Oliver, Mitchell, Bjorn, Russell, Kal, Rishi, Eleanor, and many, many others who continuously and successfully reminded me that there is indeed a life outside of the lab. Without all of these people, my graduate career in biomedical engineering may not have existed.

In the lab at Michigan, I have been fortunate to work alongside some of the brightest people I have ever met as mentors, peers, and students. Xi Zhang deserves a large amount of credit for

getting me up to speed with research at Michigan, and I wish to thank him for his guidance, kindness, and patience. You will be a friend to me for life. I wish to thank Kim Ives for all of her help making animal studies easy and providing many laughs during long and challenging days. I wish to, in particular, thank Jonathan Lundt and Tyler Gerhardson for making work feel less like a job as we all figured out how to be senior grad students. I would also like to thank each and every member of this lab with which I have had the pleasure of working: Eli Vlaisavljevich, Jonathan Sukovich, Steven Allen, Yige Li, Hedieh Tamaddoni, Sang Won Choi, Tejaswi Worlikar, Ryan Hubbard, Ellen Yeats, Ning Lu, and Greyson Stocker. This collection of names will undoubtedly be an impressive one in the future. You have all taught me so much and I thank you for your support.

I have also been very fortunate to have many supportive friends outside the lab here at Michigan who deserve my sincere thanks. In particular, Richard and Ignas, my long-term housemates, and Lauren and Lane, honorary housemates, helped make LBH a home and were always there when I needed them.

Finally, I would like to thank my parents for their undying love and support throughout everything. They have been a backbone of stability for each and every step along the way. They are my original mentors. I would also like to thank my sister for always showing me how to be adventurous and my Oma for always knowing what is truly best. Without the support of my family, none of this could have been possible.

Table of Contents

List of Tables

List of Figures

Abstract

Histotripsy is a therapeutic ultrasound modality that employs clouds of inertial cavitation to noninvasively destroy unwanted tissue. Histotripsy systems are, traditionally, transmit-only systems incapable of receiving ultrasound. For guidance, an ultrasound imaging probe is placed in the center of a histotripsy array. On B-mode ultrasound imaging, the region of tissue destruction appears as a hypoechoic zone after a substantial amount of treatment has occurred. However, this level of histotripsy feedback is insufficient for several reasons. First, histotripsy treatments occur in a 3D space, yet B-mode imaging is 2D. While 3D ultrasound imaging exists, the large footprint of 3D probes would occupy a substantial portion of the acoustic window for therapy. Second, histotripsy-treated lesions only appear hypoechoic on B-mode after a substantial amount of treatment has occurred resulting in poor sensitivity. Developing receive-capable histotripsy arrays would enable a multitude of feedback mechanisms. The overall objective of this dissertation is to develop receive-capable histotripsy systems and new feedback mechanisms enabled by this technology that improve histotripsy treatment efficacy and patient outcomes.

In the first part of this dissertation, the technical details associated with the development of receive-capable histotripsy systems are discussed. First, the challenges of designing highly-parallelized data acquisition systems that are capable of operating over a high dynamic range are outlined and solutions are proposed. Next, the various stages of prototypes that were developed are explored. Finally, two fully-functional receive-capable histotripsy systems are described in detail: a retrofit system that can enable receive-capability for any existing histotripsy system, and a new histotripsy system that incorporates receiver electronics in with high-voltage drivers.

In the second part of this dissertation, several feedback methods for monitoring the extent and progression of histotripsy treatment are discussed. In particular, a new feedback method is investigated, which uses the cavitation collapse time to monitor tissue damage. Upon initiation of a histotripsy bubble cloud, a series of shockwaves are emitted during its initial expansion. Once the bubble cloud expands to a maximum radius, it begins to collapse inward on itself, and, during the final stage of collapse, another shockwave is released. Using a receive-capable histotripsy array, these shockwaves can be acquired thus allowing for a measurement of the overall lifespan of the bubble cloud. This acoustic measurement is optically validated using a high-speed camera. It was found that this lifespan, defined by the cavitation collapse time, correlates directly with the extent of histotripsy treatment. *Ex vivo* bovine liver samples were treated, and it was found that the change in collapse time directly correlates with hepatocyte destruction.

In the final part of this dissertation, a receive-capable histotripsy system was used to implement acoustic aberration correction. Natural heterogeneities of tissue can result in upwards of 10% variation of sound speed throughout the acoustic path of propagation for histotripsy. These sound speed variations result in acoustic aberrations that significantly defocus histotripsy pulses through phase aberration and result in lowered focal pressure and treatment efficacy *in vivo*. By using a receive-capable histotripsy system to acquire the expansion shockwave construct from the initial expansion of the histotripsy bubble cloud, time reversal acoustics was implemented to correct for these acoustic aberrations and refocus subsequent histotripsy pulses. Using this method, over 20% of lost pressure due to phase aberration is recovered, and the histotripsy system power required to induce cavitation was reduced by approximately 31.5%.

CHAPTER 1

Introduction

This dissertation focuses on the investigation of acoustic feedback methods for histotripsy using the acoustic emissions from the cavitation bubble cloud used during histotripsy treatments. The medical applications for the research in this dissertation are primarily focused on the treatment of abdominal diseases such as liver cancer, but the technology and methods developed herein are applicable to all varieties histotripsy treatments as well as a number of other non-invasive ultrasonic therapy methods such as high-intensity focused ultrasound (HIFU). This research is separated into three categories: 1) technological development of histotripsy arrays that are capable of both transmitting and receiving ultrasound, 2) methods for acoustically monitoring the progression and extent of treatment progression, and 3) methods for implementing soft-tissue phase aberration correction for histotripsy to increase focal pressure when treating through heterogeneous overlying tissue. This chapter will provide a brief background into existing feedback methods for histotripsy and the difficulties with developing receive-capable histotripsy systems. This chapter will conclude with an outline of this dissertation, which provides a brief description of each chapter.

1.1. Histotripsy

Primary liver and intrahepatic bile duct cancers are diagnosed in 30,000-40,000 new patients every year in the United States with approximately 29,000 existing patients dying from these cancers each year [1], [2]. Similar morbidities exist with a large variety of other soft-tissue

abdominal cancers including pancreatic adenocarcinoma [3], renal cell carcinoma [4], colorectal cancer [5], and breast cancer [6] among many others. Current treatment strategies generally include radiation or chemical therapy, tumor resection via invasive surgery, or, in severe cases for some diseases, organ transplant [7]. There are also thermal-based ablation techniques, including radiofrequency, microwave, and ultrasound thermal ablation methods. However, these thermal methods have limitations such as unwanted heating of surrounding tissues [8] and adverse physiological effects such as skin toxicity (e.g., blisters or tracks) or edema at the treatment site [9]. There is a clear need for more effective non-invasive, non-ionizing, non-thermal soft-tissue cancer treatments.

Histotripsy is a therapeutic ultrasound technique that is ideally suited for treating health conditions in soft tissue in which a portion of tissue needs to be destroyed and/or removed [10]. Histotripsy has been investigated for the treatment of deep vein thrombosis [11], [12], liver tumors [13], benign prostatic hyperplasia [14], [15], congenital heart diseases [16], and transcranial brain applications [17]. Histotripsy uses high-intensity and highly focused ultrasound to initiate a cloud of inertially cavitating bubbles within soft tissue using a high peak-negative rarefactional pressure pulse in excess of 28 MPa under the intrinsic threshold mechanism [18]. This cavitating bubble cloud is used to fractionate unwanted target-tissue within the body [19]. Histotripsy has been shown to have significant advantages when compared to existing thermal ablation technologies including highly precise and accurate targeting [20], increased depth-of-penetration [21], and the fact that histotripsy is immune to the effects of natural heat sinks such as adjacent vessels [22]. However, there are two areas of technical advancements that could improve histotripsy. 1) Current real-time tissue assessment techniques have poor sensitivity and require additional equipment. 2) When treating through tissue, significant phase aberrations occur when ultrasound interacts with

tissue scatterers surrounding the target-tissue, which act to de-focus histotripsy thereby decreasing its accuracy and efficiency.

1.2. Feedback Mechanisms for Histotripsy

It is important to monitor both the location and size of the bubble cloud as well as the extent of tissue treatment during a histotripsy therapy session to ensure proper treatment. B-mode ultrasound is typically used during treatment to monitor the histotripsy bubble cloud, which appears as a dynamically changing hyperechoic zone [19], [23]. When substantial tissue liquefaction has occurred, the tissue appears to be hypoechoic on B-mode imaging [24]. However, this method is sub-optimal due to its low sensitivity, as the hypoechoic zone only occurs when substantial tissue fractionation is achieved [24]. Because the intensity of the tissue speckle varies across different tissues and patients, it is unlikely that a universal intensity threshold could be set to indicate complete tissue fractionation for different tissues and patients. Additionally, a 2D ultrasound imaging probe is currently used to view a 2D plane of tissue containing the geometric focus of the histotripsy transducer, which is not able to view the 3D volumes of ablation generated by histotripsy. Therefore, 3D ultrasound imaging would be desired and is available, but the large footprint of the 3D probe would occupy a substantial portion of the acoustic window for therapy. Ultrasound elastography, such as acoustic radiation force impulse (ARFI) imaging, has also been investigated to detect histotripsy lesion formation because histotripsy gradually fractionates the target-tissue to a liquid-appearing homogenate [25]-[28]. These elastography methods have been experimentally successful in detecting tissue fractionation with higher sensitivity than B-mode speckle intensity. However, as the tissue becomes more liquefied, the shear wave propagation used for elastography imaging techniques becomes increasingly restricted resulting in decreased accuracy of elastography measurements later in histotripsy treatment [26]. Additionally,

reflections from the histotripsy-induced cavitation nuclei are known to contribute to the radiation force used for ARFI imaging, which may introduce artifacts in the elastography methods [28].

Other medical imaging modalities, such as magnetic resonance imaging (MRI), have also been investigated for histotripsy feedback. In fact, magnetic resonance guided focused ultrasound (MRgFUS) has already been used to provide three-dimensional temperature maps as real-time feedback during high-intensity focused ultrasound (HIFU) thermal treatments [29, 30, 31], and it has been approved by the FDA to treat several conditions including essential tremor [32], uterine fibroids [33], and prostate cancer [34]. However, MRI-guidance for histotripsy would require MRI-compatible histotripsy arrays as well as procedural MRI scanners. MRI-compatible histotripsy arrays are currently under development, but requiring an MRI scanner to be operated during all histotripsy treatments would drastically increase the cost of histotripsy. Furthermore, MRI still is incapable of accurately understanding the acoustic properties of tissue, and its real-time capabilities are limited depending on the desired resolution and field-of-view.

Recently, a new modality called bubble induced color Doppler (BCD) has been employed to monitor histotripsy-induced tissue fractionation in real-time [35] [36]. This method uses Doppler ultrasound on a conventional clinical ultrasound machine to obtain velocity estimations of the residual nuclei that persist after cavitation. It is thought that the movement of these residual nuclei in the treated tissue corresponds to the level of tissue fractionation. However, a solidified understanding of the underlying mechanisms behind this metric has remained elusive, and the Doppler signal is highly dependent on the characteristics of the histotripsy transducer. Additionally, both elastography and BCD techniques are 2D imaging methods that do not provide the desired 3D treatment mapping. Furthermore, all of these available technologies require additional imaging equipment, which reduces the available acoustic window for histotripsy.

Therefore, there is a need for a non-invasive tissue integrity monitoring technique that is able to monitor therapy in 3D with high sensitivity and without reducing the acoustic window for therapy.

In addition to the type of histotripsy feedback that provides information about treatment progression and bubble cloud location, another form of feedback that is required for optimal histotripsy efficacy involves correction for aberrations induced by tissue heterogeneities. The speed of sound in biological soft-tissue can vary by over 10% between tissue types [37, 38, 39]. These sound speed variations are caused by natural heterogeneities in tissue, and they result in phase aberrations of ultrasound pulses in two ways. First, the impedance mismatch between tissues as well as the overlying water standoff can result in refractory effects that alter the direction of acoustic propagation [40]. Attempts have been made to match the impedance of the acoustic coupling bath between the histotripsy transducer and the tissue sample or patient [12] thereby matching the sound speed of the couplant and the tissue. While this method decreases aberration due to the initial interface between the acoustic standoff and the tissue surface, this does not correct for aberrations that occur within the patient. Second, the sound speed variations can cause pulses of ultrasound from various portions of an ultrasound array to arrive at the focus at varying times thus resulting in decreased constructive interference [41]. For therapeutic ultrasound, phase aberrations are the primary source of overall acoustic aberration rather than absorption and scattering, and these phase aberrations can cause severe decorrelation of transmit waveforms [42]. This effect can reduce the treatment efficacy and, in some cases, prevent treatment altogether [43, 44]. Several aberration correction techniques have been devised, e.g., [45], and these are discussed in greater detail later in this dissertation. Notably, for transcranial histotripsy, significant efforts have been made to reduce the aberrations caused by the skull and other bony structures [46] [47] [48]. However, this research is not directly applicable to soft-tissue histotripsy because the soft-

tissue areas of treatment such as the abdomen are devoid of large scattering bodies such as the skull. Additionally, during *in vivo* soft-tissue histotripsy experiments, reductions in sound propagation through tissue due to acoustic aberrations are known to significantly reduce treatment efficacy [12], yet no aberration correction methods specifically designed for soft-tissue histotripsy are used in practice. Therefore, there is a significant need for research into aberration correction techniques for soft-tissue histotripsy.

1.3. The Acoustic Cavitation Emission

During the initiation of inertially cavitating bubbles such as those found in the histotripsy bubble cloud, a series of shockwaves is emitted during the period of maximum bubble wall expansion [49]. As these bubbles expand, they reach a maximum bubble radius and begin to collapse inwardly, and as they collapse to a single point, another shockwave is released [50, 51]. Collectively, these shockwaves have been referred to as the acoustic cavitation emission (ACE) [52, 53]. These shockwaves have been studied heavily from both a physics perspective [54]-[60], and from a practical perspective to monitor therapeutic ultrasound in the field of passive cavitation detection (PCD) [61]-[68]. PCD has been used for monitoring both stable cavitation [69] and inertial cavitation [70] during high-intensity focused ultrasound (HIFU) therapies, which generally use the thermal effects of ultrasound to destroy unwanted tissues [71]. PCD, however, generally uses a separate transducer from the therapy transducer. For histotripsy, emissions from the cavitation bubble cloud have been received by a separate PCD receiver, and it has been shown that the spatial variability of the backscatter signal correlated with the level of histotripsy-induced tissue homogenization [72]. Additionally, it is hypothesized that the shockwaves emitted by the bubble cloud could be used as a point source guidestar for aberration correction similar to in [38]

[44] [73] - [77]. We therefore hypothesize that by receiving ACE signals on an entire histotripsy array, we will be able to (1) track changes in cavitation dynamics over the course of treatment due to tissue fractionation and (2) use these received signals to correct for acoustic aberrations thereby improving histotripsy treatment efficacy. Based on the above scientific premise, we hypothesize that developing the technology to allow for the therapy array to easily and quickly acquire and process the received waveforms will address a number of current unmet needs that will drastically improve histotripsy therapy.

1.4. Challenges of Receive-Enabled Histotripsy

The ultrasonic transmitters used in histotripsy transducers are standard piezoelectric elements generally made from one of several variations of lead zirconate titanite (PZT). As is the case with all piezoelectric materials, these PZT histotripsy elements are capable of both transmitting ultrasound and receiving ultrasound. However, the hardware does not yet exist to obtain these received signals from the histotripsy transmitters. There are several useful applications for the acoustics received by the transmit elements of a histotripsy array. These applications include cavitation localization [78], mapping of physiological structures such as the skull, aberration correction [46], and monitoring of tissue integrity [79]. Therefore, compared to a histotripsy array that essentially treats "blindly" without receive capability, a receive-capable histotripsy array could drastically improve current therapy efficacy in a variety of treatments. However, there are several technical challenges involved in creating receive-capable histotripsy arrays. First, a typical histotripsy array has hundreds of individual ultrasound transmitters. Therefore, a histotripsy receiver system must be a highly-parallelized receiver that is able to acquire data from hundreds of channels simultaneously. This results in a very large amount of

generated data, so the computing infrastructure for managing and transferring large amounts of data must also be developed. Second, histotripsy drivers transmit electrical pulses on the order of 3 kV to each individual channel at hundreds to thousands of Hertz pulse repetition frequency (PRF), yet many of the useful signals received by the histotripsy array elements are on the order of less than ten Volts to hundreds of Volts. Therefore, a histotripsy receiver system must be able to isolate sensitive electronics from high-voltage signals and also have a high dynamic range. Third, all of these technical challenges must be solved without drastically increasing the cost of histotripsy systems. Several other researchers have worked towards the development of receive-capable therapeutic ultrasound primarily for thermal therapies, and these will be discussed in greater detail in Chapter 3. However, each of these have their own drawbacks and none of them are adaptable for histotripsy. Therefore, there is a clear need for the technological development of receive-capable histotripsy systems.

1.5. Outline of This Dissertation

This dissertation is organized into six chapters to present acoustic techniques for histotripsy feedback and, in particular, feedback methods that are enabled by receive-capable histotripsy systems.

Chapter 1 describes the scope of this dissertation, introduces traditional histotripsy, the need for better feedback methods for histotripsy, and some of the challenges associated with developing receive-capable histotripsy arrays.

Chapter 2 further investigates bubble-induced color Doppler feedback for histotripsy and, specifically, the relationship of the data from this feedback method to the destruction of various physiological structures in tissue from a histological perspective. The remainder of this dissertation

is concerned with using receive-capable histotripsy arrays for both histotripsy monitoring and aberration correction feedback.

Chapter 3 discusses the challenges with receive-capable histotripsy, various prototypes that were designed and tested to approach these problems, and the technical details of two varieties of receive-capable histotripsy systems.

Chapter 4 investigates the relationship between the acoustical physics of histotripsy bubbles clouds, which can be detected by receive-capable arrays, and tissue destruction. In this chapter, a new method for histotripsy feedback using the cavitation collapse time is evaluated and the prospect of using it on receive-capable histotripsy arrays is discussed.

Chapter 5 investigates methods for using receive-capable histotripsy arrays and the ACE signal for aberration correction through soft tissue.

Finally, Chapter 6 summarizes the findings and engineering and scientific contributions of this dissertation, and provides insight into future directions for receive-capable histotripsy research.

1.6. References

[1] "Key Statistics About Liver Cancer," American Cancer Society, 6 Jan 2017. [Online]. Available: https://www.cancer.org/cancer/liver-cancer/about/what-is-key-statistics.html. [Accessed 5 Jun 2017].

[2] "Liver Cancer," Centers for Disease Control and Prevention, 12 Jul 2016. [Online]. Available: https://www.cdc.gov/cancer/liver/index.htm. [Accessed 5 Jun 2017].

[3] "What is Pancreatic Cancer?," American Cancer Society, 2016 May 2016. [Online]. Available: https://www.cancer.org/cancer/pancreatic-cancer/about/what-is-pancreatic-cancer.html. [Accessed 5 Jun 2017].

[4] "What is Kidney Cancer?," American Cancer Society, 16 May 2016. [Online]. Available: https://www.cancer.org/cancer/kidney-cancer/about/what-is-kidney-cancer.html. [Accessed 5 Jun 2017].

[5] "What is Colorectal Cancer?," American Cancer Society, 6 April 2017. [Online]. Available: https://www.cancer.org/cancer/colon-rectal-cancer/about/what-is-colorectal-cancer.html. [Accessed 5 Jun 2017].

[6] "What is Breast Cancer?," American Cancer Society, 18 Aug 2016. [Online]. Available: https://www.cancer.org/cancer/breast-cancer/about/what-is-breast-cancer.html. [Accessed 5 Jun 2017].

[7] "Liver Cancer," Mayo Clinic, 24 Mar 2016. [Online]. Available: http://www.mayoclinic.org/diseases-conditions/liver-cancer/home/ovc-20198165. [Accessed 5 Jun 2017].

[8] C. Mougenot, M. Kohler, J. Enholm, B. Quesson and C. Moonen, "Quantification of near-field heating during volumetric MR-HIFU ablation," *Medical Physics,* vol. 38, no. 1, pp. 272-82, 2010.

[9] R. Illing, J. Kennedy, F. Wu, G. ter Haar, A. Protheroe, P. Friend, F. Gleeson, D. Cranston, R. Phillips and M. Middleton, "The safety and feasibility of extracorporeal high-intensity focused ultrasound (HIFU) for the treatment of liver and kidney tumors in a Western population," *British Journal of Cancer,* vol. 93, no. 8, pp. 890-5, 2005.

[10] Z. Xu, A. Ludomirsky, L. Y. Eun, T. L. Hall, B. C. Tran, B. J. Fowlkes and C. A. Cain, "Controlled Ultrasound Tissue Erosion," *IEEE Trans. on Ultrasonics, Ferroelectrics, and Frequency Control,* vol. 51, no. 6, pp. 726-736, June 2004.

[11] X. Zhang, G. E. Owens, C. A. Cain, H. S. Gurm, J. Macoskey and Z. Xu, "Histotripsy Thrombolysis on Retracted Clots," *Ultrasound in Medicine & Biology,* vol. 42, no. 8, pp. 1903-1918, August 2016.

[12] X. Zhang, J. Macoskey, K. Ives, G. Owens, H. Gurm, J. Shi, M. Pizzuto, C. CA and Z. Xu, "Non-Invasive Thrombolysis Using Microtripsy in a Porcine Deep Vein Thrombosis Model," *Ultrasound Med. Biol.,* vol. 43, no. 7, pp. 1378-90, 2017.

[13] E. Vlaisavljevich, Y. Kim, S. Allen, S. Pelletier, C. Cain, K. Ives and Z. Xu, "Image-Guided Non-Invasive Ultrasound Liver Ablation Using Histotripsy: Feasibility Study in an In Vivo Porcine Model," *Ultrasound in Medicine & Biology,* vol. 39, no. 8, pp. 1398-1409, August 2013.

[14] G. R. Schade, J. Keller, I. Kimberly, X. Cheng, T. J. Rosol and W. W. Roberts, "Histotripsy focal ablation of implanted prostate tumor in an ACE-1 canine cancer model," *The Journal of Urology,* vol. 188, no. 5, pp. 1957-1964, November 2012.

[15] A. Lake, T. Hall, K. Kieran, J. Fowlkes, C. Cain and W. Roberts, "Histotripsy: Minimally invasive technology for prostatic tissue ablation in an in vivo canine model," *Urology,* vol. 72, no. 3, pp. 682-6, 2008.

[16] Z. Xu, A. Ludomirsky, L. Eun, T. Hall, B. Tran, J. Fowlkes and C. Cain, "Noninvasive creation of an atrial septal defect by histotripsy in a canine model," *Circulation,* vol. 121, pp. 742-49, 2010.

[17] Y. Kim, T. Hall, Z. Xu and C. Cain, "Transcranial histotripsy therapy: A feasibility study," *IEEE Trans. Ultrason. Ferroelect. Freq. Control,* vol. 61, no. 4, pp. 582-93, 2014.

[18] Z. Xu, T. Hall, J. B. Fowlkes and C. A. Cain, "Effects of acoustic parameters on bubble cloud dynamics in ultrasound tissue erosion (histotripsy)," *The Journal of the Acoustical Society of America,* vol. 122, no. 1, pp. 229-236, July 2007.

[19] G. Owens, R. Miller, G. Ensing, K. Ives, D. Gordon, A. Ludomirsky and Z. Xu, "Therapeutic ultrasound to noninvasively create intracardiac communications in an intact animal model," *Catheter. Cardiovasc. Interv.,* vol. 77, no. 4, pp. 580-8, 2011.

[20] K.-W. Lin, Y. Kim, A. D. Maxwell, T.-Y. Wang, T. L. Hall, Z. Xu, B. J. Fowlkes and C. A. Cain, "Histotripsy beyond the intrinsic cavitation threshold using very short ultrasound pulses: Microtripsy," *IEEE Trans. on Ultrasonics, Ferroelectrics, and Frequency Control,* vol. 61, no. 2, pp. 251-265, February 2014.

[21] V. Khokhlova, J. Fowlkes, W. Roberts, G. Schade, Z. Xu, T. Khoklova, T. Hall, A. Maxwell, Y.-N. Wang and C. Cain, "Histotripsy methods in mecahnical disintegration of tissue: Towards clinical applications," *International Journal of Hyperthermia,* vol. 31, no. 2, pp. 145-62, 2015.

[22] N. Styn, J. Wheat, T. Hall and W. Roberts, "Histotripsy of VX-2 Tumor Implanted in a Renal Rabbit Model," *Journal of Endourology,* vol. 24, no. 7, pp. 1145-1150, 2010.

[23] G. Owens, R. Miller, S. Owens, S. Swanson, K. Ives, G. Ensing and D. X. Z. Gordon, "Intermediate-term effects of intracardiac communications created noninvasively by therapeutic ultrasound (histotripsy) in a porcine model," *Pediatric cardiology,* vol. 33, no. 1, pp. 83-9, 2012.

[24] T. Hall, J. Fowlkes and C. Cain, "A real-time measure of cavitation induced tissue disruption by ultrasound imaging backscatter reduction," *IEEE Trans Ultrason Ferroelectr Freq Control,* vol. 54, no. 3, pp. 569-75, 2007.

[25] R. Miller, A. Maxwell, T.-Z. Wang, J. Fowlkes, C. Cain and Z. Xu, "Real-time elastography-based monitoring of histotripsy tissue fractionation using color Doppler," in *IEEE International Ultrasonics Symposium*, Dresden, Germany, 2012.

[26] T.-Z. Wang, T. Hall, Z. Xu, J. Fowlkes and C. Cain, "Imaging feedback of histotripsy treatments using ultrasound shear wave elastography," *IEEE Trans. Ultrason. Ferroelec. Freq. Control,* vol. 59, no. 6, pp. 1167-81, 2012.

[27] C. Cain and T.-Z. Wang, "Imaging feedback of histotripsy treatments with ultrasound transient elastography". United States Patent US 20130102932 A1, 10 Oct 2012.

[28] T.-Z. Wang, T. Hall, Z. Xu, J. Fowlkes and C. Cain, "Imaging feedback for histotripsy by characterizing dynamics of acoustic radiation force impulse (ARFI)-induced shear waves excited in a treated volume," *IEEE Trans. Ultrason. Ferroelec. Freq. Control,* vol. 61, no. 7, pp. 1137-51, 2014.

[29] K. Hynynen, A. Darkazanli, E. Unger and J. Schenck, "MRI-guided noninvasive ultrasound surgery," *Medical Physics,* vol. 20, no. 1, pp. 107-115, 1993.

[30] N. McDannold, K. Hynynen, D. Wolf, G. Wolf and F. Jolesz, "MRI Evaluation of Thermal Ablation of Tumors with Focused Ultrasound," *J. Magn. Reson. Imaging,* vol. 8, no. 1, pp. 91-100, February 1998.

[31] S. P. Allen, W. W. Roberts, T. L. Hall, C. A. Cain and L. Hernandez-Garcia, "Characterization of the in vivo Histotripsy Lesion Using High Field MRI," in *Proceedings,*

International Society for Magnetic Resonance in Medicine 20th Annual Meeting and Exhibition, Melbourne, Austrialia, 2012.

[32] N. Lipsman, S. ML, Y. Huang, L. Lee, T. Sankar, M. Chapman, K. Hynynen and L. AM, "MR-guided focused ultrasound thalamotomy for essential tremor: A proof-of-concept study," *Lancet Neurol.,* vol. 12, no. 5, pp. 462-468, 2013.

[33] W. Roberts, "Focused ultrasound ablation of renal and prostate cancer: Current technology and future directions," *Urol. Oncol.,* vol. 23, no. 5, pp. 367-371, 2005.

[34] M. Gyöngy and C.-C. Coussios, "Passive Spatial Mapping of Inertial Cavitation During HIFU Exposure," *IEEE Trans. Biomed. Eng.,* vol. 57, no. 1, pp. 48-56, January 2010.

[35] R. Miller, Z. X, M. AD, C. CA and X. Z, "Bubble-Induced Color Doppler Feedback for Histotripsy Fractionation," *IEEE Trans Ultrason Ferroelectr Freq Control,* vol. 63, no. 3, pp. 408-19, 2016a.

[36] X. Zhang, R. M. Miller, K.-W. Lin, A. M. Levin, G. E. Owens, H. S. Gurm, C. A. Cain and Z. Xu, "Real-Time Feedback of Histotripsy Thrombolysis Using Bubble-Induced Color Doppler," *Ultrasound in Medicine & Biology,* vol. 41, no. 5, pp. 1389-1401, May 2015.

[37] F. Fry and J. Barger, "Acoustic properties of the human skull," *J. Acoust. Soc. Am.,* vol. 63, no. 5, pp. 1576-90, 1978.

[38] S. Flax and M. O'Donnell, "Phase-aberration correction using signals from point reflectors and diffuse scatterers: basic principles," *IEEE Trans. Ultrason., Ferroelect., Freq. Control,* vol. 35, no. 6, pp. 758-67, 1988.

[39] F. A. Duck, "Acoustic Properties of Tissue at Ultrasonic Frequencies," in *Physical Properties of Tissue: A Comprehensive Reference Book*, San Diego, CA, Academic Press Inc., 1990, pp. 73-135.

[40] D. Blackstock, "Transmission Phenomena: Oblique Incidence," in *Fundamentals of Physical Acoustics*, USA, John Wiley & Sons, Inc., 2000, pp. 186-217.

[41] J. Macoskey, T. Hall, J. Sukovich, S. Choi, K. Ives, E. Johnsen, C. Cain and Z. Xu, "Soft-Tissue Aberration Correction for Histotripsy," *IEEE Transactions on Ultrasonics, Ferroelectrics, and Frequency Control,* vol. 65, no. 11, pp. 2073-85, 2018.

[42] K. Vortman and S. Vitek, "Tissue aberration corrections in ultrasound therapy". United States Patent 8,088,067, 2012.

[43] M. Pernot, J.-F. Aubry, M. Tanter, J.-L. Thomas and M. Fink, "High power transcranial beam steering for ultrasonic brain therapy," *Phys. Med. Biol.,* vol. 48, pp. 2577-89, 2003.

[44] M. Pernot, G. Montaldo, M. Tanter and M. Fink, ""Ultrasonic stars" for time-reversal focusing using induced cavitation bubbles," *Applied Physics Letters,* vol. 88, p. 034102, 2006.

[45] K. Vortman and S. Vitek, "Tissue aberration corrections in ultrasound therapy". United States Patent 8,088,067, 3 Jan. 2012.

[46] J. Sukovich, Z. Xu, T. Hall, J. Macoskey and C. Cain, "Transcranial histotripsy acoustic-backscatter localization and aberration correction for volume treatments," in *173rd Meeting of the Acoustical Society of America*, Boston, MA, 2017.

[47] G. Clement and K. Hynynen, "A non-invasive method for focusing ultrasound through the human skull," *Phys. Med. Biol.,* vol. 47, pp. 1219-36, 2002.

[48] Y. Kim, T.-Y. Wang, Z. Xu and C. Cain, "Lesion generation through ribs using histotripsy therapy without aberration correction," *IEEE Trans. Ultrason. Ferroelec. Freq. Control,* vol. 58, no. 11, pp. 2334-43, 2011.

[49] J. Sukovich, T. Hall, J. Macoskey, C. Cain and Z. Xu, "Investigation of the source of histotripsy acoustic backscatter signals," *Journ. Acoust. Soc. Am.,* vol. 141, p. 3551, 2017.

[50] T. Leighton, "The Forced Bubble," in *The Acoustic Bubble*, San Diego, Academic Press, Inc., 1994, pp. 287-438.

[51] T. Whittingham, F. Duck, Baker and S. H. AC, "The Purpose and Techniques of Acoustic Output Measurement," in *Ultrasound in Medicine*, Philadelphia, Institute of Physics Publishing, 1998, pp. 129-148.

[52] J. Macoskey, S. Choi, T. Hall, E. Vlaisavljevich, J. Lundt, E. Johnsen, C. Cain and Z. Xu, "Using the cavitation collapse time to indicate the extent of histotripsy-induced tissue fractionation," *Phys. Med. Biol.,* vol. 63, p. 155013, 2018.

[53] M. Burgess and T. Porter, "Control of acoustic cavitation for efficient sonoporation with phase-shift nanoemulsions," *Ultrasound Med. Biol.,* vol. 45, no. 3, pp. 846-58, 2019.

[54] M. Plesset, "Shockwaves from cavity collapse," *Phil. Trans. Royal Soc. A,* vol. 260, no. 1110, pp. 241-244, 1966.

[55] M. Plesset and R. Chapman, "Collapse of an inertially spherical vapour cavity in the neighborhood of a solid boundary," *J. Fluid Mech.,* vol. 47, no. 2, pp. 283-90, 1971.

[56] M. Plesset and A. Prosperetti, "Bubbly Dynamics and Cavitation," *Ann. Rev. Fluid Mech.,* vol. 9, pp. 145-185, 1977.

[57] R. Ivany and F. Hammitt, "Cavitation bubble collapse in viscous, compressible liquids - Numerical analysis," *J. Basic Eng.,* vol. 87, no. 4, pp. 977-985, 1965.

[58] T. Mitchell and F. Hammitt, "Asymmetric cavitation bubble collapse," *J. Fluids Eng.,* vol. 95, no. 1, pp. 29-37, 1973.

[59] C.-D. Ohl, A. Philipp and W. Lauterborn, "Cavitation bubble collapse studied at 20 million frames per second," *Ann. Physik,* vol. 507, no. 1, pp. 26-34, 1995.

[60] C. Ohl and R. Ikink, "Shock-wave-induced jetting of micron-sized bubbles," *Phys. Rev. Lett.,* vol. 90, p. 214502, 2003.

[61] J. Gateau, J. Aubry, M. Pernot, M. Fink and M. Tanter, "Combined Passive Detection and Ultrafast Active Imaging of Cavitation Events Induced by Short Pulses of High-Intensity Ultrasound," *IEEE Trans. Ultrason., Ferroelect., Freq. Control ,* vol. 58, no. 3, pp. 517-32, 2011.

[62] K. Haworth, T. Mast, K. Radhakrishnan, M. Burgess, J. Kopechek, S. Huang, D. McPherson and C. Holland, "Passive imaging with pulsed ultrasound insonations," *J. Acoust. Soc. Am.,* vol. 132, no. 1, pp. 544-53, 2012.

[63] M. Gyöngy and C.-C. Coussios, "Passive Spatial Mapping of Inertial Cavitation During HIFU Exposure," *IEEE Transactions on Biomedical Engineering,* vol. 57, no. 1, pp. 48-56, January 2010b.

[64] Y. Tung, F. Vlachos, J. Choi, T. Deffieux, K. Selert and E. Konofagou, "In vivo transcranial cavitation threshold detection during ultrasound-induced blood-brain barrier opening in mice," *Phys. Med. Biol.,* vol. 55, no. 20, pp. 6141-55, 2010.

[65] N. McDannold, N. Vykhodtseva and K. Hynynen, "Targeted disruption of the blood–brain barrier with focused ultrasound: association with cavitation activity," *Phys. Med. Biol.,* vol. 51, no. 4, pp. 793-807, 2006.

[66] J. Choi, M. Pernot, S. Small and E. Konofagou, "Noninvasive, transcranial and localized opening of the blood-brain barrier using focused ultrasound in mice," *Ultras. Med. Biol.,* vol. 33, no. 1, pp. 95-104, 2007.

[67] M. Gyöngy and C.-C. Coussios, "Passive cavitation mapping for localization and tracking of bubble dynamics," *J. Acoustc. Soc. Am.,* vol. 128, no. 4, pp. 175-180, October 2010a.

[68] V. Salgaonkar, S. Datta, C. Holland and T. Mast, "Passive cavitation imaging with ultrasound arrays," *J. Acoust. Soc. Am.,* vol. 126, no. 6, pp. 3071-83, 2009.

[69] C. Coussios, C. Farny, G. Ter Haar and R. Roy, "Role of acoustic cavitation in the delivery and monitoring of cancer treatment by high-intensity focused ultrasound (HIFU)," *International Journal of Hyperthermia,* vol. 23, no. 2, pp. 105-120, 2007.

[70] M. Gyöngy, M. Arora, J. A. Noble and C. C. Coussios, "Use of Passive Arrays for Characterization and Mapping of Cavitation Activity during HIFU Exposure," Beijing, 2008.

[71] N. McDannold, K. Hynynen, D. Wolf, G. Wolf and F. Jolesz, "MRI Evaluation of Thermal Ablation of Tumors with Focused Ultrasound," *Journal of Magnetic Resonance Imaging,* vol. 8, no. 1, pp. 91-100, February 1998.

[72] J. E. Parsons, C. A. Cain and B. J. Fowlkes, "Spatial Variability in Acoustic Backscatter as an Indicator of Tissue Homogenate Production in Pulsed Cavitational Ultrasound Therapy," *IEEE Trans. on Ultrasonics, Ferroelectrics, and Frequency Control,* vol. 54, no. 3, pp. 576-590, March 2007.

[73] D. Zhao and G. Trahey, "Comparisons of image quality factors for phase aberration correction with diffuse and point targets: theory and experiments," *IEEE Trans. Ultrason., Ferroelectr., Freq. Control,* vol. 38, no. 2, pp. 125-32, 1991.

[74] M. Fink, "Time reversal of ultrasonic fields - Part I: Basic principles"," *IEEE Trans. Ultrason., Ferroelectr., Freq. Control,* vol. 39, no. 5, pp. 555-66, 1994.

[75] D. Lui and R. Waag, "Correction of ultrasonic wavefront distortion using backpropagation and a reference waveform method for time-shift compensation," *J. Acoust. Soc. Am.,* vol. 96, no. 2, pp. 649-60, 1994.

[76] S. Krishnan, P.-C. Li and M. O'Donnell, "Adaptive compensation of phase and magnitude aberrations," *IEEE Trans. Ultrason., Ferroelectr., Freq. Control,* vol. 43, no. 1, pp. 44-55, 1996.

[77] M. Tabei, T. Mast and R. Waag, "Simulation of ultrasonic focus aberration and correction through human tissue," *J. Acoust. Soc. Am.,* vol. 113, no. 2, pp. 1166-76, 2003.

[78] J. Sukovich, Z. Xu, T. Hall, J. Macoskey and C. Cain, "Histotripsy pulse-reflection for 3D image forming and bubble cloud localization in transcranial applications," *J. Acoust. Soc. Am.,* vol. 140, p. 3083, 2016.

[79] J. Macoskey, J. Sukovich, T. Hall, C. Cain and Z. Xu, "Real-time acoustic-based feedback for histotripsy therapy," in *173rd Meeting of the Acoustical Society of America*, Boston, MA, 2017.

[80] E. Vlaisavljevich, Y. Kim, G. Owens, W. Roberts, C. Cain and Z. Xu, "Effects of tissue mechanical properties on susceptibility to histotripsy-induced tissue damage," *Phys. Med. Biol.,* vol. 59, pp. 253-270, 2014a.

CHAPTER 2

Histological Investigation into the Effects of Tissue Microstructure on Bubble-Induced Color Doppler Feedback for Histotripsy

This chapter has been published in *Ultrasound in Medicine & Biology*. 2018; 44(2):602-612.

2.1. Introduction

Histotripsy is a therapeutic ultrasound technique that employs inertial cavitation to mechanically destroy and fractionate unwanted target-tissue within the body noninvasively without damaging surrounding tissue [2, 3]. Histotripsy has been investigated for the treatment of deep vein thrombosis [4, 5], liver tumors [6], benign prostatic hyperplasia [7, 8], congenital heart diseases [9], and transcranial brain applications [10].

Quantitative imaging feedback for indicating tissue fractionation is important for monitoring and guiding non-invasive ablation techniques such as histotripsy to ensure treatment accuracy and efficacy. Magnetic resonance guided focused ultrasound (MRgFUS) is used to provide a 3D temperature map as real-time feedback during high-intensity focused ultrasound (HIFU) thermal treatments [11, 12, 13] and has been approved by the FDA to treat several conditions including essential tremor [14], uterine fibroids [7], and prostate cancer [15]. However, MRI-guidance for histotripsy would require MRI-compatible histotripsy arrays as well as procedural MRI scanners.

Ultrasound imaging has previously been used to guide HIFU therapy and for monitoring treatment and the development of HIFU-induced cavitation [16, 17]. For histotripsy, B-mode ultrasound imaging has also been used in real-time during treatment to monitor changes in the bubble cloud, which appears as a dynamically changing hyperechoic zone [16, 18]. When

substantial tissue liquefaction has occurred, the tissue appears to be hypoechoic on B-mode imaging [19, 20]. However, B-mode ultrasound is sub-optimal for monitoring the treatment effect due to its low sensitivity, as the hypoechoic zone only occurs when substantial tissue fractionation is achieved [21]. Additionally, as the intensity of the tissue speckle varies across different tissues both temporally and from patient-to-patient, it is unlikely that a universal intensity threshold could be set to indicate complete tissue fractionation for different tissues and patients.

Ultrasound elastography, such as acoustic radiation force impulse (ARFI) imaging, has also been investigated to detect histotripsy lesion formation. As the histotripsy treatment progresses, the target-tissue is fractionated until it turns into a liquid-appearing homogenate, indicating that the elasticity of the tissue decreases throughout treatment [22, 23, 24, 25]. A reliable elasticity method would be especially useful for histotripsy in viscoelastic tissues such as the liver where the collagenous elements of the extracellular matrix are the primary structural component. These elastography methods have been experimentally successful in the detection of tissue fractionation with higher sensitivity than B-mode speckle intensity. However, as the tissue becomes more liquefied, the shear wave propagation used for elastography imaging techniques become increasingly restricted resulting in decreased accuracy of elastography measurements later in histotripsy treatment [26]. Additionally, reflections from the histotripsy-induced cavitation nuclei are known to contribute to and interfere with the radiation force used for ARFI imaging, which may introduce artifacts in the elastography methods [24].

Recently, a new modality called bubble-induced color Doppler (BCD) has been developed to monitor histotripsy-induced tissue fractionation in real-time [27, 28, 29]. This method uses Doppler ultrasound on a conventional clinical ultrasound machine to obtain velocity estimations of the residual cavitation nuclei that persist after cavitation during histotripsy therapy. Our

previous work has shown that this motion is due to the disturbance caused by the rapid expansion and collapse of the bubble cloud, which has also been observed previously elsewhere [30]. This motion is only observed when the histotripsy bubble cloud is formed, and we have found that this residual motion can last for at least 20 ms after each histotripsy pulse, thus indicating that it is likely not due to acoustic radiation force. Furthermore, we have found that as the tissue becomes increasingly fractionated, the motion of residual nuclei lasts longer, and that the change of the BCD signal correlates somewhat with increased tissue destruction [28]. However, in this previous study, only cellular destruction was quantified over a small sample of pulse numbers. Thus, a more detailed physiological investigation of the correlation of the BCD signal with tissue destruction is required. Interestingly, in Vlaisavljevich, et al. (2014), it was shown that tissues with higher Young's moduli result in cavitation bubbles with shorter lifespans and smaller maximum radii [31]. This suggests that as the tissue becomes more fractionated and the elasticity of the tissue decreases, the cavitation bubble cloud should last longer with a higher maximum radius. Therefore, due to the fact that the BCD signal is highly dependent on cavitation dynamics which are dependent on tissue mechanics and we know that the residual nuclei motion responsible for the BCD signal lasts increasingly longer throughout treatment, we hypothesize that the BCD signal is more closely correlated with the destruction of structural components of tissue that contribute to the overall mechanical properties of tissue rather than the cellular components.

In this study, we investigated how changes in the BCD signal throughout histotripsy treatment are quantitatively correlated to the levels of fractionation of specific structures within liver tissue induced by histotripsy. Histotripsy therapy was applied to *ex vivo* bovine liver tissue by a 112-element histotripsy array at varying levels of tissue fractionation (i.e., number of histotripsy pulses), and BCD signals were acquired for all samples. Each tissue sample was

histologically stained to quantify cellular destruction, type III collagen destruction, and type I collagen destruction.

2.2. Methods

2.2.1 Ex Vivo Bovine Liver Preparation

Freshly excised bovine liver acquired from a local abattoir was preserved in room-temperature PBS-buffered saline and was used within 24 hours of harvest. Prior to treatment, liver was sectioned into approximately 4 cm cube sections and was then placed in degassed PBS-buffered saline under vacuum in a desiccator for five hours. Liver samples were then removed from the desiccator and were embedded in blocks of 1.5% agarose to maintain structural stability. The blocks were suspended in place via two carbon skewers. This was done so that no structural support material other than agar was present between the histotripsy array and the tissue, thus minimizing aberration and the chance for cavitation on the surface of the sample. Once the agarose was solidified after roughly one hour, the tissue phantoms were positioned in the water above the histotripsy array using a three-axis positioner.

2.2.2 Histotripsy Treatment Parameters

The treatments were applied in a 6x6x7 mm volume consisting of 219 treatment locations excited by electronically steering the phased array. The treatment locations were organized in five alternating 7x7 and 6x6 location layers with 1 mm spacing between locations within each plane (x- and y-dimensions) and 1.5 mm spacing between planes (z-dimension) to ensure uniform fractionation throughout the volume. The layers were placed parallel to the histotripsy wave front,

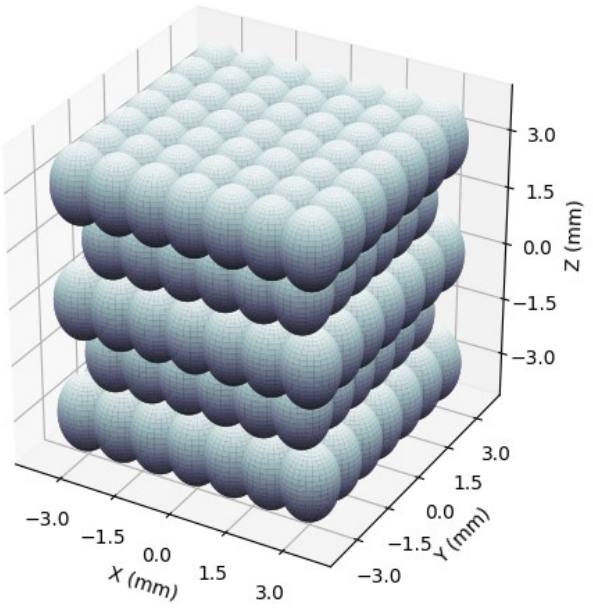

Figure 2.1 Treatment location packing grid. Spacing between points in the x- and y- directions is 1 mm, and spacing between layers in the z-direction is 1.5 mm. In this orientation, ultrasound is being delivered from the bottom of the grid, i.e., from negative z towards positive z.

and the layer farthest from the array was treated first. Locations within each layer were treated randomly. A rendering of the packing grid is shown in Figure 2.1. The array focus was steered to locations at 100 Hz PRF except for the central location where the BCD signal was acquired. The BCD signal was only acquired at the central location of the lesion. Prior to the pulse at the central location, the array paused for 0.5 seconds. This was done to allow residual cavitation nuclei from the previous pulse to dissolve [32, 26]. Liver samples were treated with 0, 30, 60, 100, 200, 300, 500, or 1000 pulses-per-location to produce a wide range of tissue fractionation. These pulse numbers were chosen to cover the full range of tissue fractionation to complete cell disruption in the treatment volume and to align with regions of change in BCD profiles collected during preliminary experiments. For each dose level, 6 replicate samples were treated. A schematic overview of the experimental setup is shown in Figure 2.2. The 112-element 500 kHz therapy array was placed facing upwards in a tank filled with degassed water. The primary control computer

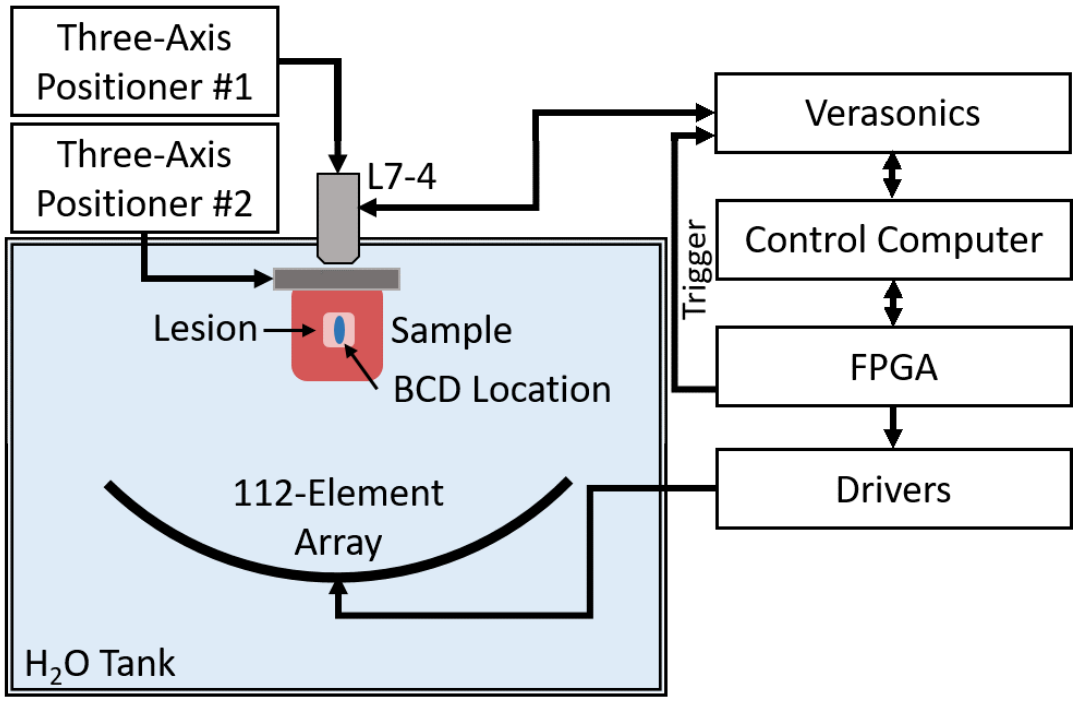

Figure 2.2: Experimental setup. A 500 kHz 112-element array is used to generate histotripsy lesions at 219 locations throughout a treatment volume in bovine liver tissue. A Verasonics system using standard Doppler ultrasound imaging with an L7-5 linear array (driven at 5 MHz) was used to acquire BCD data and was triggered by the FPGA-controlled driving system. BCD was acquired for the pulse at the central location within the lesion. An automatic three-axis positioning system was used to position the linear array, and second manual three-axis positioner was used to position the liver samples.

sent commands to the transducer driving system, which stored treatment locations and controlled the timing of treatment. The three-axis positioner holding the tissue sample was a manual positioner that allowed for gross positioning of the liver samples in the focus of the therapy array. Prior to treatment, the liver samples were imaged with B-mode ultrasound using a 5 MHz, 128-element linear imaging probe (ATL HDI L7-4, Philips, Andover, MA) with a Verasonics Imaging System (SS#: 1634, Verasonics, Inc., Redmond, WA) to ensure that therapy was occurring in relatively homogenous portions of liver that were void of large vessels or large portions of connective tissue. A motorized three-axis positioner was used to position the L7-4 imaging probe.

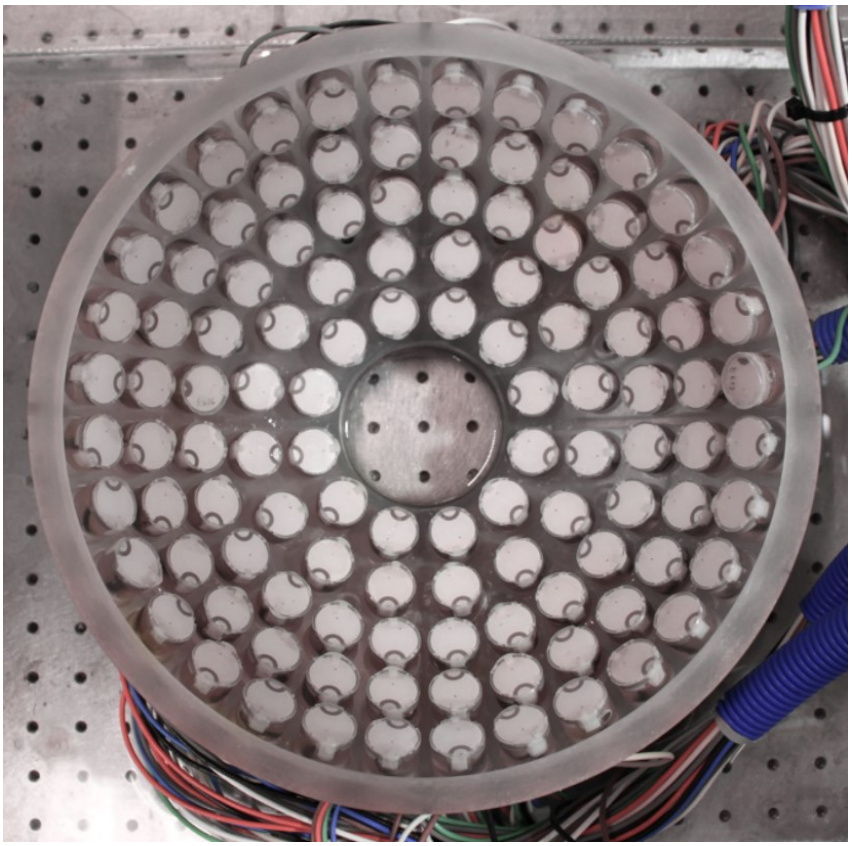

Figure 2.3: Image of the 112-element 500 kHz histotripsy phased array. From this orientation, the positive z-axis is pointed directly at the point-of-view.

The histotripsy transducer used for this study was a 112-element, 500 kHz histotripsy phased-array transducer constructed in-house [33]. An image of the array is shown Figure 2.3. The array consisted of a 15 cm radius of curvature and a 27 cm aperture. Each element was driven by one channel on a 112-channel high-voltage pulser that emitted an approximately 1.5-cycle, 3-microsecond sinusoidal acoustic pulse. The array and driving system was controlled by a set of field-programmable gate arrays (FPGAs) such that each element was individually addressable. The generated waveform at the geometric focus was evaluated using a fiber-optic probe hydrophone (FOPH) with a 100-μm diameter sensing tip [34]. The arrangement of the elements in the array produced a focal zone with a -6 dB beamwidth of 2.0 mm laterally and 6.3 mm axially when measured in the linear regime at a pressure amplitude of 8 MPa using the FOPH. During

treatment, the transducer was driven just above the intrinsic threshold for cavitation, so cavitation only occurred in the area of highest pressure rather than throughout the full -6 dB beamwidth. For peak-negative pressures above approximately 10 MPa, the waveform could not be directly measured by the FOPH due to cavitation on the fiber tip. For P- ≥10 MPa, the transducer's waveform was approximated by dividing the array into several sub-apertures, which were driven and measured separately and then summed to estimate the pressure at each calibrated driving voltage. The array was divided into four quadrant sub-apertures, which was enough to maintain a P- of <10 MPa. At the driving voltage used for this study, the extrapolated P- pressure was found to be approximately 40.8 MPa. It should be noted that nonlinear propagation was not taken into account in the extrapolation.

2.2.3 Bubble-Induced Color Doppler Acquisition and Processing

Bubble-induced color Doppler was acquired using standard Doppler ultrasound imaging on a Verasonics imaging system (Redmond, WA) using the same 5 MHz center frequency, 128-element linear imaging transducer (ATL HDI L7-4, Philips, Andover, MA) used for treatment planning. The imaging probe was placed on the opposite side of the sample from the therapy array. Prior to placing the tissue sample in the tank, the imaging probe was aligned with the geometric focus of the therapy system in the free-field by imaging the cavitation bubble cloud on B-mode. An acquisition transaxial region of interest (ROI) of 39 mm to 51 mm from the imaging probe was used to acquire the Doppler data. The Verasonics Doppler protocol was set to acquire 210 Doppler acquisitions at 10 kHz PRF to observe a temporal window of 21 ms after the central therapy pulse. This window covered the same region in which motion was recorded in a prior study using particle image velocimetry to observe the movement of residual cavitation nuclei after a histotripsy pulse

[28]. The Doppler acquisitions were processed offline using the Doppler processing algorithms included with the Verasonics ultrasound imaging system. The mean frame-by-frame Doppler velocity throughout the 21 ms after the central therapy pulse in the Doppler ROI was processed in rolling 10 acquisition segments, resulting in 200 separate 10 frame acquisitions to cover a 20 ms temporal range. A thresholding algorithm employing a multi-level Otsu's method (Matlab, The Mathworks, Natick MA, USA) was applied to the Doppler frames to observe only the areas with the greatest movement of residual nuclei. The time to peak negative rebound velocity (t_{prv}) was used to quantify the BCD data. This metric calculates the time at which the highest magnitude negative velocity after each histotripsy pulse occurs.

2.2.4 Histological Analysis of Tissue Fractionation

Upon treatment completion, samples were removed from their sample holders, and all agarose was cleaned off the tissue. Samples were then submerged in 10% buffered formalin (Fischer Scientific International, LLC, Hampton, NH) for one week for fixation. Once fixed, samples were cut into thin slices and were placed in cassettes that were then submerged in new 10% buffered formalin and sent out for histology sectioning and staining (Scientific Solutions, LLC, Fridley, MN). All formalin-fixed and paraffin-embedded liver tissue sections were stained with Masson's trichrome stain and Gordon & Sweet's reticulin stain [35]. The trichrome stain is a three-color staining protocol, which stains collagen blue, muscle fibers red, and cell nuclei dark brown to black. Trichrome staining allows for visualization of both cells and type I collagen which is the most abundant collagen in mammals. Type I collagen usually organizes into thick bundles and is found in connective tissues in the liver. Gordon & Sweet's reticulin stain was used to highlight the thin reticular fibers and basement membrane material in the liver tissue. The reticular

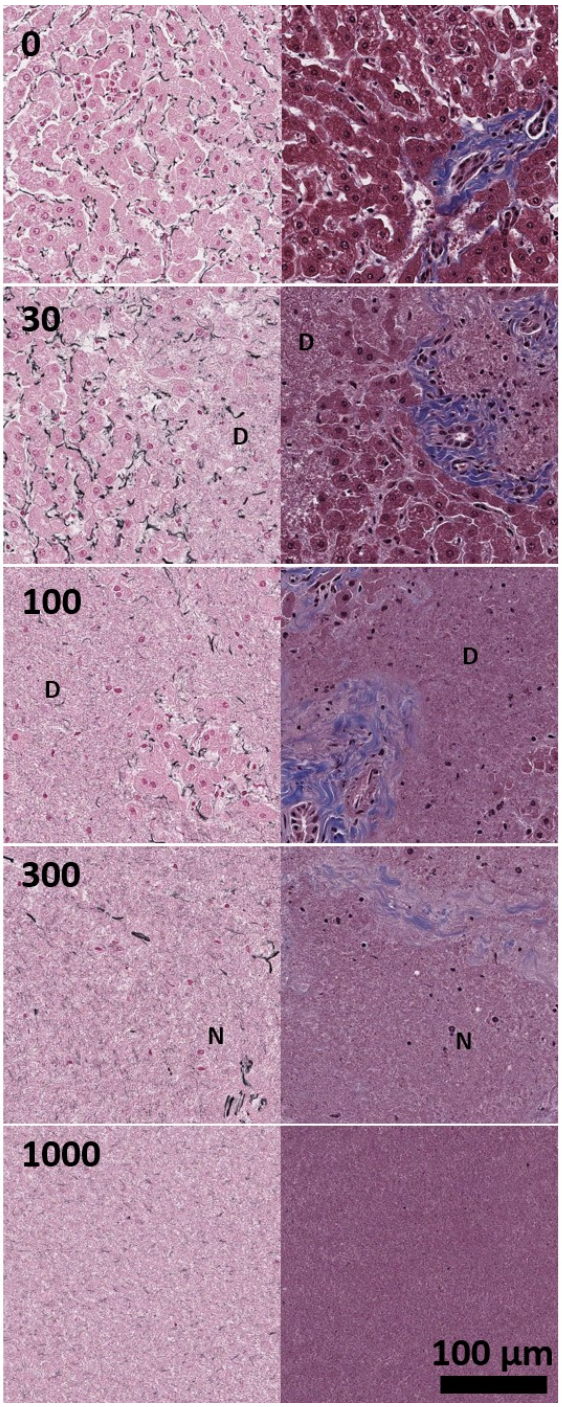

Figure 2.4: Sample histology of the liver tissue using Masson's trichrome (right column) and Gordon & Sweet's reticulin stains (left column) for histotripsy dosages of 0, (top row), 30 (second row), 100 (third row), 300 (fourth row), and 1000 (bottom row) pulses-per-location. Type I collagen is blue in trichrome stain and reticulin fiber is black in reticulin stain. For 30 and 100 pulses-per-location, areas of destruction are marked with a D. For 300 pulses-per-location, example remnant nuclei are marked with an N. Complete tissue homogenization is observed at 1000 pulses-per-location.

fibers are usually type III collagen and are found interlaced with hepatocytes in the extracellular matrix and outline the architecture of liver parenchyma. We hypothesize that cells are more susceptible to histotripsy damage while collagen is more resistant. Example images of the trichrome and reticulin stains of the liver are shown in Figure 2.4.

All slides were then scanned with a resolution of 0.253 μm/pixel – an equivalent of 400x magnification – for image processing. A square area of 15 mm^2 was selected from the center of the approximately 42 mm^2 cross-sectional lesion for image analysis. Two color-channel thresholding algorithms were used to segment the blue collagen fibers in trichrome stained slides and the dark purple/black reticular fibers in the reticulin stained slides. To determine the number of cells remaining in the lesions, ten randomly selected 1024x1024 pixel tiles within the lesion were manually counted. The number of tiles counted was based on estimated sample variance and desired detectable difference between groups using power analysis to obtain a statistical power of 0.95 with $\alpha = 0.01$ for extrapolation of cellular density to the rest of the lesion when compared to a normal distribution. A nonlinear least squares best fitting algorithm using an exponential decay model was used to calculate best fit trend lines for the histology metrics between each dosage that was analyzed, thus allowing for a continuous trend line to estimate the histology metrics at all doses between 0 and 1000 pulses-per-location. Statistical p-values for the histology data were calculated using a chi-squared goodness-of-fit test, and time constants (with time being pulse number) were calculated for each best-fit line to directly compare the histology metrics.

2.2.5 Statistical Comparison of Bubble-Induced Color Doppler and Tissue Fractionation

The BCD t_{prv} was plotted against each histology metric, and linear regression was used to fit a trend line to each relationship for a relative comparison between the metrics. Coefficients of

determination, i.e., R-squared values, were calculated for each linear regression fit to compare how well the model fit the BCD-histology comparisons. However, a high coefficient of determination does not necessarily mean that a statistical model is the right model for a given dataset. Therefore, the Pearson correlation coefficient (PCC), which measures an unbiased linear correlation between two variables and reports a p-value based on Student's t-test, was used to obtain a single quantitative metric for the extent of correlation between the BCD t_{prv} and histology metrics. The PCC was chosen because it obtains an easily comparable correlation metric between two signals regardless of the scale of the signals. The PCC returns a value ranging between -1 and 1, where 1 indicates a perfectly direct linear correlation, -1 indicates a perfectly inverse linear correlation, and 0 indicates no correlation. The PCC is mathematically defined as

$$\boldsymbol{\rho(a,b) = E(ab)/\sigma_a\sigma_b} \textbf{ (E2.1)}$$

where σ_a and σ_b are the standard deviations of signals a and b, respectively, and $E(ab)$ is the cross-correlation between a and b (Benesty et al., 2009). Because we knew a priori that there would be mono-directional change of both the BCD t_{prv} and all histology metrics, we chose a very conservative p-value of 0.001 to indicate a statistically significant correlation.

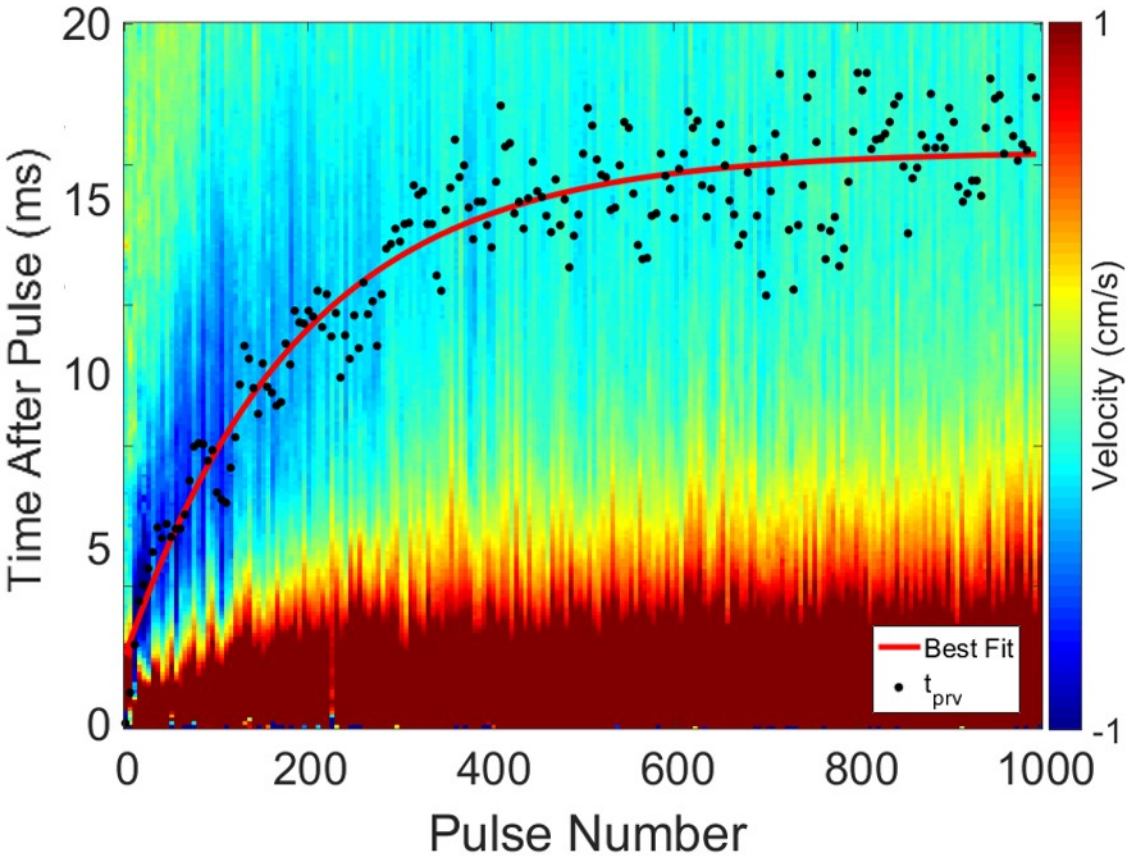

Figure 2.5: Example BCD slow-time/fast-time profile from one 1000 pulse treatment. The tprv is indicated by a black point for each pulse number, and a nonlinear least squares best-fit trend line is shown in red. The largest peak negative velocities were on the order of -1 m/s and were observed to have large negative velocities earlier in treatment.

2.3. Results

2.3.1 Bubble-Induced Color Doppler Metrics

A total of 42 lesions were treated, and their respective BCD signals for each pulse were collected and analyzed. A representative BCD slow-time/fast-time profile from one 1000 pulse-per-location treatment is shown in Figure 2.5. In all treatments, the BCD data exhibited a net large positive velocity (away from the therapy transducer) followed by a large net negative velocity (towards the therapy transducer). Early in treatment between 1 and approximately 200 pulses, a

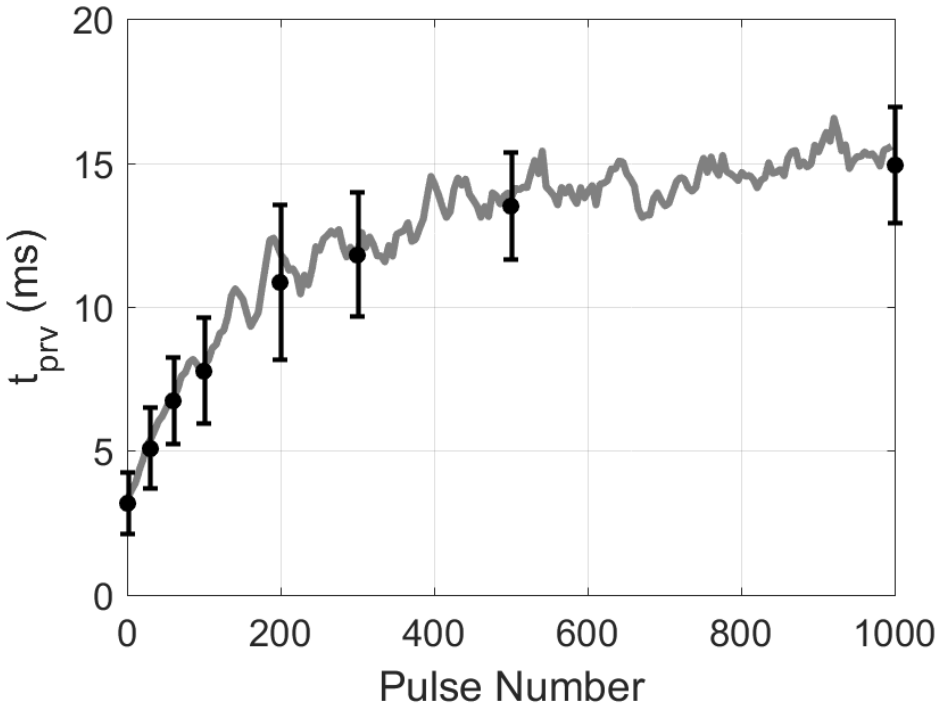

Figure 2.6: Average BCD tprv from six 1000 pulse treatments. Gray line indicates a 5-sample moving average. Black points indicate tprv at pulse numbers corresponding to the same pulse numbers used for histological analysis, i.e., 0, 30, 60, 100, 200, 300, 500, and 1000 pulse-per-location.

second positive velocity rebound was observed within the recorded 20 ms window. The time corresponding to t_{prv} for each Doppler velocity trace is also shown in Figure 2.5, and a nonlinear least squares trend line was fitted to the t_{prv} metric. In all samples, the change in the BCD t_{prv} metric exhibited mono-directional change throughout treatment and grew such that the peak negative velocity occurred later after each therapy pulse until it plateaued at around 400 pulses with a t_{prv} of approximately 16 ms.

An average of the t_{prv} metric from six 1000 pulse treatments is shown in Figure 2.6. Also shown in Figure 2.6 are the average t_{prv} found for the doses at which the histology metrics were recorded. A similar trend of increasing and plateauing t_{prv} over the treatment as Figure 2.5 is observed. It is also shown that the variance of the t_{prv} metric tends to increase throughout treatment.

This was due to the fact that the t_{prv} for each treatment reached slightly different steady states plateauing at t_{prv} values between 10 and 20 ms depending on the treatment. Previous studies in tissue-mimicking agarose phantoms also observed this phenomenon [36], suggesting that increasing liquefaction of the surrounding medium results in less consistent motion of residual cavitation nuclei.

2.3.2 Histology

In Figure 2.4, representative liver histology of normal liver and four stages after treatment are qualitatively shown: pre-treatment control (row 1), early sparse cell fractionation (row 2) generated by 30 pulses-per-location, widespread cell fractionation and partial destruction of liver architecture (row 3) generated by 100 pulses-per-location, complete cell fractionation and destruction of liver architecture and early connective tissue fractionation (row 4) generated by 300 pulses-per-location, and complete liquefaction of all cells and connective tissues (row 5) generated by 1000 pulses-per-location. In order to analyze and better visualize several varieties of tissue structures, reticulin staining (left column) and trichrome staining (right column) were used to analyze the different levels of tissue fractionation generated by histotripsy. For the first stage of treatment, at 30 pulses-per-location, only disparate regions of tissue damage have occurred. At this point, roughly 50% of the hepatocytes still appear to be intact with largely preserved liver architecture highlighted by reticulin stain and intact portal tracts with bile ducts, portal veins, portal arteries, and thick blue portal collagen fibers shown by the trichrome stain. For the second stage, by 100 pulses-per-location, significant hepatocyte and architecture destruction with loss of reticulin had occurred, and in some samples, only minimal small clusters of isolated hepatocytes with a few fractionated reticulin fibers remained in a sea of necrotic debris. The trichrome stain

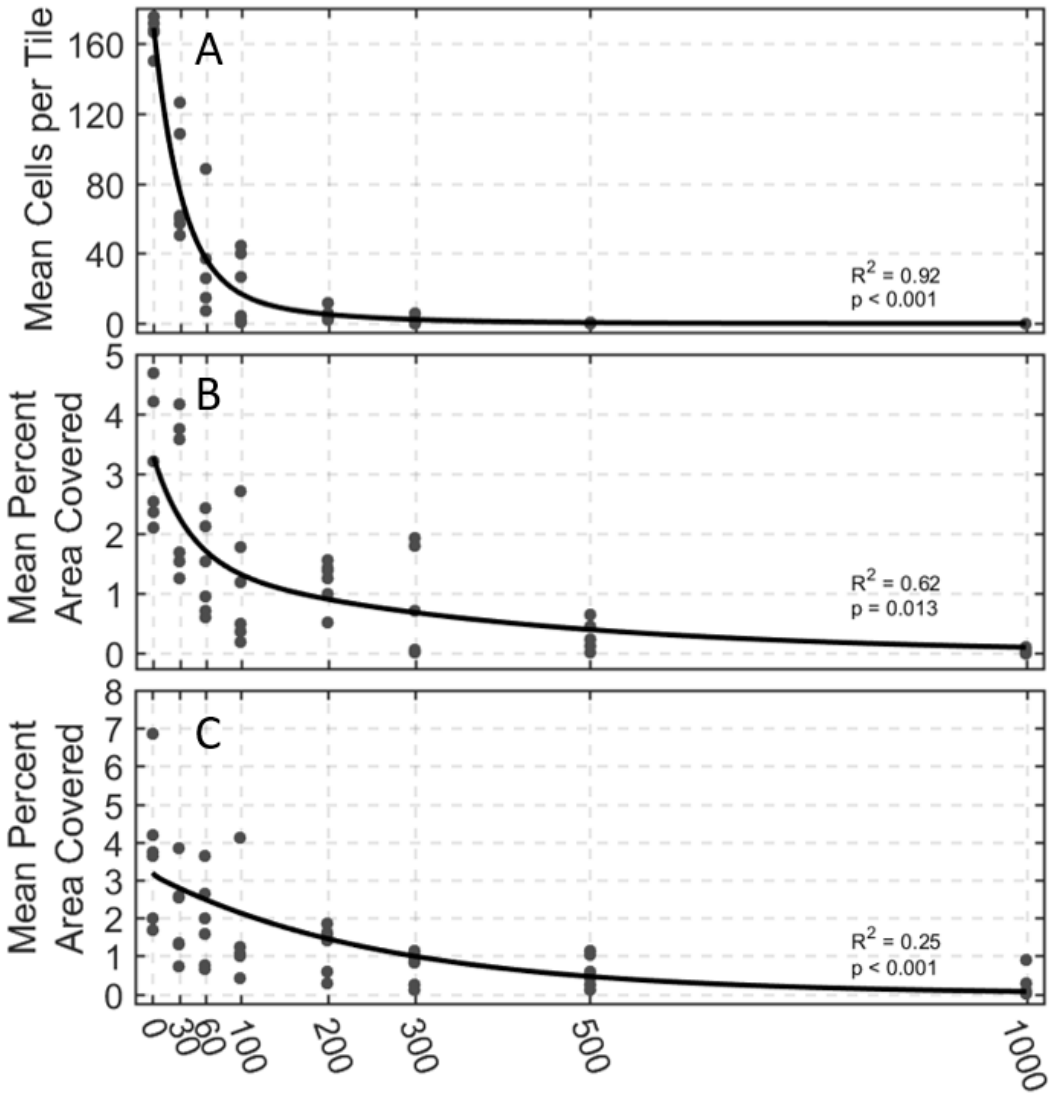

Figure 2.7: Histological analysis of 42 histotripsy treated samples at varying dosages. (A) Viable cell count remaining in imaged medium. The cell count experienced the greatest amount of destruction early in treatment. (B) Percent area with intact reticulin-stained collagen and (C) percent area with intact trichrome-stained collagen. Both collagen metrics experienced slower amounts of destruction than remaining cell count. Nonlinear least square best-fit lines are shown in black. All best fit lines exhibited statistical significance when compared to a normal distribution as indicated by the p-values on each plot.

showed that only mild to moderate portal tract and thick type I collagen fiber damage was present at 100 pulses. Interestingly, most of the remaining hepatocytes were found adjacent to the thick type I collagen fibers and portal tracts, suggesting that these collagen fibers and portal tracts acted to protect the hepatocytes from the cavitation damage. For the third stage, by 300 pulses-per-

location, virtually all hepatocytes in all treated liver samples had been destroyed including those that were adjacent to portal tracts and type I collagen fibers. Both reticulin and trichrome stains showed almost complete destruction of both type III and I collagen fibers. There were only a few scattered remnant naked nuclei in the liquefied necrotic debris, which are not viable intact cells. For the fourth stage of treatment, as shown in final row of images in Figure 2.4, at 1000 pulses-per-location, the liver tissue is completely liquefied with loss of hepatocytes and both types of collagen fibers.

The quantitative histological analyses of cell count, intact reticulin-stained collagen area, and intact trichrome-stained collagen area and their respective nonlinear least squares fits are shown in Figure 2.7. The least squares best fit lines of all three cellular metrics exhibited exponential decay to varying degrees with increasing number of histotripsy pulses applied. In these analyses, the population of viable cells in the treatment region decreases exponentially and reaches zero around 300 pulses at the latest. Both the reticulin and trichrome-stained collagen metrics take longer to reach a point at which there is virtually no reticulin or trichrome-stained collagen detected. The exponential decay time constants were found to be 38, 120, and 257 pulses for cell count, reticulin-stained collagen, and trichrome-stained collagen areas, respectively, thus supporting our hypothesis that cells are destroyed much earlier in the treatment than stronger structural connective components of the tissue.

2.3.3 Correlation Between Bubble-Induced Color Doppler and Histological Metrics

The mean values of the BCD t_{prv} were plotted against the mean values of viable cell count, reticulin-stained collagen area, and trichrome-stained collagen area in Figure 2.8A, C, and C, respectively. Linear regression was used to qualitatively indicate the fit of a linear model to the

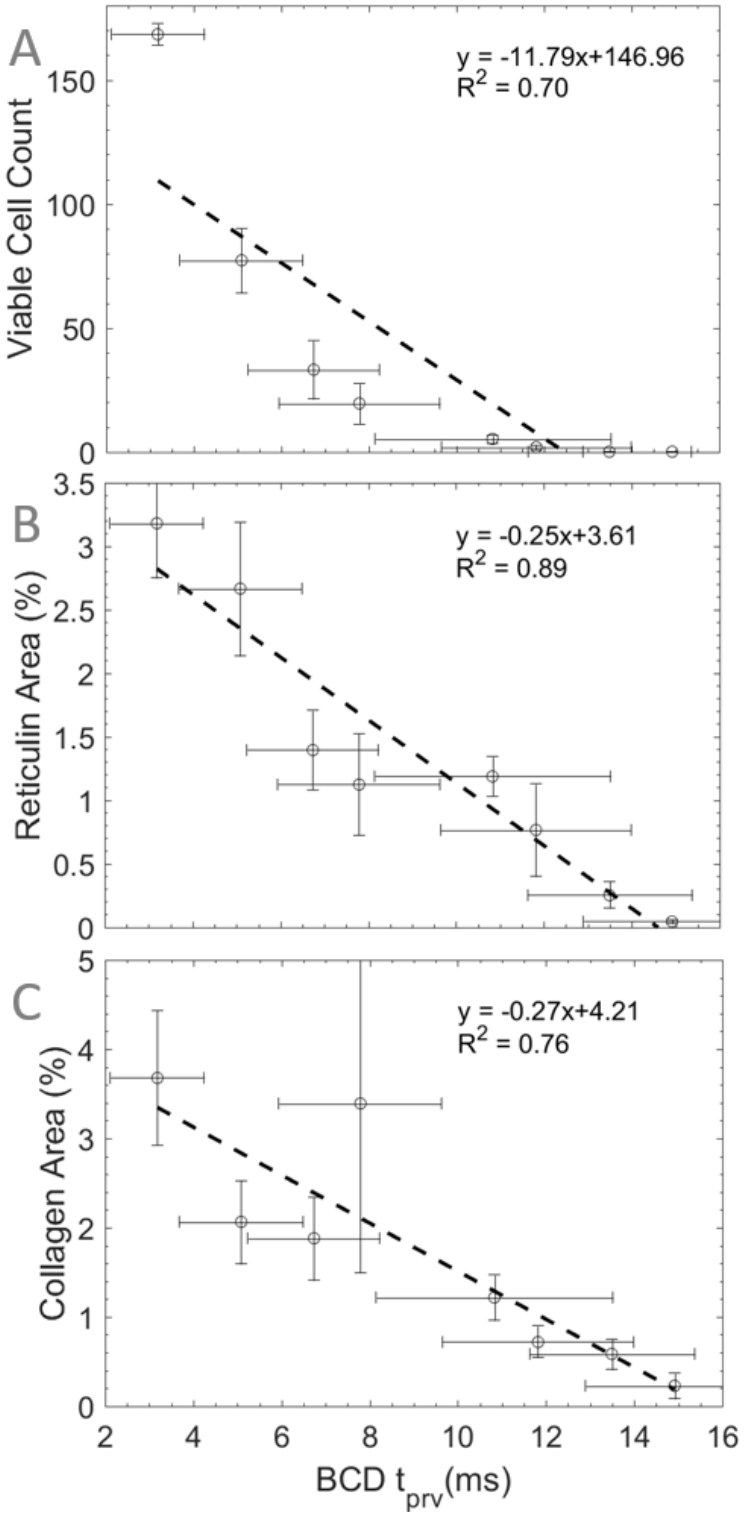

Figure 2.8: BCD t_{prv} vs. (A) viable cell count, (B) reticulin-stained area, and (C) trichrome-stained collagen area throughout 1000 pulse histotripsy treatments in bovine liver. Dashed lines indicate best-fit lines acquired using linear regression (n = 6).

relationship between these metrics. It was found that the relationship between t_{prv} and reticulin-

stained collagen resulted in the highest coefficient of determination with a value of 0.89, indicating that linear regression is a good model for this relationship. Viable cell count and trichrome-stained collagen vs. BCD t_{prv} resulted in lower coefficients of determination in comparison to reticulin-stained collagen with values of 0.70 and 0.76, respectively. This indicates that, relative to each other, the t_{prv}-reticulin relationship is better modeled by a linear relationship than the t_{prv}-viable cells and t_{prv}-trichrome relationships. The Pearson correlation coefficient analysis of the datasets returned PCCs of -0.84, -0.94, and -0.87 with p-values of 0.01, <0.001, and 0.005 for t_{prv} vs. viable cell count, reticulin-stained collagen area, and trichrome-stained collagen area, respectively (Table 2.1). This indicates that each histology metric is inversely correlated with t_{prv} to varying degrees. However, based on our chosen level of significance, only t_{prv} vs. reticulin-stained collagen resulted in a statistically significant linear correlation.

Table 2.1: Pearson Correlation Coefficients* Between BCD and Histology Metrics

	Cells Remaining	Reticulin-Stained Collagen	Trichrome-Stained Collagen
Bubble-Induced Color Doppler	-0.84 (0.010)	-0.94 (<0.001)	-0.87 (0.005)

*Values in parentheses indicate the p-value

2.4. Discussion

The results from this study support the results from all other BCD-based studies in the literature in that the BCD signal exhibited initial movement of residual cavitation nuclei away from the therapy transducer followed by a rebound back towards the transducer and that the BCD t_{prv} metric exhibited mono-directional growth in time [22, 27, 36]. While the reason for this reproducible directionality of residual nuclei movement has not yet been completely verified experimentally for histotripsy, existing theoretical and experimental work into the physics of the

non-spherical cavitation-bubble collapse is able to provide some insight. Previously, it has been shown that the collapse of the cavitation-bubble results in the formation of a liquid jet and an impulsive pressure release. The jet subsequently penetrates the bubble resulting in damage to the surrounding medium [37, 38, 39, 40, 41, 42, 43, 44]. It is believed that this non-spherical collapse and liquid jet is caused by a non-uniform pressure distribution around the bubble, which can be induced by the presence of a solid object or free surface, buoyancy, or interactions with shockwaves such as those in histotripsy [45, 46, 47, 48, 49]. During a non-spherical collapse, there is a non-zero Kelvin impulse, i.e., non-zero bubble inertia [50, 51, 52], which has been shown to correlate with bubble cloud migration and flow [53, 54]. Due to the fact that the BCD-measured movement is only observed when cavitation occurs, this suggests that acoustic radiation force is not the primary mechanism of movement. Furthermore, our unpublished data suggest that the asymmetric growth and collapse of the cavitation results in a fast net motion of the cavitation bubbles. The inertia from this fast motion can last for over 20 ms, moving persistent residual nuclei, which is detected as the BCD signal. Therefore, we hypothesize that the transfer of momentum from the Kelvin impulse to the surrounding tissue caused by non-spherical cavitation-collapse may be a primary mechanism for the BCD-detected oscillation of residual cavitation nuclei. Future experimental studies will test this hypothesis.

Tissues with lower elasticities result in bubbles that grow larger and last longer. As tissue elasticity decreases throughout histotripsy treatment until the tissue is completely liquefied, we hypothesize that the movement of the cavitation nuclei sustains longer as tissue is fractionated by histotripsy. The increase in t_{prv} observed throughout treatment indicates that the frequency of oscillation of the movement of residual nuclei is decreasing throughout treatment, which corresponds to the decreased tissue elasticity. The increased variability of the t_{prv} metric as the

treatment progresses has also been reported previously. This is likely due to the fact that bubble cloud formation is less consistent from one pulse to the next when forming in a liquid environment with increasing spatial variability of acoustic backscatter off the bubble cloud with increasing tissue homogenization [55]. An increase in variable bubble cloud formation would also result in an increase in the variability of movement of residual nuclei in the treated volume from pulse to pulse.

The three histological components extracted from histology in this study were chosen to analyze weak, moderate, and strong components of the liver tissue that have varying resistance to histotripsy-induced tissue fractionation. Cells highlighted by hematoxylin in the trichrome stained tissue samples were used as the weak component. Reticulin-stained collagen is an extracellular structure stained by silver particles in the reticulin stain, which is stronger than cells but weaker and more homogenously distributed throughout the liver tissue than the thicker type I collagen fibers highlighted by the trichrome stain. Reticulin-stained fibers are small branching structures made primarily of type III collagen that are ubiquitously found throughout the extracellular matrix in many tissues including liver [56]. The results clearly show that histotripsy destroys cells first, then weaker extracellular matrix materials such as reticulin-stained collagen, and finally stronger extracellular matrix materials such as trichrome-stained collagen. These results also directly support the results from [36] in which virtually no intact viable cells were observed after 200 to 300 therapy pulses for *ex vivo* bovine liver. In order to destroy something such as a tumor, only cellular destruction is required. However, here we have found that hepatocytes that reside close to stronger structures such as trichrome-stained collagen or portal tracts are able to sustain higher histotripsy dosages than those that are not. Thus, the collagenous and connective tissue characteristics may impact the treatment required for appropriate cellular destruction. Due to the

fact that different patients and tissues have varying tissue matrix characteristics, a real-time feedback mechanism for collagen structure destruction may provide a quantitative indication of treatment progression with patient and tissue specificity.

Previous studies have indicated that the BCD t_{prv} metric is correlated with the number of intact cells remaining. However, due to the fact that bubble dynamics are more closely influenced by structural components of tissue and cells are less of a contributing factor to the mechanical properties of tissue than collagen, we hypothesized that the BCD signal would correlate more with the destruction of structural components of tissue. The observed BCD signals and histology in this study support this hypothesis by showing that the change in the BCD t_{prv} metric has a statistically significant inverse correlation with reticulin-stained collagen components identified histologically. The inverse nature of this correlation is primarily a product of how the data is presented and should not be seen as a disadvantage. The PCC of the t_{prv} with both intact cells remaining and trichrome-stained collagen area were both found to be statistically insignificant, thus indicating that they are not linearly correlated with the t_{prv} metric. Although trichrome-stained collagen certainly contributes to the overall macrostructure of liver, trichrome-stained collagen bundles only occur in thick, sparse bundles, and they often do not contribute to the local, microstructure of the tissue treated in these experiments. Therefore, there were locations within the treated tissue where virtually no trichrome-stained collagen existed. We hypothesize that this sparse distribution of trichrome-stained collagen is what may have led to its lower correlation with t_{prv} than reticulin-stained collagen. Additionally, the variance in the trichrome-stained collagen metrics was higher than the other two histology metrics. We also attribute this high variance to the sparseness of the trichrome-stained collagen, for some histology tiles contained almost no trichrome-stained collagen while others were virtually filled with trichrome stained collagen. Furthermore, we now

hypothesize that tissues with more densely packed collagen of both type I and type III would result in a slower change of t_{prv} due to an increase in the amount of histotripsy required for complete liquefaction. An indicator for collagen-embedded tissue destruction is important due to the observed shielding of hepatocytes near collagen structures. Thus, using BCD as an indicator of complete collagen destruction would be a good indicator of tissue ablation, i.e., complete cell death thus eliminating the need to over treat tissue while ensuring that the target tissue has been completely homogenized to the necessary degree. Due to the fact that connective tissues are generally high in collagen, this indicates that the t_{prv} of the BCD signal may be able to track treatment progression in patients with varying collagen matrix profiles.

2.5. Conclusions

In this study, we investigated the use of bubble-induced color Doppler received by a separate linear imaging probe to monitor the levels of tissue fractionation induced by histotripsy therapy in bovine *ex vivo* liver. Histology was acquired at various dosages throughout treatment, and three metrics were used to identify the extent of destruction of various types of tissues with varying degrees of mechanical strength. It was found that the t_{prv} of the BCD signal had a statistically significant linear correlation with reticulin-stained collagen destruction, indicating that changes in the BCD signal are more closely related to the structural components of tissue rather than cellular destruction. These results suggest that BCD may be able to provide noninvasive and quantitative monitoring of tissue mechanical integrity during histotripsy therapy.

2.6. References

[1] J. Macoskey, X. Zhang, T. Hall, J. Shi, S. Beig, E. Johnsen, F. Lee Jr., C. Cain and Z. Xu, "Bubble-Induced Color Doppler Feedback Correlates with Histotripsy-Induced

Destruction of Structural Components in Liver Tissue," Ultrasound in Med. & Biol., vol. 44, no. 3, pp. 602-12, 2018a.

[2] Z. Xu, T. Hall, J. B. Fowlkes and C. A. Cain, "Effects of acoustic parameters on bubble cloud dynamics in ultrasound tissue erosion (histotripsy)," J. Acoust. Soc. Am., vol. 122, no. 1, pp. 229-236, July 2007.

[3] K.-W. Lin, Y. Kim, A. D. Maxwell, T.-Y. Wang, T. L. Hall, Z. Xu, B. J. Fowlkes and C. A. Cain, "Histotripsy beyond the intrinsic cavitation threshold using very short ultrasound pulses: Microtripsy," IEEE Trans. Ultrason., Ferroelect., Freq. Control, vol. 61, no. 2, pp. 251-265, February 2014.

[4] X. Zhang, G. E. Owens, C. A. Cain, H. S. Gurm, J. Macoskey and Z. Xu, "Histotripsy Thrombolysis on Retracted Clots," Ultrasound Med. Biol., vol. 42, no. 8, pp. 1903-1918, August 2016.

[5] X. Zhang, J. Macoskey, K. Ives, G. Owens, H. Gurm, J. Shi, M. Pizzuto, C. CA and Z. Xu, "Non-Invasive Thrombolysis Using Microtripsy in a Porcine Deep Vein Thrombosis Model," Ultrasound Med. Biol., vol. 43, no. 7, pp. 1378-90, 2017.

[6] E. Vlaisavljevich, Y. Kim, S. Allen, S. Pelletier, C. Cain, K. Ives and Z. Xu, "Image-Guided Non-Invasive Ultrasound Liver Ablation Using Histotripsy: Feasibility Study in an In Vivo Porcine Model," Ultrasound Med. Biol., vol. 39, no. 8, pp. 1398-1409, August 2013.

[7] W. Roberts, "Focused ultrasound ablation of renal and prostate cancer: Current technology and future directions," Urol. Oncol., vol. 23, no. 5, pp. 367-371, 2005.

[8] G. R. Schade, J. Keller, I. Kimberly, X. Cheng, T. J. Rosol and W. W. Roberts, "Histotripsy focal ablation of implanted prostate tumor in an ACE-1 canine cancer model," J. Urol., vol. 188, no. 5, pp. 1957-1964, November 2012.

[9] Z. Xu, A. Ludomirsky, L. Y. Eun, T. L. Hall, B. C. Tran, B. J. Fowlkes and C. A. Cain, "Controlled Ultrasound Tissue Erosion," IEEE Trans. Ultrason., Ferroelect., Freq. Control, vol. 51, no. 6, pp. 726-736, June 2004.

[10] Y. Kim, T. L. Hall, Z. Xu and C. A. Cain, "Transcranial histotripsy therapy: A feasibility study," IEEE Trans. Ultrason., Ferroelect., Freq. Control, vol. 61, no. 4, pp. 582-593, April 2014.

[11] K. Hynynen, A. Darkazanli, E. Unger and J. Schenck, "MRI-guided noninvasive ultrasound surgery," Medical Physics, vol. 20, no. 1, pp. 107-115, 1993.

[12] N. McDannold, K. Hynynen, D. Wolf, G. Wolf and F. Jolesz, "MRI Evaluation of Thermal Ablation of Tumors with Focused Ultrasound," J. Magn. Reson. Imaging, vol. 8, no. 1, pp. 91-100, February 1998.

[13] S. P. Allen, W. W. Roberts, T. L. Hall, C. A. Cain and L. Hernandez-Garcia, "Characterization of the in vivo Histotripsy Lesion Using High Field MRI," in Proceedings, International Society for Magnetic Resonance in Medicine 20th Annual Meeting and Exhibition, Melbourne, Austrialia, 2012.

[14] N. Lipsman, S. ML, Y. Huang, L. Lee, T. Sankar, M. Chapman, K. Hynynen and L. AM, "MR-guided focused ultrasound thalamotomy for essential tremor: A proof-of-concept study," Lancet Neurol., vol. 12, no. 5, pp. 462-468, 2013.

[15] M. Gyöngy and C.-C. Coussios, "Passive Spatial Mapping of Inertial Cavitation During HIFU Exposure," IEEE Trans. Biomed. Eng., vol. 57, no. 1, pp. 48-56, January 2010.

[16] G. Owens, R. Miller, G. Ensing, K. Ives, D. Gordon, A. Ludomirsky and Z. Xu, "Therapeutic ultrasound to non-invasively create intracardiac communications in an intact animal model.," Catheter Cardiovasc. Interv., vol. 77, no. 4, pp. 580-8, 2011.

[17] C. Farny, G. Holt and R. Roy, "Monitoring the Development of HIFU-Induced Cavitation Activity," AIP Conf Proc, vol. 829, pp. 348-52, 2006.

[18] G. Owens, R. Miller, S. Owens, S. Swanson, K. Ives, G. Ensing and D. X. Z. Gordon, "Intermediate-term effects of intracardiac communications created noninvasively by therapeutic ultrasound (histotripsy) in a porcine model," Pediatric Cardiology, vol. 33, no. 1, pp. 83-9, 2012.

[19] Z. Xu, F. Zhenzhen, T. L. Hall, F. Winterroth, B. J. Fowlkes and C. A. Cain, "Size Measurement of Tissue Debris Particles Generated from Pulsed Ultrasound Cavitational Therapy - Histotripsy," Ultrasound Med. Biol., vol. 35, no. 2, pp. 245-255, February 2009.

[20] T. Hall, J. Fowlkes and C. Cain, "A real-time measure of cavitation induced tissue disruption by ultrasound imaging backscatter reduction," IEEE Trans. Ultrason., Ferroelect., Freq. Control, vol. 54, no. 3, pp. 569-75, 2007b.

[21] T.-Y. Wang, F. Winterroth, T. L. Hall, B. J. Fowlkes, E. D. Rothman, W. W. Roberts and C. A. Cain, "Quantitative ultrasound backscatter for pulsed cavitational ultrasound therapy-histotripsy," IEEE Trans. Ultrason., Ferroelect., Freq. Control, vol. 56, no. 5, pp. 995-1005, May 2009.

[22] R. Miller, A. Maxwell, T.-Z. Wang, J. Fowlkes, C. Cain and Z. Xu, "Real-time elastography-based monitoring of histotripsy tissue fractionation using color Doppler," in IEEE International Ultrasonics Symposium, Dresden, Germany, 2012.

[23] T.-Z. Wang, T. Hall, Z. Xu, J. Fowlkes and C. Cain, "Imaging feedback of histotripsy treatments using ultrasound shear wave elastography," IEEE Trans. Ultrason., Ferroelect., Freq. Control, vol. 59, no. 6, pp. 1167-81, 2012a.

[24] T.-Z. Wang, T. Hall, Z. Xu, J. Fowlkes and C. Cain, "Imaging feedback for histotripsy by characterizing dynamics of acoustic radiation force impulse (ARFI)-induced shear waves excited in a treated volume," IEEE Trans. Ultrason., Ferroelect., Freq. Control, vol. 61, no. 7, pp. 1137-1151, 2014.

[25] C. Cain and T.-Z. Wang, "Imaging feedback of histotripsy treatments with ultrasound transient elastography". United States Patent US 20130102932 A1, 10 Oct 2012.

[26] T.-Z. Wang, Z. Xu, T. Hall, J. Fowlkes and C. Cain, "An efficient treatment strategy for histotripsy by removing cavitation memory," Ultrasound Med. Biol., vol. 38, no. 5, pp. 753-766, 2012b.

[27] X. Zhang, R. M. Miller, K.-W. Lin, A. M. Levin, G. E. Owens, H. S. Gurm, C. A. Cain and Z. Xu, "Real-Time Feedback of Histotripsy Thrombolysis Using Bubble-Induced Color Doppler," Ultrasound Med. Biol., vol. 41, no. 5, pp. 1389-1401, May 2015.

[28] R. Miller, Z. X, M. AD, C. CA and X. Z, "Bubble-Induced Color Doppler Feedback for Histotripsy Fractionation," IEEE Trans Ultrason Ferroelectr Freq Control, vol. 63, no. 3, pp. 408-19, 2016.

[29] J. Macoskey, J. Sukovich, T. Hall, C. Cain and Z. Xu, "Real-time acoustic-based feedback for histotripsy therapy," in 173rd Meeting of the Acoustical Society of America, Boston, MA, 2017.

[30] T. Khokhlova, M. Canney, V. Khokhlova, O. Sapozhnikov, L. Crum and M. Bailey, "Controlled tissue emulsification produced by high intensity focused ultrasound shock waves and millisecond boiling," J. Acoust. Soc. Am., vol. 130, pp. 3498-3510, 2011.

[31] E. Vlaisavljevich, A. Maxwell, M. Warnez, E. Johnsen, C. Cain and Z. Xu, "Histotripsy-induced cavitation cloud initiation thresholds in tissues of different mechanical properties," IEEE Trans. Ultrason., Ferroelect., Freq. Control, vol. 61, no. 2, pp. 341-52, 2014.

[32] J. Fowlkes and L. Crum, "Cavitationa threshold measurements for microsecond length pulses of ultrasound," J. Acoust. Soc. Am., vol. 83, no. 6, pp. 2190-2201, June 1988.

[33] A. Duryea, H. Tamaddoni, C. Cain and W. H. T. Roberts, "Removal of residual nuclei following a cavitation event: a parametric study," IEEE Trans. Ultrason. Ferroelectr. Freq. Control, vol. 62, no. 9, pp. 1605-1614, September 2015b.

[34] J. E. Parsons, C. A. Cain and J. B. Fowlkes, "Cost-effective assembly of a basic fiber-optic hydrophone for measurement of high-amplitude therapeutic ultrasound fields," J. Acoust. Soc. Am., vol. 119, pp. 1432-1440, March 2006b.

[35] H. Gordon and H. Sweets, "A Simple Method for the Silver Impregnation of Reticulum," Am. J. Pathol., vol. 12, no. 4, p. 545, 1936.

[36] R. Miller, Z. Zhang, A. Maxwell, C. Cain and Z. Xu, "Bubble-Induced Color Doppler Feedback for Histotripsy Fractionation," IEEE Trans. Ultrason., Ferroelect., Freq. Control, vol. 63, no. 3, pp. 408-19, 2016.

[37] Y. Tomita and A. Shima, "Mechanisms of impulsive pressure generation and damage pit formation by bubble collapse," J. Fluid Mech., vol. 169, pp. 535-564, 1986.

[38] A. Coleman, J. Saunders, L. Crum and M. Dyson, "Acoustic Cavitation Generated by an Extracorporeal Shockwave Lithotripter," Ultrasound Med. Biol., vol. 13, pp. 69-76, 1987.

[39] L. Crum, "Cavitation Microjets as a Contributory Mechanism for Renal Calculi Disintegration in ESWL," J. Urol., vol. 140, pp. 1587-1590, 1988.

[40] J. Dear and J. Field, "A study of the collapse of arrays of cavities," J. Fluid Mech., vol. 190, pp. 409-425, 1988.

[41] J. Field, "The physics of liquid impact, shock wave interactions with cavities, and the implications to shock wave lithotripsy," Phys. Med. Biol., vol. 36, pp. 1475-1484, 1991.

[42] N. Bourne and J. Field, "Shock-induced collapse of single cavities in liquids," J. Fluid Mech., vol. 244, pp. 225-240, 1992.

[43] E. Johnsen and T. Colonius, "Shock-induced collapse of a gas bubble in shockwave lithotripsy," J. Acoust. Soc. Am., vol. 124, pp. 2011-2020, 2008.

[44] E. Johnsen and T. Colonius, "Numerical simulations of non-spherical bubble collapse," J. Fluid Mech., vol. 629, pp. 231-262, 2009.

[45] W. Lauterborn and H. Bolle, "Experimental investigations of cavitation-bubble collapse in the neighbourhood of a solid boundary," J. Fluid Mech., vol. 72, no. 2, pp. 391-399, 1975.

[46] A. Philipp and W. Lauterborn, "Cavitation erosion by single laser-produced bubbles," J. Fluid Mech., vol. 361, pp. 75-116, 1998.

[47] C. Ohl and R. Ikink, "Shock-wave-induced jetting of micron-sized bubbles," Phys. Rev. Lett., vol. 90, p. 214502, 2003.

[48] D. Obreschkow, M. Tinguely, N. Dorsaz, P. Kobel, A. de Bosset and M. Farhat, "Universal scaling law for jets of collapsing bubbles," Phys. Rev. Lett., vol. 107, pp. 1-5, 2011.

[49] J. Dear, J. Field and A. Walton, "Gas compression and jet formation in cavities collapse by a shock wave," Nature, vol. 332, pp. 505-508, 1988.

[50] J. Blake, "The Kelvin Impulse: Applications to Bubble Dynamics," Eigth Australasian Fluid Mechanics Conference, pp. 10B.1-10B.4, 1983.

[51] J. Blake, "The Kelvin impulse: Application to cavitation bubble dynamics," The Journal of the Australian Mathematical Society, vol. 30, no. 2, pp. 127-146, 1988.

[52] J. Blake, D. Leppinen and Q. Wang, "Cavitation and bubble dynamics: the Kelvin impulse and its applications," Interface Focus, vol. 5, pp. 1-15, 2015.

[53] J. Blake, B. Taib and G. Doherty, "Transient cavities near boundaries. Part 1. Rigid boundary," J. Fluid Mech., vol. 170, pp. 479-497, 1986.

[54] J. Blake and D. Gibson, "Cavitation bubbles near boundaries," Ann. Rev. Fluid Mech., vol. 19, pp. 99-123, 1987.

[55] J. Parsons, C. Cain and B. Fowlkes, "Spatial Variability in Acoustic Backscatter as an Indicator of Tissue Homogenate Production in Pulsed Cavitational Ultrasound Therapy," IEEE Trans. Ultrason., Ferroelect., Freq. Control, vol. 54, no. 3, pp. 576-590, March 2007.

[56] K. Little and H. Kramer, "Nature of Reticulin," Nature, vol. 170, no. 4325, pp. 499-500, September 1952.

CHAPTER 3

Development of an Integrated Receive-Capable Histotripsy System

3.1. Introduction

The advent of Bubble-Induced Color Doppler (BCD) solved several problems of other histotripsy treatment monitoring modalities [1]. In comparison to MRI-guided focused ultrasound, BCD does not require an MRI scanner nor an MRI-compatible histotripsy system. In comparison to B-mode imaging and ultrasound elastography, BCD has higher sensitivity to treatment progression at the beginning stages of treatment when B-mode is insensitive, and BCD also has higher sensitivity to treatment progression during the later stages of treatment progression when the principles of ultrasound elastography break down and prevent accurate viscoelastic measurements. However, BCD still fails to solve several important issues with histotripsy feedback: 3D monitoring, and the necessity of additional imaging equipment. While a 2D ultrasound imaging array could be potentially introduced to solve the 3D monitoring issue, the amount of data generated for BCD in the 2D regime is already on the order of tens to hundreds of gigabytes per treatment, so much more advanced high-performance computing architecture would have to be developed to even enable 3D BCD research.

The transducers in histotripsy systems are built from the same family of piezoceramic materials from which typical clinical ultrasound probes are built. This means that histotripsy transducers have the ability to both transmit and receive ultrasound. However, histotripsy systems have traditionally been transmit-only systems for several reasons. First, typical histotripsy

transducers are highly focused and have very large, low frequency elements and element spacings that are several times the standard λ/2 distance used in imaging systems. This means that any imaging performed with a histotripsy transducer would experience severe grating lobes thus rendering any acquired images seemingly useless. Histotripsy transducers are therefore obviously quite sub-optimal for imaging. However, this does not mean that receive-capable histotripsy transducers would not be helpful for histotripsy feedback. Second, histotripsy systems employ high-voltage driver systems that output pulses of upwards of 3 kV per channel, and the acoustic signals that would be useful to receive are on the order tens to hundreds of Volts at most. Therefore, a receive system would have to overcome both high-voltage isolation and high-dynamic range issues in addition to acquiring data from hundreds of channels simultaneously. Due to both these acoustic and technological issues, histotripsy systems to this point have all been designed as transmit-only systems, and all feedback has been left to secondary imaging equipment.

Recently, other research cohorts have developed receive-capable therapeutic ultrasound systems for HIFU therapy, which have frequently been referred to as "dual-mode" ultrasound array (DMUA) systems. Some systems, such as that found in [2], use a secondary imaging probe that is embedded in the middle of a therapeutic ultrasound array. While these transducers are controlled by the same system, this does not allow for the therapy transducer itself to receive ultrasound. Other studies have disclosed true receive-capable HIFU systems that incorporate transmit and receive electronics for tens to hundreds of ultrasound elements [3, 4, 5]. While these systems were successful and proved to be useful in tracking various physiological structures, they operated at lower electrical powers than histotripsy systems and were therefore able to use off-the-shelf transmit-receive switch electronics. Most recently, a system designed for transcranial thermal applications was developed to transmit on 256 channels and receive on up to 64 channels [6]. This

system used a variety of custom electronics to enable receive capability for their custom ultrasound array including the Texas Instruments AFE5808 and a cascaded array of Altera FPGAs to acquire up to 200 μs of data on each receive channel at up to a 40 MHz sampling frequency. However, in addition to this system being designed for thermal therapies in which the power levels on the transducer were less intense than in histotripsy, this system was USB controlled which was a likely data bottleneck. Furthermore, this system required a sundry of matching electronics which may have also limited the number of possible receive channels. For histotripsy, this amount of receive time would be acceptable, as the round-trip acoustic propagation time between the array elements and the focus for histotripsy arrays is often around 200 μs. However, for many applications such as aberration correction, it is necessary to receive on all channels, and a receiver system must also be able to withstand the high power levels of histotripsy driving systems.

Histotripsy systems destroy tissue by inducing a cloud of inertially cavitating microbubbles that mechanically lyse cells in the target region [7, 8, 9]. As will be further discussed in chapters 4 and 5, inertially cavitating microbubbles induce complex acoustic emissions that can be detected by ultrasonic receivers including histotripsy systems [10, 11]. Upon initiation caused by the arrival of a high-pressure peak-negative pulse of ultrasound, existing microbubbles and gas pockets on cavitation nuclei expand rapidly to several orders of magnitude larger than their original size [12, 13]. For a single bubble, during the period of highest bubble-wall acceleration (at which point the bubble wall is traveling at a velocity higher than the speed of sound in the medium), a shockwave is emitted that is focused about the geometric center of the bubble [14, 15, 16]. The bubble continues to grow until it reaches a maximum radius, R_{max}, at which point it begins to collapse inward upon itself. During the final stages of this collapse when the bubble radius is immeasurably small, another shockwave is released [17, 18]. For clouds of cavitating bubbles, a complex series

of shockwaves are emitted, and these are collectively referred to as acoustic cavitation emission (ACE) signals [10, 19, 20]. The usefulness of these ACE signals for histotripsy feedback will be discussed later in this dissertation. For the purposes of this chapter, however, all that is important to note about these signals is that we must develop a way to measure these signals with histotripsy transducers.

This chapter is split into three sections. First, in Section 3.2, this chapter will discuss several important prototypes that led to the development of the current state-of-the-art receive-capable histotripsy system at a high level. Second, in Section 3.3, this chapter will discuss in detail the technical aspects of the first fully-functioning histotripsy receiver prototype used in [11]. Third, in Section 3.4, the technical details of the current state-of-the-art integrated receive-capable histotripsy system will be discussed.

3.2. List of Notable Prototypes

The design challenges associated with developing the first-ever receive-capable histotripsy system required a multitude of design tests and revisions before a complete design could be realized. From the initial proof-of-concept design to the final fully-integrated receive-capable system, over ten unique prototype systems were designed, built, and tested. The purpose of this section is to highlight some key prototypes and orient the reader as to the preliminary work that preceded the systems that were capable of true receive-capable histotripsy. Technical details will begin in Section 3.3.

3.2.1 Eight-Channel Passive Receiver: Purple Board

The first working prototype for the receive system, the Purple Board, was an 8-channel analog, passive circuit that implemented nonlinear compression of high voltage waveforms. Nonlinear compression was realized via a diode-capacitor voltage divider that compressed all signals above approximately 0.7 Volts. The nonlinear compression circuitry will be discussed in detail in Section 3.3. This prototype was intended to be used in conjunction with two four-channel oscilloscopes to collect data from eight channels of a histotripsy array. Notably, this was the first printed circuit board designed and constructed by the author (Figure 3.1). This prototype was used in part to collect the data used in [21, 19]. A detailed schematic of this circuit is shown in Figure 3.6.

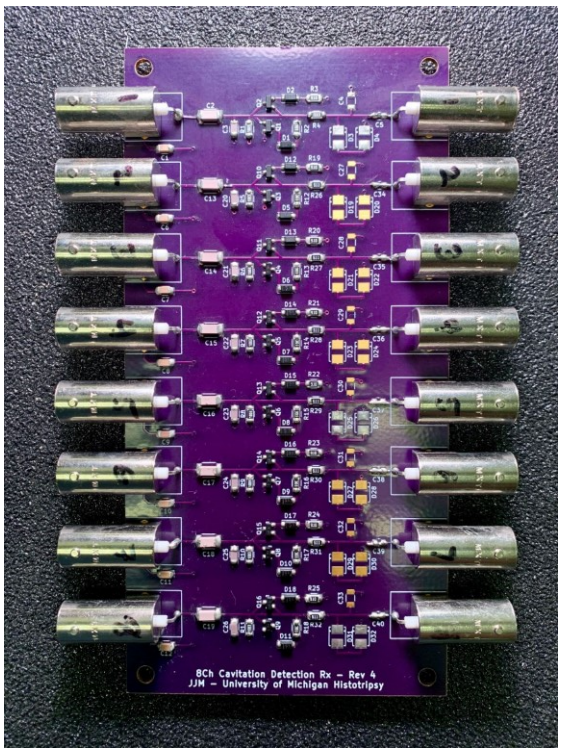

Figure 3.1: Purple Board prototype with eight populated passive receive channels.

Figure 3.2: Verasonics receive-system prototype including the 128-channel breakout board (right) connected to the standard 128-channel ultrasound connector on the Verasonics transmit-and-receive system.

3.2.2 Verasonics System

In order to collect data from a large histotripsy system rather than a subset of eight channels, a receiver system capable of acquiring data from hundreds of channels simultaneously needed to be devised in addition to the nonlinear voltage compression circuitry developed with the Purple Board (and discussed in detail in Section 3.3). Due to what were seen at the time to be large overhead costs of both funding and time associated with developing a custom digitized receiver system, the decision was made to use an existing ultrasound acquisition system as the core data management device. A Verasonics Imaging System (SS number: 1634; Verasonics, Inc., Redmond, WA, USA) with 128 transmit and receive channels was connected to a custom 128-channel breakout board designed by colleagues at the University of Washington that allowed each

channel of the Verasonics system to be individually addressed via a coaxial connector. The initial idea was to attach a larger version of the nonlinear voltage compressor to this breakout board or to develop a new breakout board that incorporated these electronics. If successful, this system would have allowed for acquisition of up to 128 channels of a histotripsy system when also integrated with a nonlinear voltage compressor for each channel. However, this prototype failed due to some intrinsic restrictions of the Verasonics system caused by firmware intended to protect the sensitive receive electronics. To attach a custom array to the Verasonics system, the system firmware requires the user to develop a custom transducer profile that initializes the system parameters for channel count and sampling frequency as well as several other parameters. This custom profile significantly limits the overall functionality of the system. For example, the sampling frequency was limited to 10 MHz when only using a small number of channels, and was dropped down to 5 MHz or less to acquire more data. Furthermore, the available sampling frequencies were set to certain pre-determined levels rather than a custom rate between some given range. Additionally, this particular Verasonics system allowed for 128 simultaneous transmit channels but only 64 simultaneous received channels (this system uses a multiplexer to alternate between banks of 64 channels when acquiring ultrasound data from a typical ultrasound probe such as a standard 128-channel L7-4 probe). While the Verasonics systems are clearly optimized for custom ultrasound imaging applications, they cannot be treated as generalized multi-channel data acquisition systems. The result of this prototype was the realization that the development of a custom receive circuit with parallel digitization of hundreds of channels for histotripsy feedback was necessary.

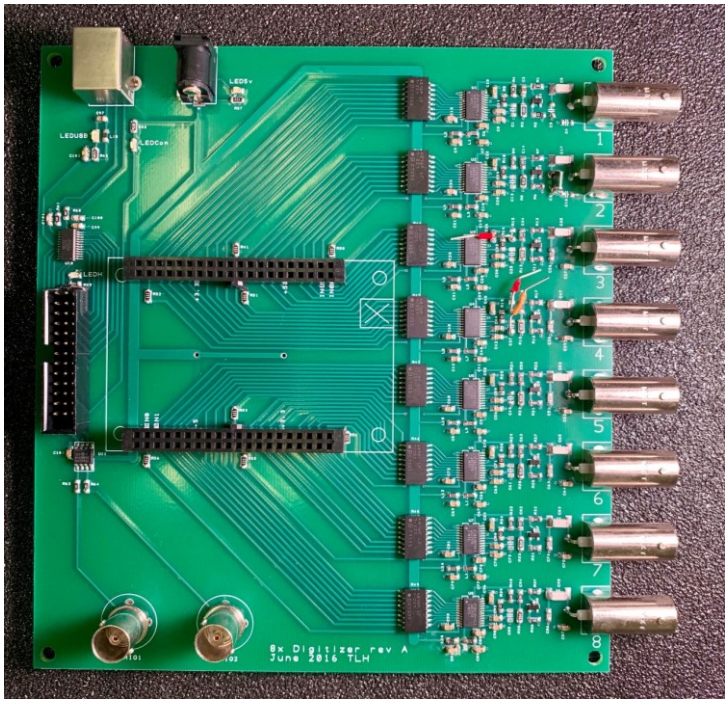

Figure 3.3: 8-channel digital receive system with analog nonlinear voltage compressor front-end. DE0-Nano FPGA module was attached to the two black 40-pin headers during operation.

3.2.3 Eight-Channel ADC1175 Evaluation Module

In order to 1) test the ability of an analog-to-digital converter (ADC) to collect acoustic data after the nonlinear voltage compressor and 2) test the ability for a field-programmable gate array (FPGA) to acquire data from multiple ADCs simultaneously, an 8-channel digital receiver evaluation module was designed, built, and extensively tested (Figure 3.3). The ADC chosen was a 1-channel, 8-bit ADC with a 20 MHz sampling rate (ADC1175, Texas Instruments, Inc., Dallas, TX, USA). This ADC is discussed in greater detail in Section 3.3. Each ADC was fed into eight general purpose input/output (GPIO) pins of an FPGA (Cyclone IV, Intel Corporation, Santa Clara, CA, USA) that was embedded on a breakout board (DE0-Nano, Terasic, Inc. Hsinchu, Taiwan) that allowed for simple integration with the custom PCB in Figure 3.3 using two 40-pin headers. Data was transmitted from the FPGA to a master control computer via USB. While this prototype was successful in the simultaneous acquisition of eight histotripsy channels, the primary

conclusion from this prototype was that while USB data speeds are fast enough to transmit large amounts of data, this solution does not scale as (1) USB hubs with dozens of inputs are not available and (2) communicating with dozens of individual USB devices to receive data in parallel would result in a data acquisition bottleneck. Therefore, in order to implement real-time feedback, a faster data transmission method was required.

3.2.4 Standalone Multi-Channel Receiver: Retrofit System

The Retrofit System (Figure 3.4) was the first successful receive-capable histotripsy system and is discussed in detail in Section 3.3. The design of this prototype allowed any existing histotripsy system to be retrofitted with receive-capability. The front end of this prototype used the same analog front end and ADC from the Eight-Channel ADC1175 Evaluation Module but with an upgraded FPGA chip (Cyclone V SoC, Intel Corporation, Santa Clara, CA, USA) embedded on a higher-performance breakout board (DE0-Nano SoC, Terasic, Inc. Hsinchu, Taiwan), which, importantly, included gigabit Ethernet hardware that was used to transmit data from all FPGAs in a system. The first version of this system used 14 8-channel FPGA/SoC modules in parallel to acquire data from an existing 112-channel histotripsy system. This system was used in [11]. Versions of this system were also built to receive-enable a 256-channel, 500-kHz hemispherical transcranial histotripsy array and a 32-element, 1-MHz spherical histotripsy transducer, which were both used to collect the data used in two manuscripts in preparation.

Figure 3.4: The Retrofit System integrated with a 112-channel, 500-kHz histotripsy array. Input data to the receive system is transmitted via the black BNC cables on the left and right sides of the system, and data transmission between the FPGA/SoC modules and the master computer occurs via the yellow Ethernet cables in the middle.

3.2.5 Fully Receive-Capable Integrated Histotripsy System: Poseidon

Project Poseidon is a fully functional transmit- and receive-capable system that is able to drive any histotripsy array up to 512 channels and is discussed in detail in Section 3.4. Both the ADC and FPGA/SoC modules used in Poseidon are upgraded versions of those used in the Retrofit System. The integrated nature of this system allows for simultaneous control of both the transmit and receive capabilities of the system thus enabling a multitude of histotripsy experiments that

were not previously possible. An image of one 8-channel board of this system is shown in Figure 3.5. Schematic-level diagrams of this system are shown in the appendix.

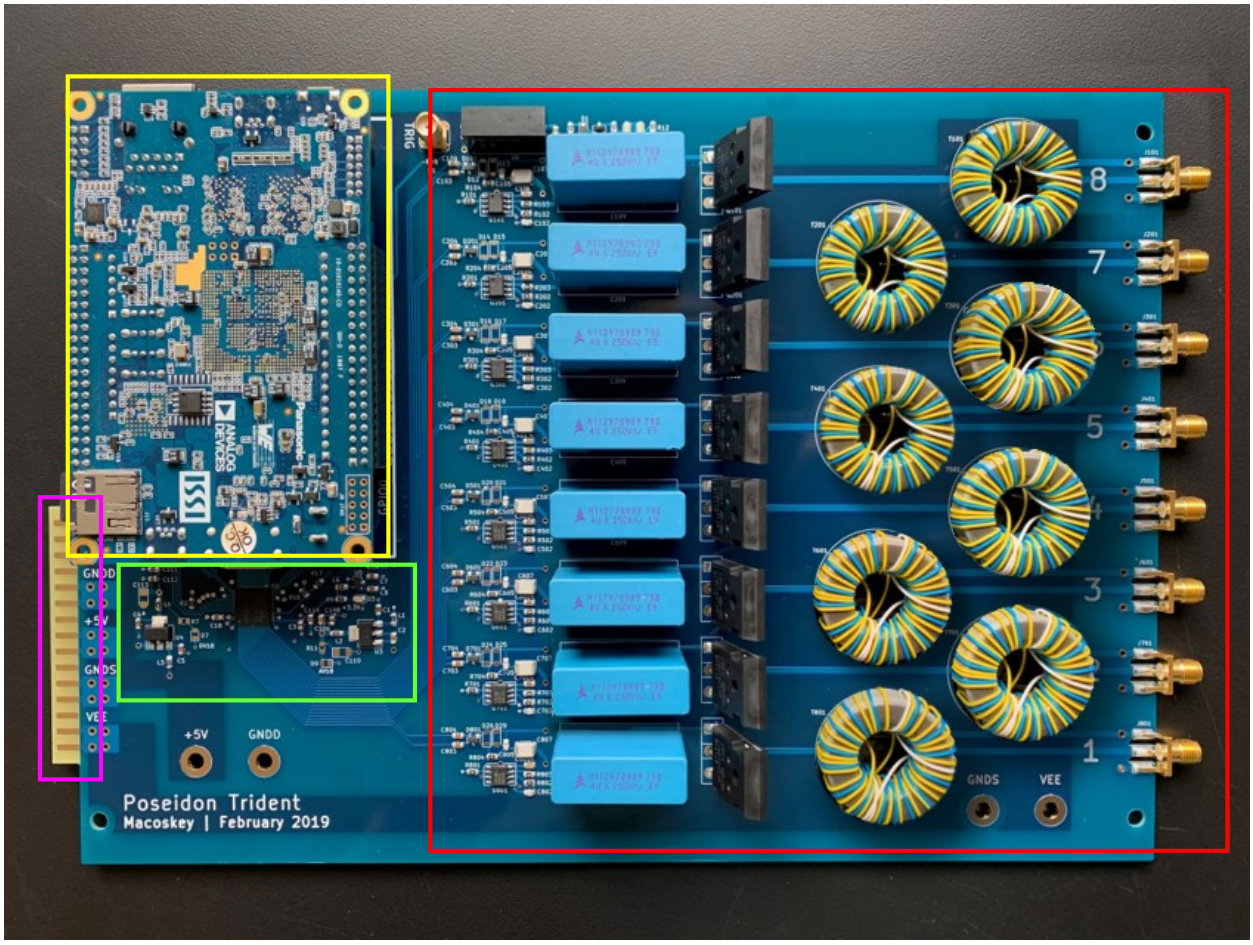

Figure 3.5: 8-Channel Poseidon board including analog transmit and receive electronics (red), FPGA/SoC module (yellow), ADC and supporting electronics (green), and card edge connector for backplane connection (pink).

3.3. Retrofit System

3.3.1 Materials and Methods

3.3.1.1 Analog Front-End Circuitry

To acquire acoustic information from the histotripsy array elements, the transmit line must be probed directly. However, the transmit waveform is on the order of 3 kV while the received waveforms are on the order of tens of Volts. Therefore, a nonlinear voltage compressor was

devised to compress the received voltages to a range that the sensitive receive electronics could handle. The passive components of this circuit were chosen and tested through a series of prototypes (Sections 3.2.1 - 3.2.3) prior to designing the Retrofit System. The fundamental components of this circuit are shown in Figure 3.6. The circuit consists of a capacitive voltage divider (C1 and C2), which attenuates all incoming signals from transducer element TX1 to approximately 10%. A capacitive divider was used (as opposed to a resistive one) because the aim was to attenuate an AC signal, and a capacitive divider is a much cheaper and smaller alternative to a transformer. Further, the use of a capacitive divider blocks any high voltage DC and can therefore be used to receive signals from a variety of high voltage driver designs. The second component is a diode-capacitor voltage divider (D1, D2, and C3) that provides nonlinear attenuation to compress signals above approximately 0.7 Volts and AC couples the signal into the ADC. The final component before the ADC is a voltage level shifter that puts the signal in the appropriate voltage range for the ADC (R2 and R3). The initial version of this circuit did not include resistor R1. However, upon further investigation, it was found that a voltage-dependent phase shift was induced without this resistor. This phase shift was induced by the recovery of the diodes when high voltages were applied. For applications where signal phase is important, such as

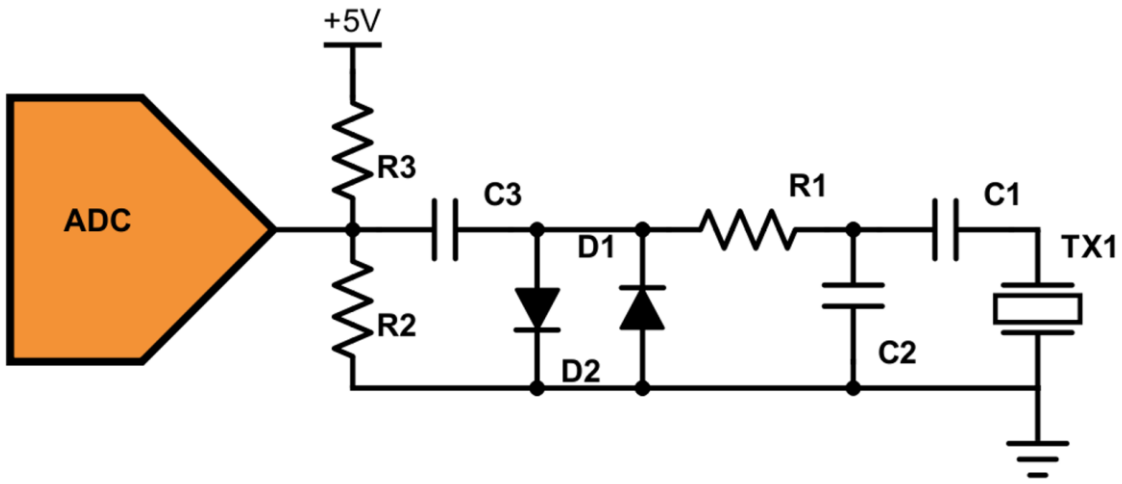

Figure 3.6: Retrofit System front-end analog circuit.

aberration correction, this phase shift is a detrimental flaw. However, with an appropriately valued resistor depending on the impedance of C1 and C2, this issue can be avoided.

3.3.1.2 Analog-to-Digital Conversion and Data Handling

The ADC chosen for this application was the ADC1175 (Texas Instruments, Dallas, TX, USA), which is a 20-MHz, 8-bit, one-channel ADC. This ADC was chosen due to its low cost, ease of use, and ease of installation. The part comes in the standard 24-TSSOP package and is therefore easily installable by hand, and costs less than $2.00, which is an insignificant cost per channel for histotripsy systems, which cost tens of thousands of dollars. The ADC1175 can be powered off 5V power and only consumes approximately 10 mA under maximum operation conditions, so the overall systemic impact of this component is small. The ADC1175 works by receiving an analog signal and converting it into an 8-bit signal which is output as eight parallel outputs. For this system, the eight digital outputs were connected to eight dedicated general-purpose input/output (GPIO) pins on an FPGA module (DE0-Nano SoC, Terasic, Inc., Hsinchu, Taiwan, China). This FPGA module consisted of an FPGA (Cyclone V SoC, Intel Corporation,

Santa Clara, CA, USA) and other requisite components such as memory and Ethernet hardware. Each FPGA module received data from eight channels, resulting in 64 parallel digital inputs.

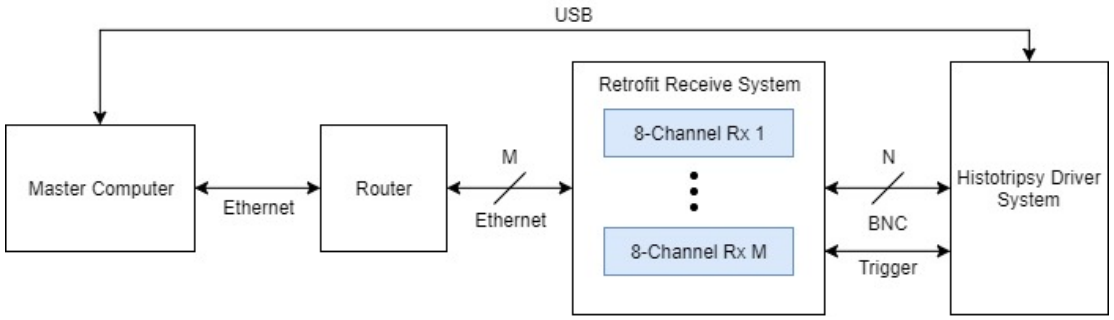

Figure 3.7: High-level system architecture for the retrofit histotripsy receiver system. White boxes indicate hardware modules, and blue boxes indicate hardware submodules. M equals the number of Ethernet connections between the receiver and the router, and N indicates the number of channels in the histotripsy system.

3.3.1.3 High-Level Architecture

The high-level system architecture for the retrofit system is shown in Figure 3.7. The design of this system allows for virtually any existing histotripsy system to be retrofitted with receive-capability. All N channels of a histotripsy driver are connected to both the receiver and their respective histotripsy element via build-in T-connectors on each channel of the 8-channel receiver boards. The DE0-Nano SoC FPGA boards receive 8-bit data from 8 separate channels, and then sends it via Ethernet to the Master Computer via an Ethernet switch (not shown) and a local area network router. For an N channel histotripsy system, there are M = ceil(N/8) Ethernet cables. The main computer controls both the transmit and receive capability of the overall system. However, the transmit and receive portions of retrofitted systems run separately. To synchronize the two systems, a trigger is output from the driver system to the receiver system so that the receiver system can record data at the appropriate time, i.e., at the same time after each histotripsy pulse when data acquisition is desired.

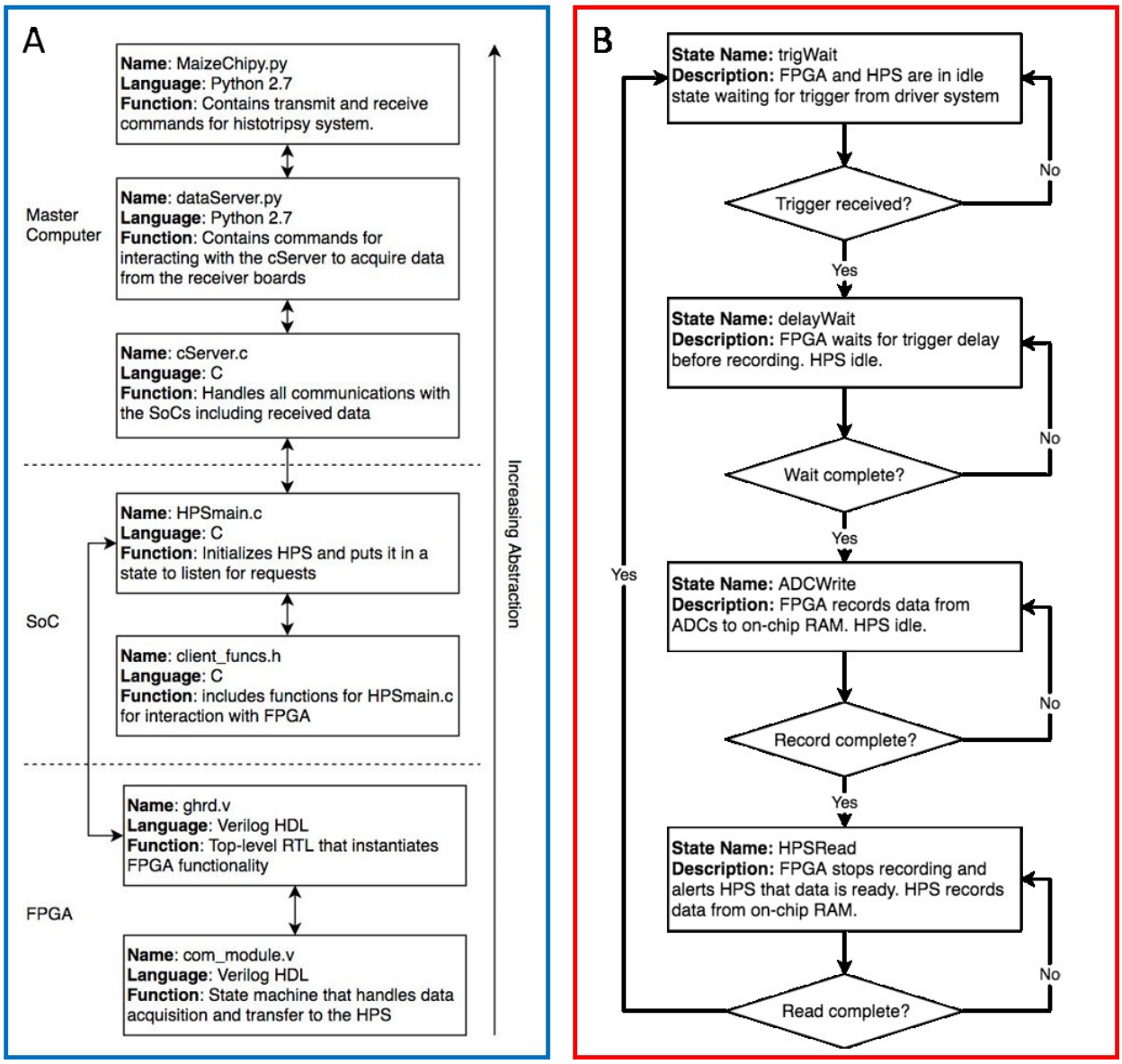

Figure 3.8: (A) Software flow and (B) state flow diagrams for the retrofit histotripsy receiver system.

3.3.1.4 Software

All FPGA software for this system was written in Verilog HDL, and all SoC and Master Computer software was written in C and Python. A software block diagram is shown in Figure 3.8A and a system state flow diagram is shown in Figure 3.8B. The software is divided into three systems with increasing levels of abstraction: the FPGA, SoC, and Master Computer levels. The

FPGA software consists of a communications module (com_module.v), which handles the FPGA state machine as well as the data acquisition directly off the ADCs from the GPIO pins connected to the FPGA. The top level (ghrd.v) is based on the Golden Hardware Reference Design from Intel, and instantiates all FPGA sub-modules including the communications module, the SoC communications module (not shown) and various PLL and RAM modules (not shown). The SoC communications modules simply activates existing dedicated data transfer channels between the HPS and FPGA sides of the Cyclone V SoC chip and sets up appropriate addresses. The SoC software consists of the main HPS program (HPSmain.c) and a header file that includes various functions used by the HPS (client_funcs.h). The main HPS program directly communicates with the Master Computer through a server program (cServer.c) running on the Master Computer. This server program controls the socket programming of the system and scans the network for SoCs that wish to communicate with the Master. The two user-oriented software modules include the data server (dataServer.py) and the therapy control module (MaizeChipy.py). These two software modules allow the user to create a therapy plan which includes both transmit and receive and essentially ties the two asynchronous systems (i.e., the driver system and the receiver system) together.

To ensure the integrity of the receiver data acquisition for each desired pulse, a state machine, which runs on the FPGA, controls when each hardware module can perform certain operations (Figure 3.8B). At the beginning of treatment, all receiver modules enter an idle state called “trigWait.” In this state, the FPGA waits for the histotripsy driver to transmit a trigger to a dedicated GPIO pin. Once the trigger is received, the FPGA enters the “delayWait” state, and the HPS remains idle, waiting for data. At this time, the FPGA waits for a pre-determined amount of time before recording data from the ADCs. The duration of this wait is programmed by the user

when planning the treatment. Once the wait is complete, the FPGA enters the "ADCWrite" state. In this state, the HPS remains idle while the FPGA records data from all channels and stores this data in on-chip RAM. The recording is complete once the FPGA has recorded the desired amount of data that was set by the user in a similar fashion to how the user set the trigger wait time. Once the recording is complete, the FPGA enters the "HPSRead" state in which the FPGA alerts the HPS that there is data to be collected. The FPGA will remain in this state until the HPS alerts the FPGA that it has received all data. Once the HPS read is complete, the system then returns to the trigWait state and waits for the next trigger from the driver system

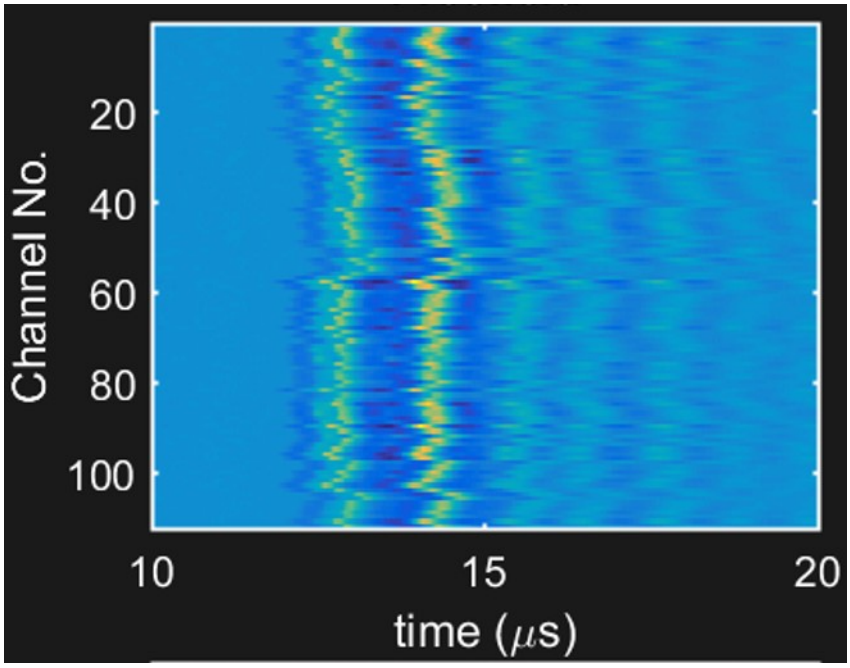

Figure 3.9: Example data from all 112 channels (y-axis) from one histotripsy pulse. These particular data are from the shockwave emitted by a bubble cloud that was received by all channels on the histotripsy array and was then used for aberration correction (see Chapter 5).

3.3.2 Results

The retrofit receive system was first implemented on a 112-channel, 500 kHz histotripsy system (Figure 3.4). This system consisted of 14 FPGA/SoC systems running in parallel. Based on the data limits of the system and Ethernet communications, the system was capable of recording

approximately 400 μs of data from all channels simultaneously with a 20 MHz sampling frequency at a 200 Hz histotripsy pulse repetition frequency (PRF). This results in a total data acquisition rate of approximately 184 MB per second. For a typical histotripsy treatment of 500 pulses at 1000 locations at 200 Hz PRF, this system would generate 450 GB of data in approximately 40 minutes. An example subset of data from all 112 channels from one pulse is shown in Figure 3.9.

3.3.3 Discussion

The retrofit system exhibited the ability to enable receive capability on any histotripsy system for the first time. Since the first implementation on the 112-channel, 500-kHz histotripsy array, this receiver design has been implemented on a 32-element spherical transducer designed for cavitation physics experiments and a 256-channel system designed for transcranial therapy.

While this system was successful, there are several improvements that should be made for the next version of this system, which is discussed in Section 3.4. First, the reason that this system was built as a retrofit rather than an entirely new histotripsy system with receive capability integrated with the transmit circuitry was that creating a brand new driving system is an expensive process relative to the electronics in this receiver system. While the retrofit style worked here, it resulted in two asynchronous systems running within the same therapy system. To synchronize these systems required a relatively substantial effort, and it results in a system that is relatively difficult to use and understand for the new user. The next version of this system should integrate transmit and receive capability into one system such that the FPGA/SoC modules control both processes for their respective channels. Second, the ADC used in this system was relatively low-quality in comparison to the ADCs used in modern ultrasound imaging equipment. While the maximum sample rate was a low 20 MHz, the bandwidth of the histotripsy receiver elements is

comparatively narrow- and low-band. Therefore, this is not an issue. The bit-depth, however, of the ADC1175 is quite low and rendered the desired dynamic range of the system a difficult standard to achieve. This issue was exacerbated by the fact that the front end analog circuit was not optimized for certain treatments. For example, treating through tissue resulted in reflections and acoustic emissions on the order of tens of Volts, which fit perfectly into the 256 available bit levels of the ADCs. However, for transcranial treatments, reflections off the skull can result in received signals of 100 V or more, which were nonlinearly compressed or clipped prior to the ADC. Using an ADC with appropriately tuned front-end protection circuitry in future systems with better bit resolution would allow for a higher dynamic range and more flexible systems. Lastly, retrofit the nature of this system resulted in nearly double the amount of cables on a typical transmit-only system. This problem would also be solved by integrating transmit and receive into one system.

3.4. An Integrated Transmit-and-Receive-Capable Histotripsy System: Poseidon

3.4.1 Materials and Methods

3.4.1.1 Analog Front-End Circuitry

The design of the driver electronics for this system had a direct impact on the design of the analog receiver circuitry and will therefore be briefly discussed first to orient the reader. A schematic overview of the high-voltage driver for one channel is shown in Figure 3.10. In this driver, bank of capacitors (not shown) in series with the primary coil of the transformer are charged by the high voltage supply. A driver chip, U1, then triggers the n-channel MOSFET transistor, Q1, which sends a high voltage AC pulse through the transformer primary coil thereby generating an AC pulse in the transformer secondary coil with a voltage proportional to the turn ratio between the coils. For this system, a turn ratio of approximately 1:3 was used between the primary and

secondary coils. Using this method, the high voltage driver is able to generate single-cycle pulses at the center frequency of the transducer on the order of 3 kV.

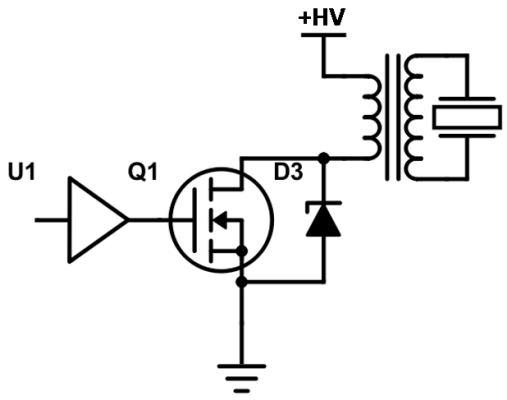

Figure 3.10: Schematic design of the high voltage driver used in the integrated receive-capable histotripsy system.

As shown in Figure 3.6, the retrofit system used a capacitive voltage divider to attenuate high voltage AC signals partly due to the fact that this is a cheap and compact alternative to using a step-down transformer. In comparison to previous histotripsy driving systems, the key difference with this system was that the transformer in Figure 3.10 was replaced with an inductor. Using a transformer offers two advantages. First, the driver is able to output several times more voltage simply due to the transformer winding ratio. Second, because the driver for this system already included a transformer at the output of each channel, a third coil could be added to each transformer

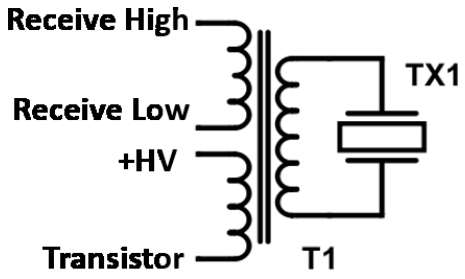

Figure 3.11: Schematic overview of the transformer design used in the integrated receive-capable histotripsy system.

and then be used for the receive electronics thereby providing total isolation between the driver and receiver, as shown in Figure 3.11. For this system, the tertiary coil was wound with approximately 10-times fewer windings than the secondary coil, thereby providing a 10X reduction in voltage. The schematic design of the receive circuitry for the integrated receive-capable histotripsy system is shown in Figure 3.12. Besides the change in ADC and the addition of the transformer, the analog receiver very closely resembles that of the retrofit system (Figure 3.6). Importantly, due to the addition of the step-down transformer, the divider ratio of the capacitive voltage divider formed by C1 and C2 was increased to only a 50% reduction in voltage. The diode divider and accompanying phase-shift-preventing resistor used in this circuit is identical to that used in the retrofit system. The analog circuit is then AC coupled to the analog front-end (AFE) using two 0.1-μF capacitors (C3 and C4).

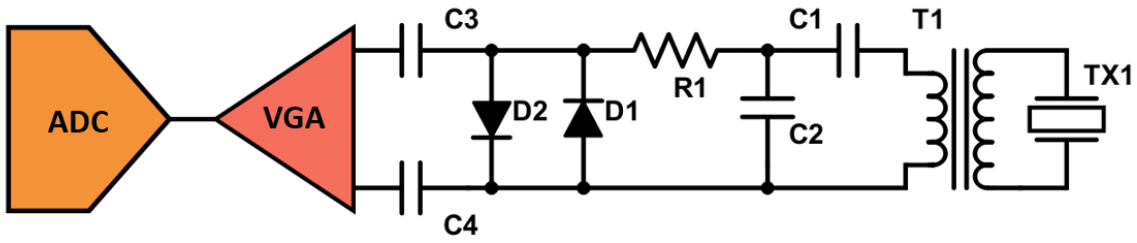

Figure 3.12: Schematic over of the receive circuitry for the integrated receive-capable histotripsy system including the analog front-end.

3.4.1.2 Analog-to-Digital Conversion and Data Handling

The AFE chosen for this application was the AFE5801 (Texas Instruments, Inc., Dallas, TX, USA), which includes an 8-channel, programmable variable gain amplifier (VGA), and an 8-channel, 12-bit, 65 MHz (maximum sampling rate) ADC. This ADC comes in the standard QFN-64 package and is therefore easily soldered by hand in a similar fashion to the ADC1175. This

system was designed that an FGPA/SoC module (DE10-Nano SoC, Terasic, Inc., Hsinchu, Taiwan, China) controlled both the transmit and receive of 8 histotripsy channels. However, controlling the output triggers of 8 histotripsy channels in addition to 96 parallel would be impossible for this platform due to a limited number of GPIO pins. The AFE5801 was therefore also chosen because the digital outputs for each channel were transmitted to the FPGA via the low-voltage differential signaling (LVDS) standard. This resulted in merely 16 GPIOs of the FPGA being consumed by the ADC. Conversion of the LVDS data was done in real-time on the FPGA

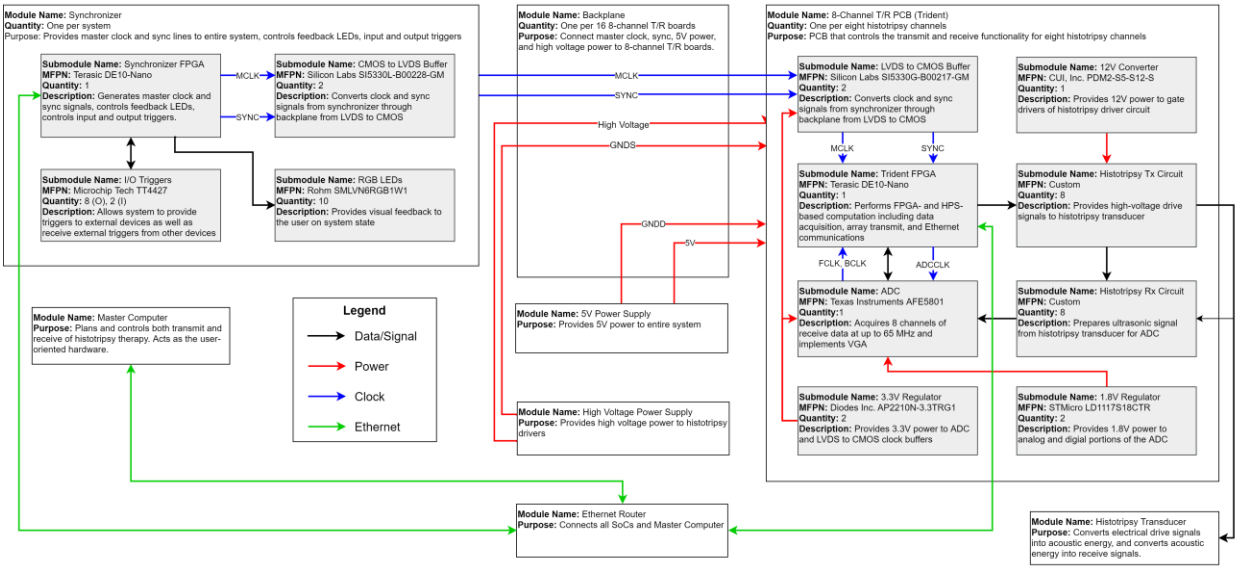

Figure 3.13: Hardware block diagram for the integrated receive-capable histotripsy system. White boxes indicate hardware modules, e.g., a circuit board, and gray boxes indicated important hardware submodules, e.g., the AFE5801.

before sending data to the HPS. Once the LVDS receive data was received and converted by the FPGA, it was sent to the HPS and handled identically to the methods used in the retrofit system for transmitting data back to the master computer.

3.4.1.3 High-Level Architecture

The hardware block diagram for the integrated receive-capable histotripsy system is shown in Figure 3.13 and is also shown in a larger format in the appendix. The system consists of three circuit boards: the synchronizer, backplane, and the 8-channel T/R circuit board (codename: Trident). For any given histotripsy system using this architecture, there is one trident board per eight transducer channels, one backplane per 16 trident boards, and only one synchronizer. The synchronizer is currently designed to be able to support up to four backplanes, or 512 histotripsy channels.

The synchronizer is used to, as its name would suggest, synchronize the entire system. The primary function of the synchronizer is to generate the master clock and sync signals that are fanned out to the entire system. The synchronizer includes a DE10-Nano SoC that is connected to the master computer via Ethernet. During treatment, the synchronizer generates a 10 MHz clock signal that is used as the master clock. The CMOS 10 MHz clock output from one GPIO pin on the DE10-Nano is connected to a 1:4 clock buffer (SI5330L-B00228-GM, Silicon Laboratories, Inc., Austin, TX, USA), which uses the LVDS standard for the clock outputs. The LVDS standard was chosen as the communications protocol for both the master clock and sync to reduce the risk of introducing an irreparable amount of noise to these signals while traversing cables, backplanes, and card edge connectors. Each clock output is routed to an SMA connector, which is used to coaxially connect the clock signals to a backplane. Due to the 1:4 output ratio of this clock buffer, only four backplanes are currently supported. However, one could easily design a different synchronizer board with a higher ratio clock buffer or several identical clock buffers to support larger systems. The distribution of the sync signal is performed identically to the master clock. The

synchronizer board also contains 10 RGB LEDs that are used to visually indicate various states of operation to the user, e.g., initialization, therapy active, error, etc.

The backplane is a passive circuit board that is used to connect the master clock and sync signals, the high voltage and its ground, and the 5V power and its ground to the trident T/R boards. There is one SMA port each for the master clock and sync lines per backplane. Importantly, a 100-Ohm terminating resistor for the LVDS clock and sync lines is included on the backplane as per the multidrop-LVDS standard (TIA/EIA-899) utilized to connect each of the 16 trident boards to the same clock and sync lines. The backplane also includes LEDs to indicate when the 5V and high voltage power are active.

The trident circuit board handles all transmit and receive functionality of the histotripsy transducer. A DE10-Nano is used to control both transmit and receive for subsets of 8 channels. Each trident board includes separate power regulators for the various components, which are all powered from the 5V supply. The LVDS master clock and sync lines are converted back to CMOS using a 1:8 ratio clock buffer (SI5330G-B00217-GM, Silicon Laboratories, Inc., Austin, TX, USA). Only one of the outputs of each clock buffer is connected to the FPGA via the GPIO headers on the DE10-Nano.

3.4.1.4 Software

The software hierarchy of the Poseidon integrated receive-capable histotripsy system is detailed in the software block diagram in Figure 3.14 and is shown in a larger format in the Appendix. Other than the fact that the Poseidon software now contains transmit capability, the overall architecture shares many similarities with the retrofit software (Figure 3.8). All FPGA software was written in Verilog HDL, all SoC software in C, and the top-level Master Computer

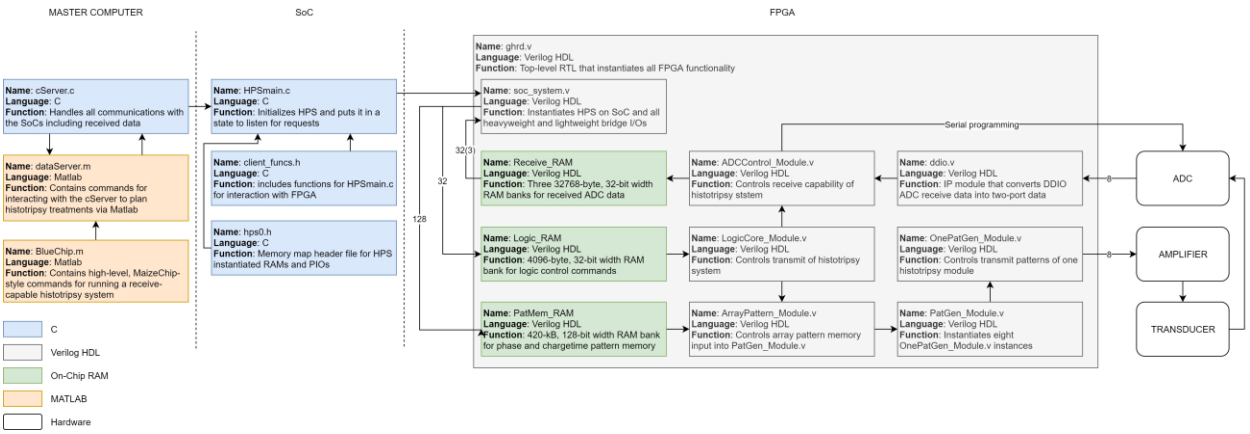

Figure 3.14: Software block diagram for integrated receive-capable histotripsy system. Software architecture allows for system programmability at several layers of abstraction including the Python architecture used in the retrofit system as well as a new Matlab high-level user interface.

software written in C with UI software modules written in Python and a new version written in Matlab.

The FPGA control software includes a golden-hardware reference design top level Verilog file (ghrd.v), which instantiates all lower-level FPGA software modules including the ADC control module, the Logic Core, and the Array Pattern modules. The ADCControl_Module.v file works virtually identically to com_module.v in the retrofit system. The major difference now is that ADCControl_Module.v no longer waits for an external trigger from a separate driver system. Instead, all state changes are internally controlled and data acquisition occurs synchronously with the driving portion of the system. Furthremore, the ADC control module also controls the serial programming of the ADC which includes modifying the gain an TGC profile. There is, however, still a state machine that handles when the FPGA receives data and when the HPS acquires this data from the FPGA, and there is no continuous acquisition option where the ADC continuously records throughout treatment despite the presence of a histotripsy pulse. This would result in an astronomically large and unnecessary amount of data. To protect users from accidentally acquiring

too much data and crashing the system, a maximum record time of 400 us is still maintained at a high level on the master computer.

For transmit, the Logic Core controls the state of the therapy. This core works in a similar manner to the Instruction Memory Module of the previous MaizeChip systems, and the ArrayPattern_Module.v, PatGen_Module.v, and OnePatGen_Module.v files remained virtually untouched from MaizeChip other than the necessary changes for channel numbers per driving board. However, the major change between this system and previous systems is the addition of large on-chip RAMs, which are shown in green in Figure 3.14. These RAMs are used for both transmit and receive and are enabled by the presence of the HPS interface. These RAMs operate on the heavyweight bridge instantiated by the QSYS software in the Intel Quartus Prime development suite and essentially act as DMAs that are accessible by both the FPGA and HPS. To write any given treatment plan to the FPGA, the HPS writes the entire 32-bit program into the RAM before treatment, which eliminates the need for the FPGA to serially receive and store individual instructions. This also significantly increases the number of treatment points from roughly 1000 locations on previous systems to over 27,000 locations on this system.

On the SoC, the hps0.h header file is used to map the memory locations of the various on-chip RAMs and is automatically generated by Quartus, and the client_funcs.h header file is used to define the various therapy functions, e.g., fire, receive, wait, etc. Together, these files allow the master computer to write individual treatment commands directly to the FPGA-level on-chip RAMs on every board in the system.

Other than the addition of new protocols for transferring therapy planning information from the master computer to the FPGA, the HPS software on the SoC has remained untouched for the most part from the retrofit system. Because of this, the general functionality of cServer.c is also

vastly unchanged other than the addition of functions necessary for treatment. Additionally, the previous version of cServer.c used on the retrofit system was only usable on a Linux-based master computer. Due to the fact that the majority of lab computers run Windows OS and many supporting software packages (e.g., high-speed camera software) are only available for Windows-based computers, a new version of cServer.c that can be run from the Windows OS has been created.

From a top-level point of view, the major changes are from the user-oriented side. While cServer.c functions virtually identically, a new Matlab Interface has been included in this distribution. The MIF includes a dataServer.m, which functions similarly to dataServer.py, and a new set of functions contained in BlueChip.m. The reason for doing this was that the previous version of histotripsy controller software that was built for transmit-only systems, called MaizeChip, is built in Matlab at high level. Therefore, the vast majority of histotripsy users are most familiar with a Matlab-based interface, so we wanted to ensure that the typical histotripsy researcher would be able to operate this system without first having to obtain a computer engineering degree.

An example Matlab script for running Poseidon with the BlueChip MIF is shown in Figure 3.15. One familiar with the program style of previous transmit-only systems will immediately feel at home. The major stylistic changes come from the fact that all commands are now stored in a class that is now instantiated by calling the `blueInit()` function. This function initializes communications with the Poseidon system. The user then stops any execution before moving on to setting up the transmit program. Performing the set up for transmit charge times and phases is identical to the way it was with the previous MaizeChip systems. Next, the user initializes the

```
% Initialize BlueChip System
d = blueInit();                         % Initialize BlueChip communcations
d.stop_execution;                       % stop any program that might be running

% set up TX program:
%*********************
ct = 500*ones(1,32);                    % 5 usec charge time for all channels
d.set_chipmem_wloc(25)                  % specify location for charge data
d.write_array_pattern_16bit(ct)         % write charge time to memory
%*********************

% set up RX program:
%*********************
d.setRecLen(400e-6)                     % set receive record length (max 400 usec)
d.toggleReceive(1)                      % initializes receive system
%*********************

% here is the actual program:
%*********************
d.set_imem_wloc(0)                      % start at instruction memory location 0
d.loadincr_chipmem(1,25)                % data memory location 25
d.set_amp(0)                            % set charge times
d.set_phase(0)                          % also set delay
d.start_loop(1,5000)                    % fire the output 5000 times
    d.fire(0)                           % fire output
    d.waitsec(100e-6)                   % pause 100 usec
    d.receive(0)                        % trigger receive system
    d.waitsec(10e-3-100e-6)             % pause 10 msec -> 100 Hz
d.end_loop(1)                           % end loop
d.halt                                  % stop at end of loop
%*******************

d.execute_program(0)                    % run program
```

Figure 3.15: Example program for running the BlueChip system in Matlab with receive on every pulse.

receive system. First, the user selects the amount data they wish to collect after each pulse up to 400 µs. For the BlueChip system, the ADCs are hard-coded to run at a 25 MHz sampling frequency. Doing so reduces the chances of fatal software errors, and 25 MHz is more than substantial for any histotripsy experiments given that the majority of histotripsy transducers do not have a bandwidth that extends above 1 MHz. Next, the user calls the `toggleReceive()` command to initialize the receive system. This command forces the FPGA into a state in which it programs the ADCs functionality through the serial interface. Once it is done (which takes on the

order of 10s of microseconds), it alerts the HPS that the ADC is initialized. From this point in the program forward, the functionality is identical to that in the previous MaizeChip system. The only difference is that the user must call the `receive()` function (an argument of 0 is default and optional) to receive data after a pulse. This gives the user the flexibility to decide whether or not receive data is acquired after any given pulse. In this example, the treatment plan has the transducer fire a pulse 5000 times at a 100 Hz PRF. At 100 μs after the transducer is fired (programmed via `d.waitsec(100e-6)`), the receive system is triggered and acquires data for 400 μs. The system then waits another 9.9 ms until the next pulse to ensure a treatment PRF of 100 Hz.

3.4.1.5 Mechanical System Design

The first two systems built using this architecture were built to drive a 260-channel abdominal transducer and 360-channel transcranial transducer. Therefore, each system required three backplanes, so the mechanical design for both was identical. Both systems were rack-mounted in off the shelf 25U server racks (SR4POST25, Tripp Lite, Chicago, IL, USA) mounted on caster wheels for easy movability. Each backplane required 5U of rack space but only approximately 12-inches of depth. Therefore, the driver outputs were mounted on the back side of the rack, taking up 15U of the rack, while the user-oriented components were mounted on the front of the rack. The user-oriented components included the synchronizer (5U), high-voltage power amplifier (1U), computer (4U), and 5V power switch (mounted with synchronizer). The overall design of these systems allowed for simply portability and usability by hiding all unnecessarily complicated electronics within the rack and porting all transducer cables out the back side while providing a comfortable, convenient physical user interface on the front side. While the overall

design was complete at the time of this dissertation, the parts required for assembly were not yet available and so no image of either system is yet available.

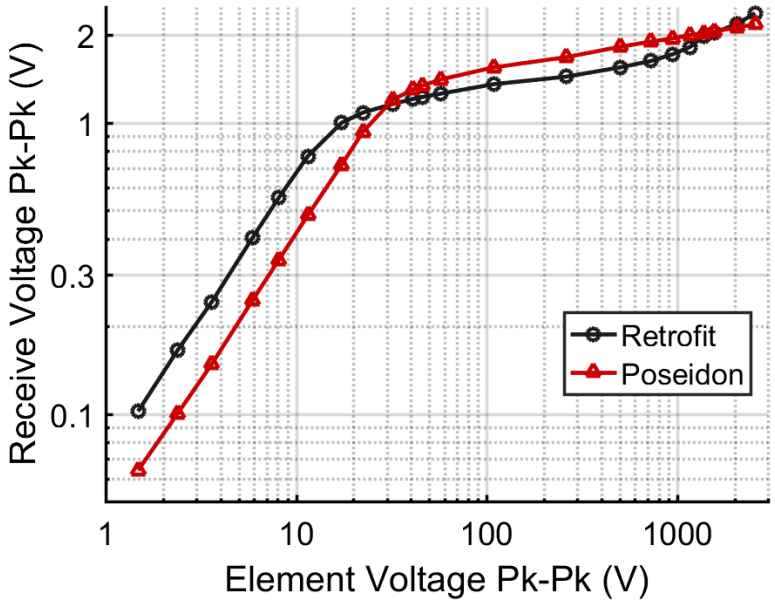

Figure 3.16: Transfer functions for the Retrofit (black) and Poseidon (red) systems. The x-axis indicates the peak-to-peak voltage measured at the element, and the y-axis indicates the peak-to-peak voltage measured just before the ADC for both systems.

3.4.2 Results

The transfer functions for both the Retrofit system and the Integrated (Poseidon) system are shown in Figure 3.16. The Poseidon system exhibited better linearity in both the low voltage (<30 V) and high voltage regimes. In the low voltage regime, the Retrofit system exhibited a range of approximately 0.7 V while the Poseidon system exhibited a range over 1 V, which means that there is less nonlinear compression for smaller signals. In the high voltage regime, the Retrofit system exhibited a nonlinear transfer function that appeared to begin linear growth at higher voltage levels while the Poseidon system exhibited nearly perfect logarithmic growth towards a threshold around 2 V peak-to-peak. The improved linearity of the Poseidon system results in more

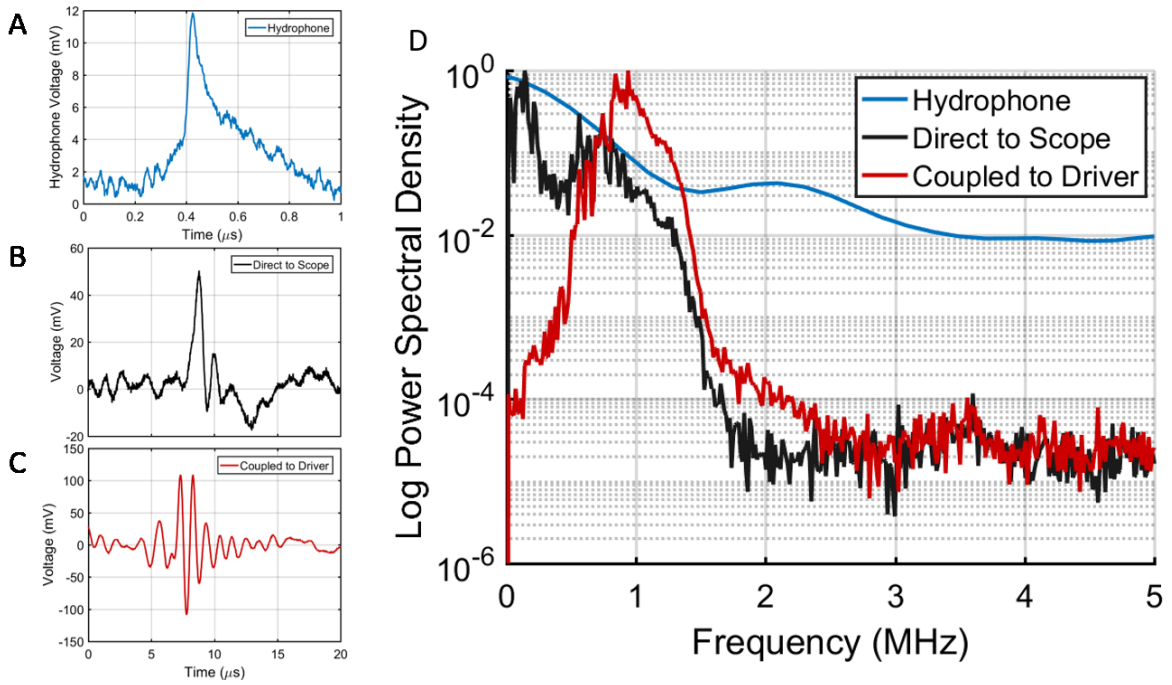

Figure 3.17: Single-bubble shockwaves recorded on a (A) broadband hydrophone, (B) passive histotripsy element not connected to a driving system, and (C) histotripsy element connected to the Poseidon driving system. (D) Power spectra of the signals shown in (A), (B), and (C).

predictable input-output characteristics and an improved dynamic range over the Retrofit system, which will be discussed in detail later in this section.

The bandwidth of the Poseidon system was analyzed by acquiring a single-cycle shockwave emitted by a single histotripsy cavitation bubble (Figure 3.17). When acquired by a broadband hydrophone, these single-cycle shockwaves appear as a broadband impulse with a rise time on the order of tens of nanoseconds, as shown in Figure 3.17A. However, when acquired on a passive histotripsy element that is not connected to a histotripsy driver, the rise time of the impulse is reduced significantly, as shown in Figure 3.17B. However, the overall impulse shape is still observable, and the arrival time of the highest pressure portion of the shockwave is easily observable. When connected to a histotripsy driver, the impulse response of a histotripsy element becomes narrowband and a significant amount of ringing is introduced, as shown in Figure 3.17C. The power spectra of these three signals is shown in Figure 3.17D. As expected, the hydrophone

shockwave signal exhibits a broadband frequency response while the histotripsy elements (both connected and not connected to the driver) exhibit a narrowband frequency response due to the fact that they are large piezoelectric disks with a specific resonant frequency. However, the driver-connected element exhibits a significantly more narrowband frequency response with around 10% bandwidth or less while the passive element exhibited a bandwidth around 30-50%. This reduction in bandwidth is due to the large inductance of the secondary coil of the transformer, which drives the frequency response to its resonant frequency. This same issue existed in previous systems where an inductor was used instead of a transformer. This reduction in bandwidth makes it more difficult to determine the precise arrival time of shockwaves, which is important for both treatment monitoring and aberration correction.

Given the shockwave waveform in Figure 3.17C, which has a peak to peak amplitude of approximately 200 mV, the received waveforms that would be acquired by the ADCs of both the Retrofit and Poseidon systems would have voltage levels of approximately 165 mV and 100 mV according to the transfer functions shown in Figure 3.16. Given that the ADCs are able to acquire signals across a voltage range of approximately 2 V peak-to-peak, we can estimate the quantization and therefore the dynamic range of each system. The ADC on the Retrofit system acquired signals at 8-bit while the Poseidon system acquires signals at 12-bit. This means that, across the 2 V range, the Retrofit ADC quantizes signals to approximately 9.3 mV levels while the Poseidon ADC quantizes to 0.53 mV levels. Given the 165 mV and 100 mV shockwave waveforms on the Retrofit and Poseidon systems, respectively, each system would quantize the shockwave signal in Figure 3.17C into 18 levels and 189 levels, respectively. A simulation of this quantization is shown in Figure 3.18. Qualitatively, the shockwave acquired by the Retrofit system is clearly quantized to some of the lowest possible sensitivity levels of the system while the Poseidon-acquired

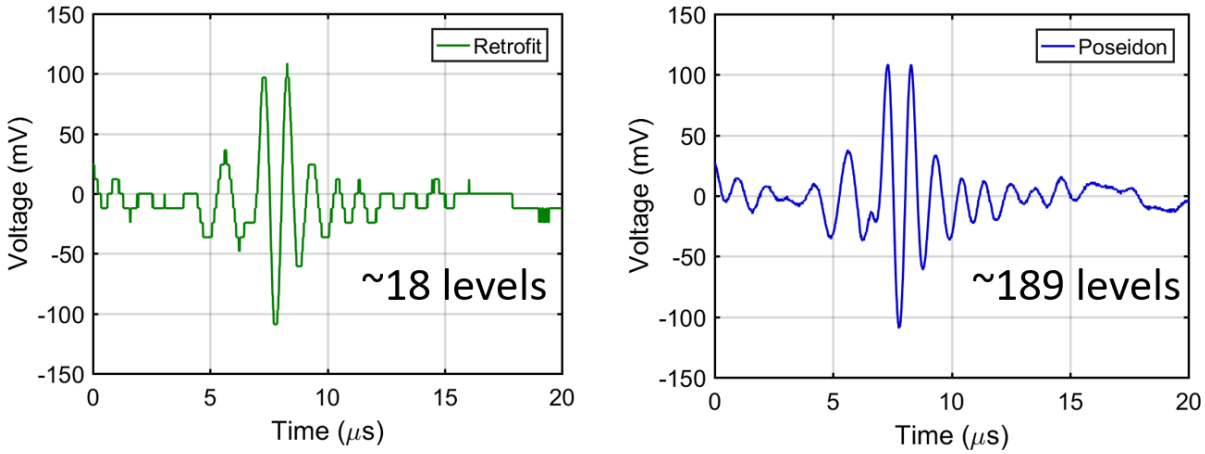

Figure 3.18: Simulation of ADC quantization for a single-cycle shockwave received by the Retrofit receiver system (left) and the integrated Poseidon receiver system (right).

shockwave looks virtually identical to the analog signal. This results in the ability for better signal processing and quantitative assessment of ACE signals. Given that $Dynamic\ Range = 20 \times \log_{10}(Vmax/Vmin)$, where $Vmax$ and $Vmin$ are the maximum and minimum respective possible signal levels that each system can acquire, we can estimate that the Retrofit system has a 48 dB dynamic range while the Poseidon system has a 72 dB dynamic range. This means that the Poseidon system has a dynamic range that is nearly 16-times better than the Retrofit system.

3.4.3 Discussion

In this chapter, we developed and tested the first receive-capable histotripsy systems. A multitude of prototypes were developed to test various aspects of receive-based histotripsy prior to a full-scale implementation. The work in this chapter began with early-stage analog receiver prototypes and concluded with the disclosure of the design of a fully-integrated receive-capable histotripsy system. The Poseidon system and BlueChip software architecture allow for seamless integration of receive capability into existing histotripsy workflows. The current design allows for up to 512 histotripsy channels to be driven simultaneously, all with receive capability at 25 MHz

sampling with up to 400 μs of acquired data per pulse. However, by designing a different synchronizer board with more than one clock and sync buffer chip, a system with thousands of channels could easily be devised. Further testing of these systems is awaiting the fabrication of their accompanying transducers. However, the full functionality of this hardware and software architecture is complete.

Several improvements can still be made to the state-of-the-art system in this chapter, which will be discussed in greater detail in Chapter 6 but highlighted upon here. First, the reliance on using off-the-shelf FPGA platforms results in a significant loss of flexibility. FPGAs are inherently flexible devices with typically hundreds of I/Os and dozens of LVDS pairs allowing for a massive amount of data throughput. However, the DE0-Nano and DE10-Nano boards reduce this functionality by dedicating many of the I/Os to peripheral hardware on their respective boards that are not used at all for these histotripsy systems, e.g., HDMI or audio output. While the engineering effort required to design a custom PCB will all the necessary supporting hardware to support modern FPGAs such as the Cyclone V SoC would be significant, the efforts could pay off substantially and may result in systems that have many more than eight channels controlled by a single FPGA. This would result in lighter-weight, faster, and cheaper histotripsy systems.

A second major possible improvement to these systems would be to improve the bandwidth of the receiver portion of the system. Due to the inductive load of the driver caused by the transformer, frequencies outside the driver frequency band are significantly attenuated to the point that they are virtually undetectable. Meanwhile, the histotripsy elements themselves are relatively narrowband and act as excellent passive receivers. While the ADC and analog front-end circuitry is also capable of capturing information well outside the driver frequency band, none of it is captured due to this flaw. Therefore, either higher bandwidth driving systems or receive systems

that are able to completely isolate the transducer and receive circuit from the driver (e.g., with a T/R switch) would drastically improve performance. This would be especially impactful for improved functionality in areas such as aberration correction where the acquisition of broadband shockwaves is desired.

3.5. Summary

This chapter detailed the first receive-based histotripsy systems and discussed, in detail, the technical challenges associated with doing so. Using the information in this chapter, it is our hope that other histotripsy researchers as well as therapeutic ultrasound researchers in general may be able to develop receive-enabled therapeutic ultrasound systems to further the field of noninvasive ultrasonic surgery.

3.6. References

[1] J. Macoskey, X. Zhang, T. Hall, J. Shi, S. Beig, E. Johnsen, F. Lee Jr., C. Cain and Z. Xu, "Bubble-Induced Color Doppler Feedback Correlates with Histotripsy-Induced Destruction of Structural Components in Liver Tissue," *Ultrasound in Med. & Biol.,* vol. 44, no. 3, pp. 602-12, 2018a.

[2] A. Casper, D. Lui, J. Ballard and E. Ebbini, "Real-Time Implementation of Dual-Mode Ultrasound Array System: In Vivo Results," *IEEE Trans. Biomed. Eng.,* vol. 60, no. 10, pp. 2751-59, 2013.

[3] H. Yao and E. Ebbini, "Dual-mode ultrasound phased arrays for imaging and therapy," in *2nd IEEE International Symposium on Biomedical Imaging: Nano to Macro*, Arlington, VA, USA, 2004.

[4] J. Ballard, A. Casper, Y. Wan and E. Ebbini, "Adaptive Transthoracic Refocusing of Dual-Mode Ultrasound Arrays," *IEEE Trans. Biomed. Eng.,* vol. 57, no. 1, pp. 93-102, 2009.

[5] F. Marquet, J. Aubry, M. Pernot, M. Fink and M. Tanter, "Optimal transcostal high-intensity focused ultrasound with combined real-time 3D movement tracking and correction," *Phys. Med. Biol.,* vol. 56, pp. 7061-80, 2011.

[6] H.-L. Lui, C.-H. Tsai, C.-K. Jan, H.-Y. Chang, S.-M. Huang, M.-L. Li, W. Qui and H. Zheng, "Design and Implementation of a Transmit/Receive Ultrasound Phased Array for Brain Applications," *IEEE Trans. Ultrason. Ferroelectr. Freq. Control,* vol. 65, no. 10, pp. 1756-67, 2018.

[7] K.-W. Lin, Y. Kim, A. D. Maxwell, T.-Y. Wang, T. L. Hall, Z. Xu, B. J. Fowlkes and C. A. Cain, "Histotripsy beyond the intrinsic cavitation threshold using very short ultrasound

pulses: Microtripsy," *IEEE Trans. Ultrason., Ferroelect., Freq. Control,* vol. 61, no. 2, pp. 251-265, February 2014.

[8] Z. Xu, T. Hall, J. B. Fowlkes and C. A. Cain, "Effects of acoustic parameters on bubble cloud dynamics in ultrasound tissue erosion (histotripsy)," *J. Acoust. Soc. Am.,* vol. 122, no. 1, pp. 229-236, July 2007.

[9] Z. Xu, A. Ludomirsky, L. Y. Eun, T. L. Hall, B. C. Tran, B. J. Fowlkes and C. A. Cain, "Controlled Ultrasound Tissue Erosion," *IEEE Trans. Ultrason., Ferroelect., Freq. Control,* vol. 51, no. 6, pp. 726-736, June 2004.

[10] J. Macoskey, S. Choi, T. Hall, E. Vlaisavljevich, J. Lundt, E. Johnsen, C. Cain and Z. Xu, "Using the cavitation collapse time to indicate the extent of histotripsy-induced tissue fractionation," *Phys. Med. Biol.,* vol. 63, p. 155013, 2018.

[11] J. Macoskey, T. Hall, J. Sukovich, S. Choi, K. Ives, E. Johnsen, C. Cain and Z. Xu, "Soft-Tissue Aberration Correction for Histotripsy," *IEEE Transactions on Ultrasonics, Ferroelectrics, and Frequency Control,* vol. 65, no. 11, pp. 2073-85, 2018.

[12] T. Leighton, "The Forced Bubble," in *The Acoustic Bubble*, San Diego, Academic Press, Inc., 1994, pp. 287-438.

[13] T. Whittingham, F. Duck, Baker and S. H. AC, "The Purpose and Techniques of Acoustic Output Measurement," in *Ultrasound in Medicine*, Philadelphia, Institute of Physics Publishing, 1998, pp. 129-148.

[14] M. Gyöngy, M. Arora, J. A. Noble and C. C. Coussios, "Use of Passive Arrays for Characterization and Mapping of Cavitation Activity during HIFU Exposure," Beijing, 2008.

[15] M. Plesset, "Shockwaves from cavity collapse," *Phil. Trans. Royal Soc. A,* vol. 260, no. 1110, pp. 241-244, 1966.

[16] M. Plesset and A. Prosperetti, "Bubbly Dynamics and Cavitation," *Ann. Rev. Fluid Mech.,* vol. 9, pp. 145-185, 1977.

[17] C. Coussios, C. Farny, G. Ter Haar and R. Roy, "Role of acoustic cavitation in the delivery and monitoring of cancer treatment by high-intensity focused ultrasound (HIFU)," *International Journal of Hyperthermia,* vol. 23, no. 2, pp. 105-120, 2007.

[18] V. Salgaonkar, S. Datta, C. Holland and T. Mast, "Passive cavitation imaging with ultrasound arrays," *J. Acoust. Soc. Am.,* vol. 126, no. 6, pp. 3071-83, 2009.

[19] J. Sukovich, T. Hall, J. Macoskey, C. Cain and Z. Xu, "Investigation of the source of histotripsy acoustic backscatter signals," *Journ. Acoust. Soc. Am.,* vol. 141, p. 3551, 2017.

[20] M. Burgess and T. Porter, "Control of acoustic cavitation for efficient sonoporation with phase-shift nanoemulsions," *Ultrasound Med. Biol.,* vol. 45, no. 3, pp. 846-58, 2019.

[21] J. Macoskey, J. Sukovich, T. Hall, C. Cain and Z. Xu, "Real-time acoustic-based feedback for histotripsy therapy," in *173rd Meeting of the Acoustical Society of America*, Boston, MA, 2017.

[22] G. Owens, R. Miller, G. Ensing, K. Ives, D. Gordon, A. Ludomirsky and Z. Xu, "Therapeutic ultrasound to noninvasively create intracardiac communications in an intact animal model," *Catheter. Cardiovasc. Interv.,* vol. 77, no. 4, pp. 580-8, 2011.

[23] G. Owens, R. Miller, S. Owens, S. Swanson, K. Ives, G. Ensing and D. X. Z. Gordon, "Intermediate-term effects of intracardiac communications created noninvasively by

therapeutic ultrasound (histotripsy) in a porcine model," *Pediatric cardiology,* vol. 33, no. 1, pp. 83-9, 2012.

[24] T. Hall, J. Fowlkes and C. Cain, "A real-time measure of cavitation induced tissue disruption by ultrasound imaging backscatter reduction," *IEEE Trans Ultrason Ferroelectr Freq Control,* vol. 54, no. 3, pp. 569-75, 2007.

[25] R. Miller, A. Maxwell, T.-Z. Wang, J. Fowlkes, C. Cain and Z. Xu, "Real-time elastography-based monitoring of histotripsy tissue fractionation using color Doppler," in *IEEE International Ultrasonics Symposium*, Dresden, Germany, 2012.

[26] T.-Z. Wang, T. Hall, Z. Xu, J. Fowlkes and C. Cain, "Imaging feedback of histotripsy treatments using ultrasound shear wave elastography," *IEEE Trans. Ultrason. Ferroelec. Freq. Control,* vol. 59, no. 6, pp. 1167-81, 2012.

[27] C. Cain and T.-Z. Wang, "Imaging feedback of histotripsy treatments with ultrasound transient elastography". United States Patent US 20130102932 A1, 10 Oct 2012.

[28] T.-Z. Wang, T. Hall, Z. Xu, J. Fowlkes and C. Cain, "Imaging feedback for histotripsy by characterizing dynamics of acoustic radiation force impulse (ARFI)-induced shear waves excited in a treated volume," *IEEE Trans. Ultrason. Ferroelec. Freq. Control,* vol. 61, no. 7, pp. 1137-51, 2014.

[29] R. Miller, Z. X, M. AD, C. CA and X. Z, "Bubble-Induced Color Doppler Feedback for Histotripsy Fractionation," *IEEE Trans Ultrason Ferroelectr Freq Control,* vol. 63, no. 3, pp. 408-19, 2016a.

[30] X. Zhang, R. M. Miller, K.-W. Lin, A. M. Levin, G. E. Owens, H. S. Gurm, C. A. Cain and Z. Xu, "Real-Time Feedback of Histotripsy Thrombolysis Using Bubble-Induced Color Doppler," *Ultrasound in Medicine & Biology,* vol. 41, no. 5, pp. 1389-1401, May 2015.

[31] Z. Xu, F. Zhenzhen, T. L. Hall, F. Winterroth, B. J. Fowlkes and C. A. Cain, "Size Measurement of Tissue Debris Particles Generated from Pulsed Ultrasound Cavitational Therapy - Histotripsy," *Ultrasound Med. Biol.,* vol. 35, no. 2, pp. 245-255, February 2009.

[32] Z. Xu, M. Raghavan, T. L. Hall, M.-A. Mycek, B. J. Fowlkes and C. A. Cain, "Evolution of Bubble Clouds Induced by Pulsed Cavitational Ultrasound Therapy - Histotripsy," *IEEE Trans. on Ultrasonics, Ferroelectrics, and Frequency Control,* vol. 55, no. 5, pp. 1122-1132, May 2008.

[33] Z. Xu, R. M. Miller, A. Maxwell and C. A. Cain, "Bubble-induced color doppler feedback during histotripsy". USA Patent US 20140100459 A1, 4 Oct 2013.

CHAPTER 4

Acoustic Cavitation Emission Monitoring for Histotripsy Feedback

The majority of this chapter has been published in *Physics in Medicine & Biology*. 2018; 63(055013):1-13.

4.1. Introduction

Histotripsy is a tissue ablation method that uses highly controlled acoustic cavitation to noninvasively destroy soft tissue using high peak rarefactional pressure amplitude (>28 MPa), short duration (1-2 cycles) ultrasonic pulses in the intrinsic threshold regime [2, 3, 4]. Histotripsy destroys tissue by repeatedly initiating a dense cloud of cavitation microbubbles, which coalesce and collapse violently, thereby fractionating tissue into acellular homogenate [5, 6]. Upon arrival of the acoustic pulse, existing cavitation nuclei in the treated medium are excited, resulting in a fast expansion of bubbles. These bubbles expand several orders of magnitude until they have reached a maximum radius, R_{max}, and then collapse in a violent fashion to microscopic size [7]. This sequence of energetic expansion and collapse is known as inertial cavitation [8], which is the fundamental physical mechanism through which histotripsy destroys tissue [9]. After a sufficient number of pulses, histotripsy can completely fractionate soft tissue into a liquefied acellular homogenate [10]. It is known that areas of the body with a higher Young's modulus (a quantitative indicator of stiffness) such as the wall of blood vessels or fibrous tissues, e.g., tendons, take higher doses of histotripsy pulses to completely liquefy [11, 12].

Previously, ultrasound elastography techniques, such as acoustic radiation force impulse (ARFI) imaging and shear wave imaging, have been used to monitor histotripsy-induced tissue

fractionation in real-time [13, 14, 15]. It has been found that ultrasound elastography is able to track tissue fractionation with higher sensitivity than by simply observing changes in the B-mode speckle intensity that are caused by the destruction of diffuse scatterers in the tissue [16, 17, 18]. In these studies, it was shown that the Young's modulus of soft tissues, such as kidney and liver, decreases throughout histotripsy treatment until a threshold is reached at which point the tissue has been completely liquefied [15].

Cavitation bubble dynamics models in viscoelastic media show that the cavitation bubble collapse time (t_{col}), i.e., the time between the initial expansion and first collapse of the bubble cloud, is expected to increase with decreasing Young's modulus. The Kelvin-Voigt model, given by **(**E4.1**)** [19, 20, 21]

$$\boldsymbol{\tau = \frac{2}{3}E\gamma + 2\mu\dot{\gamma}} \textbf{ (E4.1)},$$

is commonly used to describe viscoelastic media, which relates the stress tensor, τ, to the Young's modulus, E, the deformation tensor, γ, and the viscosity, μ. The stress tensor can be further related to the bubble radius, R, through the Keller-Miksis **(**E4.2**)**,

$$\boldsymbol{\left(1-\frac{\dot{R}}{c}\right)R\ddot{R}+\frac{3}{2}\left(1-\frac{\dot{R}}{3c}\right)\dot{R}^2=\frac{1}{\rho}\left(1+\frac{\dot{R}}{c}\frac{\mathrm{d}}{\mathrm{d}t}\right)\left(p_g-\frac{2S}{R}-p_\infty(t)-\frac{4E}{9}\left(1-\frac{R_0^3}{R^3}\right)-\frac{4\mu\dot{R}}{R}\right)} \textbf{ (E4.2)},$$

which is dependent upon the sound speed, c, and density, ρ, of the medium, the surface tension against air, S, the absolute forcing pressure $p_\infty(t)$, an assumed spatially uniform pressure within the gas bubble, p_g, and the initial radius of the bubble, R_0 [22]. From this equation, it can be seen

that the spatial and temporal dynamics of the bubble radius are directly dependent on the Young's modulus of the medium. Previous simulations and experiments have shown that as the stiffness of the medium quantified by the Young's modulus decreases, the bubble R_{max} and t_{col} both increase [23, 24, 25, 26].

We hypothesize that as target-tissue becomes further fractionated over the histotripsy treatment, the effective tissue stiffness decreases, and thus the t_{col} of the cavitation bubble cloud increases. It is known that both the initial expansion and collapse sequences result in the emission of measureable acoustic shockwaves [27, 28, 29, 30, 31, 32, 33]; thus, t_{col} can be measured directly by detecting these emitted shockwaves. We further hypothesize that the increase of t_{col} over the histotripsy treatment can be used to monitor the treatment progression and completion.

In this study, these hypotheses were tested in three steps. First, transparent agar gel phantoms of varying stiffness were treated with histotripsy at a single location. We acquired the acoustic shockwave signal emitted by the bubble cloud collapse using broadband hydrophones, and we recorded high-speed imaging of the cavitation to validate the hydrophone measurements. The t_{col} parameter was calculated from both signals to compare with each other. Second, the change of t_{col} over the treatment recorded acoustically was correlated with the lesion progression in the tissue-mimicking red blood cell (RBC) phantoms. Third, the increasing trend of t_{col} over the treatment was validated in *ex vivo* bovine liver. Lastly, preliminary results from an ongoing study using a receive-capable histotripsy array to monitor collapse time during treatment are discussed.

4.2. Materials and Methods

4.2.1 Histotripsy Transducer and Setup

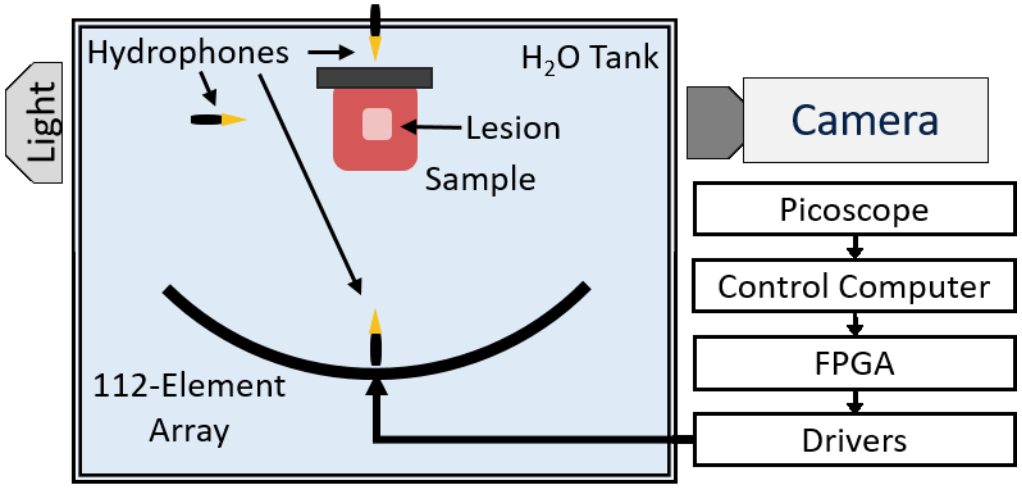

Figure 4.1: Experimental Setup. A 500 kHz 112-element high-powered ultrasound array is used to generate histotripsy lesions at a single location within tissue-mimicking phantoms and ex vivo bovine liver. Three hydrophones at varying positions are used to capture the acoustic shockwaves emitted by the cavitation bubble cloud, and their signals are acquired on a Picoscope data acquisition system (connections not shown). A high-speed camera is used to image the backlit bubble cloud during transparent tissue-mimicking phantom experiments.

A 500 kHz, 112-element histotripsy array constructed in-house with a 15 cm radius of curvature and a 27 cm aperture was used for all treatments in this study [34]. A custom-built 112-channel high-voltage pulser was used to drive each element with an approximately 1.5-cycle, 3-µs sinusoidal pulse. All elements were driven in-phase such that the histotripsy pulse from each element arrived at the geometric focus of the array simultaneously. A schematic overview of the setup is shown in Figure 4.1. The acoustic waveform generated at the focus was measured using a fiber-optic probe hydrophone (FOPH) with a 100-µm sensing tip [35]. The array produced a focal zone with a -6 dB beamwidth of 1.65 mm laterally and 6.50 mm axially when measured with the FOPH in the linear regime at a peak rarefactional pressure amplitude of 10 MPa. Above 10 MPa peak-negative pressure (P-), the acoustic waveform could not be measured directly because cavitation occurred at the FOPH tip. For P- greater than 10 MPa, the output from the transducer

was estimated by dividing the array into several subaperture slices, which were driven and measured separately and summed to estimate the pressure at each driving voltage. The number of subapertures chosen was always the minimum number required to prevent cavitation at the FOPH tip for each respective driver voltage level [34].

The histotripsy array was placed facing upwards in a water tank, and all samples were placed above the array at its focus (Figure 4.1). All treatments were applied at a single location at the geometric focus of the histotripsy array at 1-Hz pulse repetition frequency (PRF). This low PRF was chosen to reduce cavitation memory effects due to persistent residual nuclei, which are known to alter cavitation dynamics [36]. Agar samples were treated with 100 pulses, and liver samples were treated with 1000 pulses.

4.2.2 Hydrophone-Based Cavitation Detection

Three broadband hydrophones (Model CA-1135, Dynasen, Inc., Goleta, CA) were placed in the tank at three different orientations: above, to the side, and directly below the focus of the array all at different distances from the focus of the histotripsy array (Figure 4.1). This was done to investigate any differences in t_{col} when measured from different orientations relative to the sample and to ensure that we were obtaining the signal from the cavitation collapse and not from scattering. Each hydrophone was connected to a multi-channel oscilloscope (Picoscope 4000 Series, Pico Technology, Cambridgeshire, UK) that was connected to the control computer. t_{col} was defined as the time between the shockwave signal from the initial expansion of the bubble cloud and the shockwave signal from the first collapse of the bubble cloud. To parse the expansion and collapse signals from the acquired signals, the hydrophone data were filtered with a 1D Gaussian band-pass filter centered at 6 MHz with a Gaussian root-mean square width of 1 MHz.

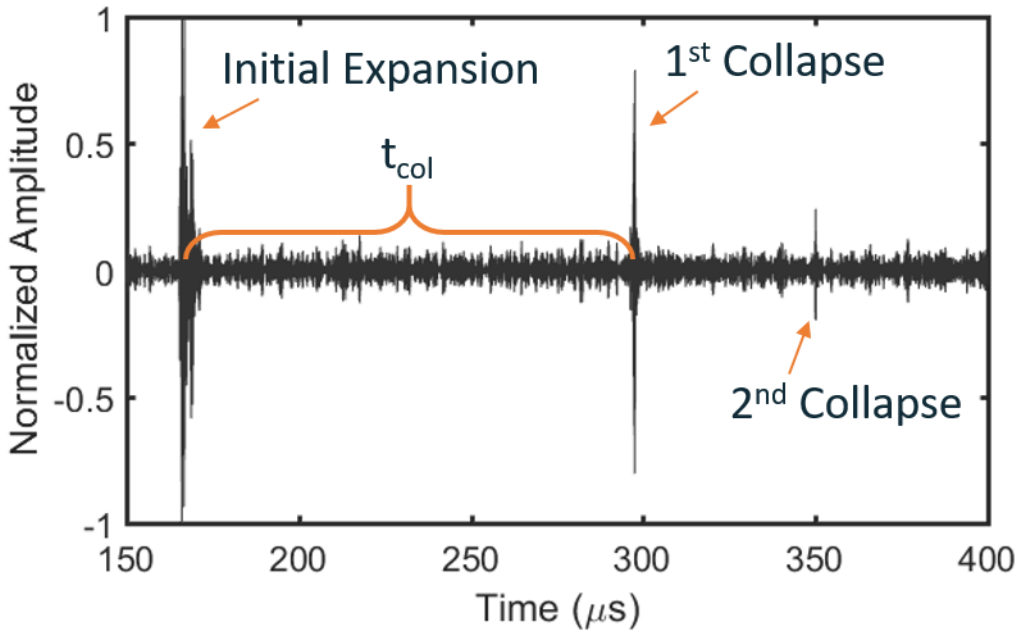

Figure 4.2: Representative bubble cloud expansion and collapse signals acquired from hydrophone in an agar phantom after frequency-domain filtering using a Gaussian shaped filter with a 6 MHz center frequency and a Gaussian root-mean square width of 1 MHz. Time zero represents time at which the histotripsy array was fired. The t_{col} is calculated as the time between the peak expansion signal and the peak collapse signal. The initial expansion and first collapse signals were readily observable for all treatments of all phantoms and tissue samples.

This filter was chosen because it eliminated the low frequency oscillations around the 500 kHz center frequency of the histotripsy transducer and also reduced very high frequency noise while still passing high frequency components of the broadband shockwave emissions from the bubble cloud. A representative cavitation emission signal from a single bubble cloud recorded on the side-mounted hydrophone is shown in Figure 4.2. After filtration, the acoustic shockwaves emitted from the initial expansion and collapse of the bubble cloud had amplitudes that were approximately an order of magnitude greater than the noise floor. Assuming a fixed sound speed of 1480 m/s, the time of arrival of the shockwave from the initial expansion was predictable. The overall durations of the detected expansion and collapse signals were on the order of 1 μs. Because both the expansion and collapse emission signals were expected to be high-pressure, single-cycle

shockwaves [37, 38], the arrival times for the expansion and collapse signals were chosen to be the peak pressure arrival times for each signal. Therefore, to calculate t_{col}, the time between the expansion and collapse signals was directly measured by calculating the time between the peaks of the two largest signals over the lifespan of the histotripsy bubble cloud.

4.2.3 Experiment 1 - Hydrophone-Acquired and High Speed Camera-Acquired Collapse Time Change in Agarose Phantoms of Varying Stiffness

The goal of this experiment was to test the hypotheses that 1) the t_{col} of the cavitation bubble cloud increases with both decreasing phantom stiffness and increasing histotripsy treatment; and 2) use optical images of the bubble cloud expansion and collapse to validate the t_{col} measurements acquired using the acoustic shockwave emitted from the collapse of the bubble cloud. Histotripsy-induced cavitation was generated in agarose gel phantoms with varying stiffness, and t_{col} was calculated using the acoustic shockwave emitted from the cavitation and validated using high-speed optical images of the cavitation bubble cloud.

Previously, it has been shown that agar phantoms can be used to model a physiologically relevant range of tissue mechanical properties by modifying the concentration of agar in the phantom [23]. Typically, the compressional Young's moduli for low melt temperature agar phantoms range from approximately 38 kPa at 1.0% concentration to approximately 929 kPa at 5% concentration [39]. For comparison, typical physiological compressional Young's moduli range from ~2-5 kPa for the weakest tissues, e.g., lung, fat, and ~900 kPa for the strongest tissues, e.g., cartilage [40]. For this study, low melt, molecular biology grade agar (CAS No. 9012-36-6, DOT Scientific, Burton, MI) was dissolved in boiling deionized water to form tissue-mimicking phantoms in a rectangular mold approximately 9 x 12 x 1.25 cm in size. The molds were designed

to reduce acoustic aberrations by ensuring that no structural supporting materials were placed between the histotripsy array and the phantoms to reduce acoustic aberrations. Four different types of agar gels were formed using concentrations of 1.0%, 1.5%, 2.5%, and 5.0% w/v to interrogate the relative differences in bubble dynamics across samples of varying stiffness. Phantoms were treated in replicates of six justified by power analysis to performed to obtain a statistical power of 0.95 and $\alpha = 0.01$ for observing the difference in t_{col} between agar concentrations when compared to a normal distribution. All phantoms were degassed in a vacuum (WOB-L 2581, Welch Vacuum, Mt. Prospect, IL) in a desiccator for ten minutes prior to solidification to remove small gas bubbles. Upon solidification, phantoms were removed from their molds and were placed in the water tank above the histotripsy array using a three-axis positioning system for treatment. The driving voltage used to treat these agar phantoms resulted in an estimated P- pressure of 33.1 MPa, which was measured as the summation of four array subapertures. This was just above the intrinsic threshold for cavitation generated using a single-cycle pulse [41], so cavitation only occurred at the area of highest pressure at the focus of the transducer and not throughout the entire -6 dB beamwidth. It is important to note that the linear summation of subapertures does not perfectly account for the effects of nonlinear propagation, so this P- pressure measurement is likely an overestimate.

Hydrophone-acquired measurements of t_{col} were obtained throughout the entire treatment of each tissue-mimicking phantom. For the first pulse in each treatment of each phantom, t_{col} measurements were directly compared to observe the effects of varying stiffness of intact phantoms on t_{col}. The overall change of t_{col} throughout treatment relative to the t_{col} from the first pulse was then calculated to compare the t_{col} progression profiles throughout the treatment of each phantom.

A high-speed camera (Phantom V210, Vision Research, Inc., Wayne, NJ) with a 200-mm lens was used to acquire optical images of the bubble cloud expansion and collapse at 125,000 frames-per-second with 8-μs temporal and 45.5-μm spatial resolution with an exposure of 2.0 μs per frame. While this is relatively poor spatial resolution, the maximum bubble sizes observed were on the order of >1 mm, so this resolution was satisfactory for this experiment. For each histotripsy pulse, 38 frames were acquired providing approximately 300 μs of high-speed images per histotripsy pulse. A custom-built diffuse light source was used to backlight the samples. tcol measurements were obtained from the high-speed images by using a summation of a binary mask of each frame to determine whether the bubble cloud was present [42]. The camera-acquired progression of t_{col} was then correlated with the hydrophone-acquired progression of t_{col} throughout all treatments using linear regression to optically validate the hydrophone data.

4.2.4 Experiment 2 - Correlation Between Change of Collapse Time and Lesion Development in Red Blood Cell Phantoms

The goal of Experiment 2 was to test the hypothesis that the increase of t_{col} over the histotripsy treatment can be used to detect the progression of tissue fractionation generated by histotripsy. To provide a quantifiable indication of histotripsy-induced tissue fractionation, tissue-mimicking agar phantoms made from a thin layer of RBCs embedded between two layers of agar were treated with histotripsy. RBC phantoms have been previously shown to be a good indicator of histotripsy-induced fractionation because the RBC area turns from an opaque red when undamaged to a translucent pink when they are fractionated [43, 44]. High-speed optical images of the RBC phantom can be taken after each pulse to visualize and quantify the damaged area. To form the RBC phantoms, fresh bovine blood acquired from a local abattoir was mixed with citrate-

phosphate-dextrose solution (#C7165; Sigma-Aldrich Co., St. Louis, MO, USA) to prevent clotting [45]. The blood was then placed in a vial in a centrifuge at a relative centrifugal force of 1300 g for 15 minutes. Once separated, the plasma and buffy coat was aliquoted from the sample, leaving only packed RBCs. Agar was dissolved in a 1.0% concentration in boiling, phosphate-buffered saline (PBS). The phantom holder from the first experiment was half-filled with the hot agar-saline solution, which was then allowed to cool thereby forming the bottom layer of the three-layer phantom. RBCs were then added to a small amount of 1.0% agar-saline solution at 40 °C to form a 2.5% RBC-agar-saline w/w solution, which was then poured over the bottom agar layer to form a roughly 0.5 mm thick layer that was then allowed to solidify. Finally, a top layer of 1.0% agar-saline solution was added to complete the phantom thereby completely enclosing the RBC layer in agar gel.

To ensure that the RBC phantom layer was completely engulfed by the bubble cloud throughout the entire -6-*dB beamwidth, the histotripsy transducer was driven well above the intrinsic threshold level for cavitation. At the voltage levels used for the treatments in this experiment, the histotripsy array was estimated to output a P- pressure of 59.4 MPa when measured as a summation of eight subapertures using the FOPH.

To analyze the extent of histotripsy-induced destruction optically, a high-resolution camera (Point Grey Chameleon 3, FLIR Systems, Inc., Richmond, BC, Canada) and macro lens were used to take an image of the area of destruction after each histotripsy pulse with an effective resolution of 11.4 μm/pixel. The samples were backlit by a custom-built diffuse light source. To compute a quantitative metric for fractionation progression, an approximately 0.52 mm^2 region of interest (ROI) in the center of the lesion was extracted from each image to limit the effects of peripheral damage on the mean lesion intensity (MLI) metric. The MLI, defined as the average pixel intensity

over the ROI, was calculated for the entire treatment on a normalized scale from 0 to 1 following the protocol established from previously published work [46, 43]. The exposure settings of the camera were calibrated such that an untreated area resulted in an average MLI of 0 and an area of complete destruction resulted in an MLI of 1. Thus, an MLI of 1 was used to indicate complete fractionation. Hydrophone-acquired measurements of t_{col} for each histotripsy pulse were correlated with the change in MLI using linear regression for six treatments to validate the change in t_{col} as a measure of tissue fractionation. The sample size was determined using power analysis to obtain a statistical power of 0.95 and $\alpha = 0.05$ for observing the change in MLI throughout treatment.

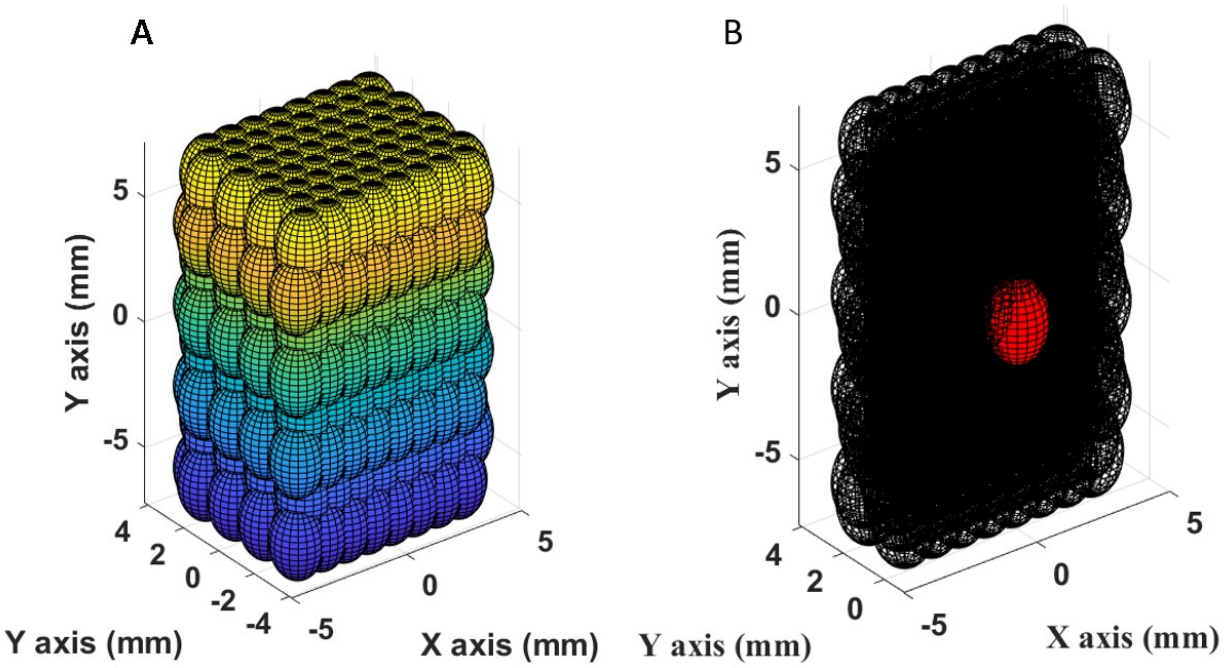

Figure 4.3: (A) treatment grid used in volumetric treatments in Experiment 4. (B) Cross-section of Experiment 4 volumetric treatment grid revealing the focal location (red) at which receive-data was acquired with the 112-element receive-capable histotripsy array.

4.2.5 Experiment 3 - *Ex Vivo* Bovine Liver Treatment

The goal of Experiment 3 was to validate the increasing trend of t_{col} over the histotripsy treatment in *ex vivo* tissue. To make *ex vivo* liver samples, freshly excised bovine liver was

acquired from a local abattoir and was preserved in room-temperature phosphate-buffered saline (PBS) during transport. All liver samples were used within 12 hours of harvest. Cube-shaped samples of approximately 4 cm were cut from the outermost sections of the left and right lobes of whole liver to obtain sections away from large vasculature. Samples were then placed in degassed PBS under vacuum in a desiccator for five hours. Liver samples required a longer degassing period than agar phantoms due to natural gas formation in excised tissue. The liver cubes were then removed from the vacuum and were embedded in 1.5% agar blocks to maintain structural stability [47]. The tissue cubes were suspended in sample holders such that no structural support materials occluded the acoustic signal path of the histotripsy array. Upon solidification of the agar block, phantoms were removed from their molds and were positioned in the water above the histotripsy array using a three-axis positioner. Four liver samples were treated with 1000 histotripsy pulses at a single location at the geometric focus of this histotripsy array. This sample size was determined via power analysis to obtain a statistical power of 0.95 with $\alpha = 0.05$ for observing the change in t_{col} throughout treatment.

Due to the increased intrinsic threshold for cavitation in liver tissue relative to agar phantoms [23], the histotripsy transducer was driven well above the free-field intrinsic threshold for cavitation for the liver samples in this experiment. Therefore, the driving voltage used for treating all *ex vivo* samples was estimated to output a P- pressure of 59.4 MPa if the array were driven in the free-field at that voltage. This was the same driving voltage used for the RBC phantom treatments in the second experiment.

4.2.1 Experiment 4 - Collapse Time Monitoring using a Receive-Capable Histotripsy System

To investigate the ability for a receive-capable histotripsy array to self-monitor the progression of a volumetric histotripsy treatment, the retrofitted, receive-capable, 112-element, 500 kHz histotripsy array described in Section 3.3 was used to treat *ex vivo* bovine liver. Under the driving conditions used for this experiment, this array produced a -6 dB beamwidth of 1.65 mm laterally and 6.5 mm laterally. This focus was steered over an 8x8x8 location grid with 1-mm lateral and 2-mm axial focal spacing making a lesion volume of approximately 1 cm^3 (Figure 4.3A). At the central location of this lesion (Figure 4.3B), the t_{col} of the histotripsy bubble cloud was measured by all elements of the histotripsy array as well as a broadband hydrophone placed near the histotripsy array and laterally to the lesion in the same fashion as the lateral hydrophone shown in Figure 4.1. Six 1% agarose gel phantoms and six *ex vivo* bovine liver samples were treated to 500 pulses-per-location, and the correlation between change in t_{col} measured with the histotripsy array and hydrophone was calculated to validate the method of using a receive-capable histotripsy array for therapy monitoring.

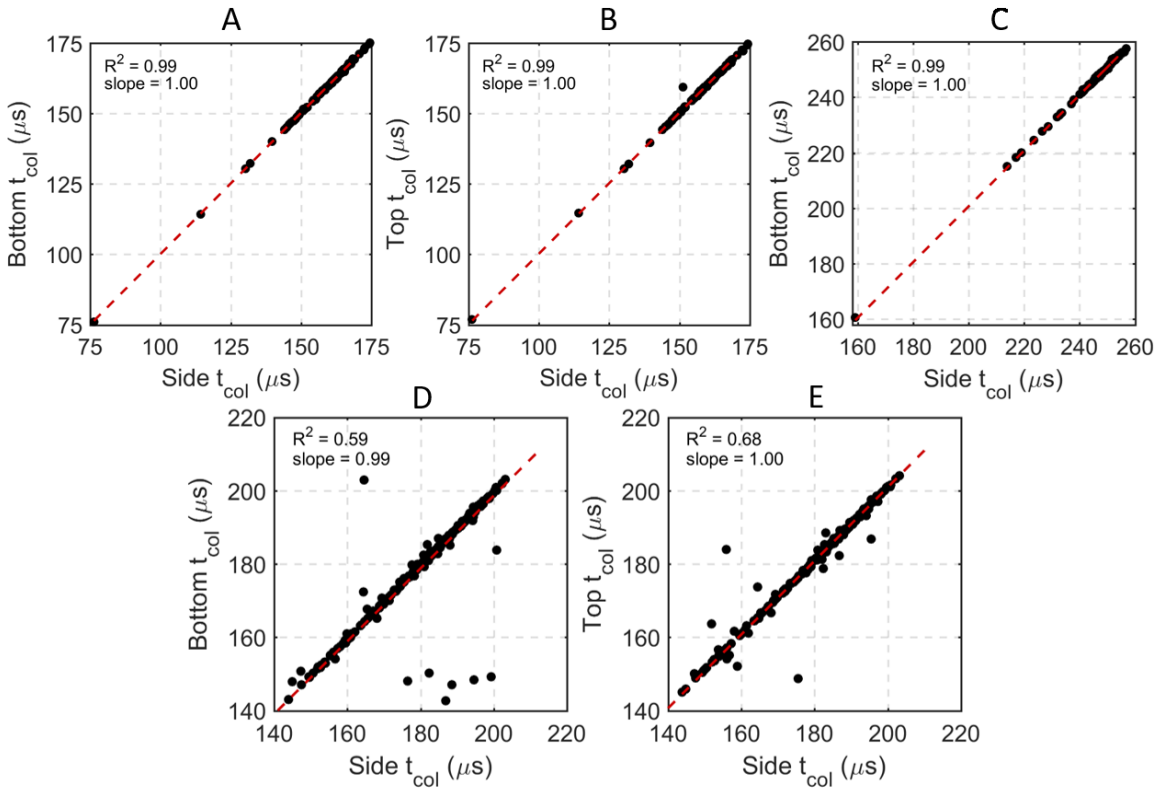

Figure 4.4: Comparisons of t_{col} acquired from top- bottom- and side-mounted hydrophones for one 100-pulse treatment in a 1.0% agar phantom (Experiment 1) (A, B), one 100-pulse treatment in a 1.0% RBC phantom (Experiment 2) (C), and one 1000-pulse treatment (every third pulse) in an ex vivo bovine liver sample (Experiment 3) (D, E). The top-mounted hydrophone was blocked by the RBC phantom holder for Experiment 2, thus it could not be compared to the other two hydrophones. A strong, linear, direct correlation was observed in all comparisons, indicating that the t_{col} recorded on all three hydrophones were virtually identical.

4.3. Results

4.3.1 Agarose Phantom Treatment

A total of 28 single-location lesions were generated in transparent phantoms with four different concentrations of agar. An example filtered signal from one hydrophone from one histotripsy pulse in a 1.0% agar phantom is shown in Figure 4.2. In this signal, the emission

shockwaves from the initial expansion, first collapse, and second collapse of the bubble cloud are observed around 170, 295, and 350 μs, respectively. Note that while the initial expansion and first collapse signals were observable in all experiments, the second collapse signal was only observable in some cases and generally only in the 1.0% and 1.5% agar gels. In all samples, the cavitation collapse signals were observable on all three hydrophones, and the t_{col} measurements from all three hydrophones were virtually identical. Example hydrophone comparisons from one treatment of one 1.0% agar phantom from this experiment are shown in Figure 4.4A,B and indicate very strong, direct linear correlations between the side-mounted and the top- and bottom-mounted hydrophones. In this experiment and subsequent experiments, forward and reverse scattering of the histotripsy pulses occasionally interfered with the collapse shockwave signals on the top- and bottom-mounted hydrophones, thus making it difficult to extract t_{col} from the data in some cases. However, the side-mounted hydrophone did not experience this issue due to its placement away from the transaxial direction of the histotripsy transducer. Therefore, for consistency, all quantitative t_{col} data reported in this manuscript are from the side-mounted hydrophone other than the comparative linear correlations reported in Figure 4.4.

For the first pulse in each treatment, a decrease in t_{col} acquired from both the hydrophone and the high-speed camera was observed with increasing stiffness [24, 39]. As shown in Figure

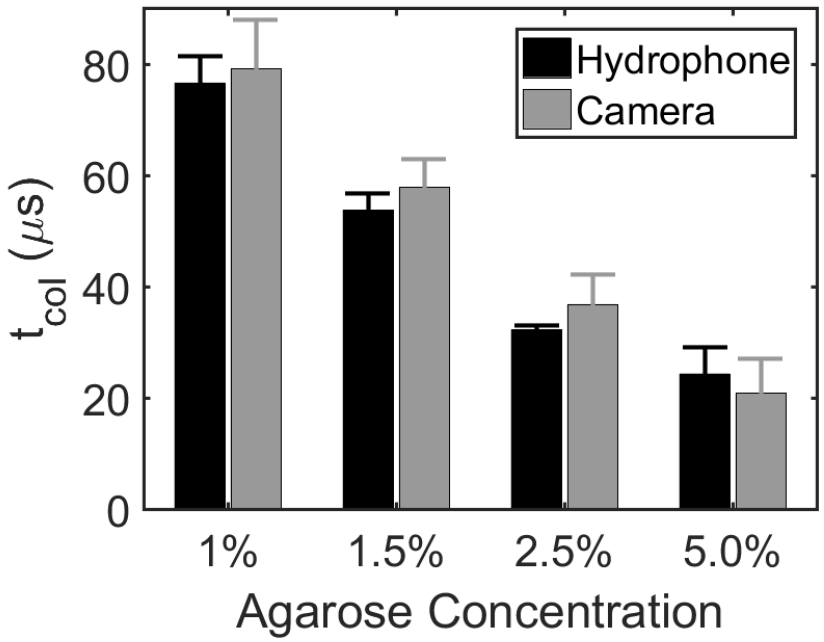

Figure 4.5: Bubble cloud t_{col} in tissue-mimicking phantoms of varied agar concentration acquired from both hydrophone and high-speed camera. Results show t_{col} for the first histotripsy pulse in six replicate treatments of four different agar concentrations. A significant decrease in t_{col} with increasing agarose concentration was observed. All differences in t_{col} due to different agar concentrations were found to be statistically significant using Tukey's HSD multiple comparisons test (p-values < 0.001) t_{col} measurements were not statistically significantly different between hydrophone and camera (p-value = 0.16).

4.5, the t_{col} at the beginning of each treatment was found to be 77 ± 4.8, 56 ± 2.8, 32 ± 0.7, and 26 ± 4.7 μs on the hydrophone and 80 ± 7.7, 58 ± 4.1, 37 ± 4.2, and 21 ± 5,2 on the high-speed camera for the 1.0%, 1.5%, 2.5%, and 5.0% agar concentration phantoms, respectively. Differences between t_{col} measurements on the first pulse between all agar concentrations were significant (*p-values* < 0.001), and differences between t_{col} measurements on the hydrophone and high-speed camera were insignificant (*p-value* = 0.16). For the 1.0%, 1.5%, and 2.5% phantoms, the camera tended to overestimate t_{col} on the first pulse in comparison to the hydrophone, but the opposite effect was observed for the 5.0% phantoms. However, no significant interaction effect between the t_{col} measurement method and the phantom concentration was observed (*p-value* = 0.15).

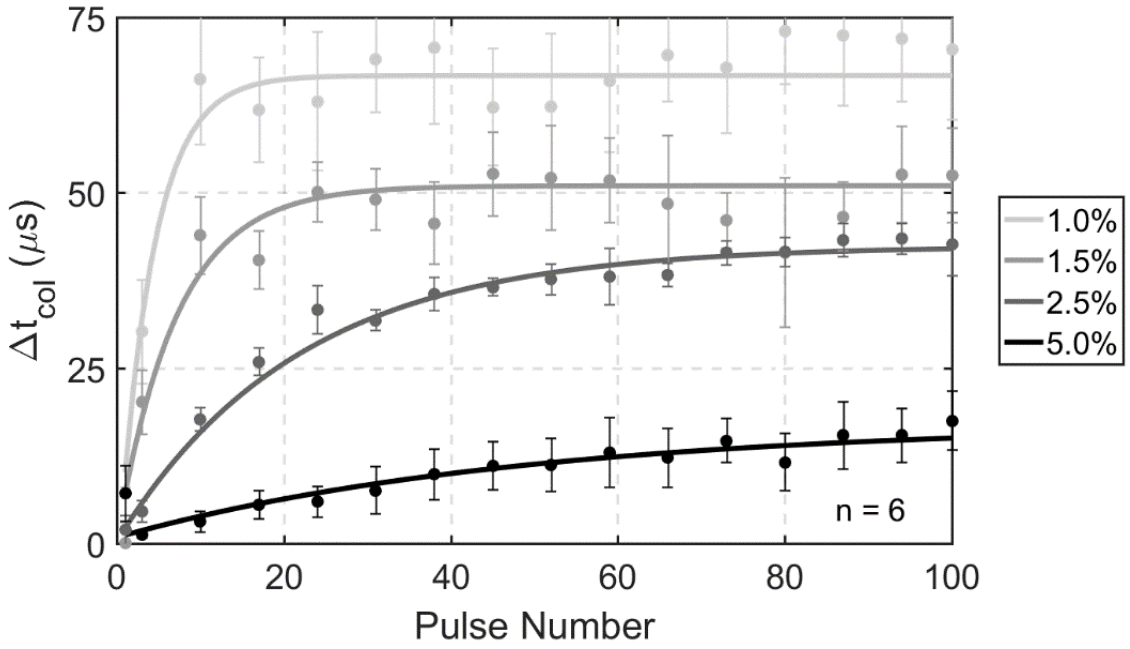

Figure 4.6: Change in t_{col} of bubble clouds throughout 100 pulse treatments in tissue-mimicking phantoms with varying concentrations of agar. Lighter shades of gray correspond with tissue-mimicking phantoms with lower agar concentration and therefore lower stiffness, which exhibited both longer t_{col} and larger changes in t_{col}.

Furthermore, variation between the two measurement methods is to be expected due to the poor temporal resolution of the camera relative to the hydrophone.

The changes in t_{col} based on the hydrophone data throughout six 100-pulse treatments in the four different gel stiffness levels are shown in Figure 4.6. An increasing trend of t_{col} over the treatment was observed for all gel concentrations, and the phantoms with lower agar concentrations reached their maximum t_{col} increases earlier than the higher concentration phantoms. Measurements of t_{col} in the 1.0%, 1.5%, 2.5%, and 5.0% phantoms all exhibited mono-directional increases, with maximum increases of approximately 75, 58, 45, and 18 μs and steady-state increases realized at approximately 18, 28, 70, and 90 pulses, respectively, throughout treatment.

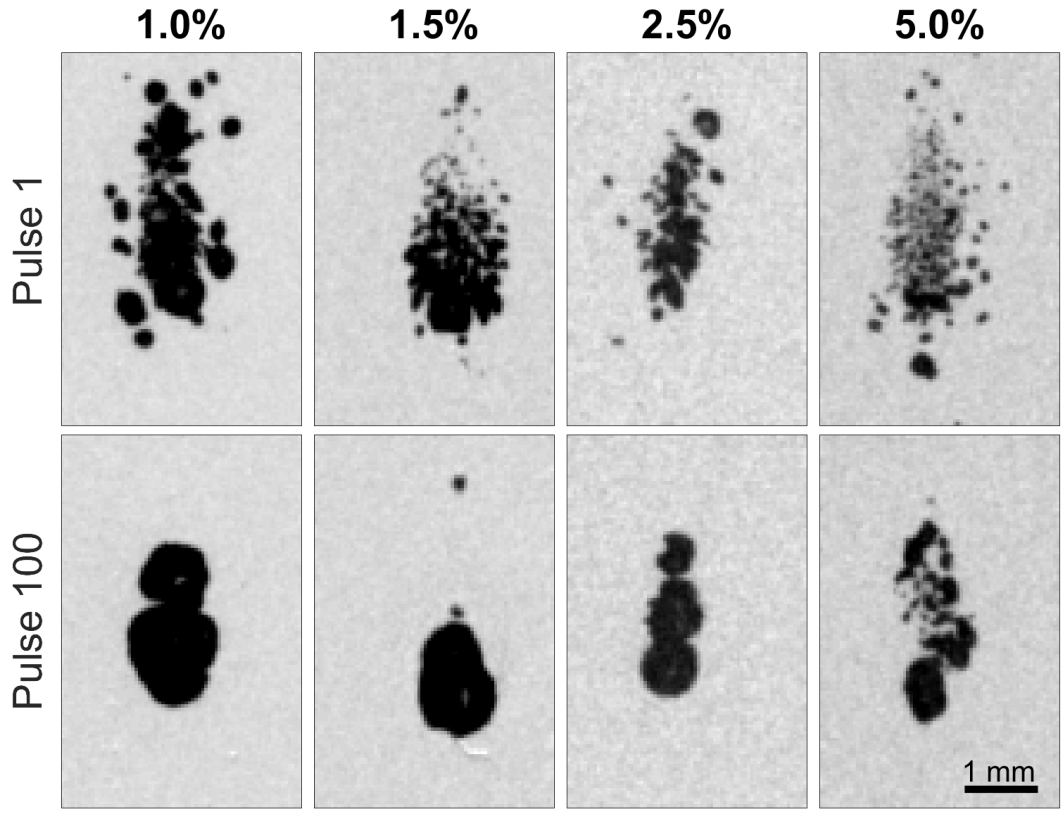

Figure 4.7: High-speed imaging stills of maximum bubble expansion during first and last pulses of 100 pulse treatments of agar tissue phantoms of varying gel concentration. Maximum bubble expansions did not occur at the same time across agar concentrations and histotripsy dosages. At the time of R_{max}, bubbles are smaller and more diffuse for higher agar concentrations and lower treatment dosages.

The high-speed camera data also revealed mono-directional increases with decreasing gel concentration and increasing fractionation over the treatment. The t_{col} measurements in the 1.0%, 1.5%, 2.5%, and 5.0% gels all exhibited mono-directional increases, with the maximum increases of approximately 75, 65, 54, and 25 μs, respectively throughout treatment, with steady-state increases realized at approximately 20, 30, 72, and 90 pulses, respectively. In addition, the high-speed imaging revealed that R_{max} increased with decreasing gel concentration and increasing fractionation over the treatment, which corresponded to the t_{col} data. Stills obtained from the high-

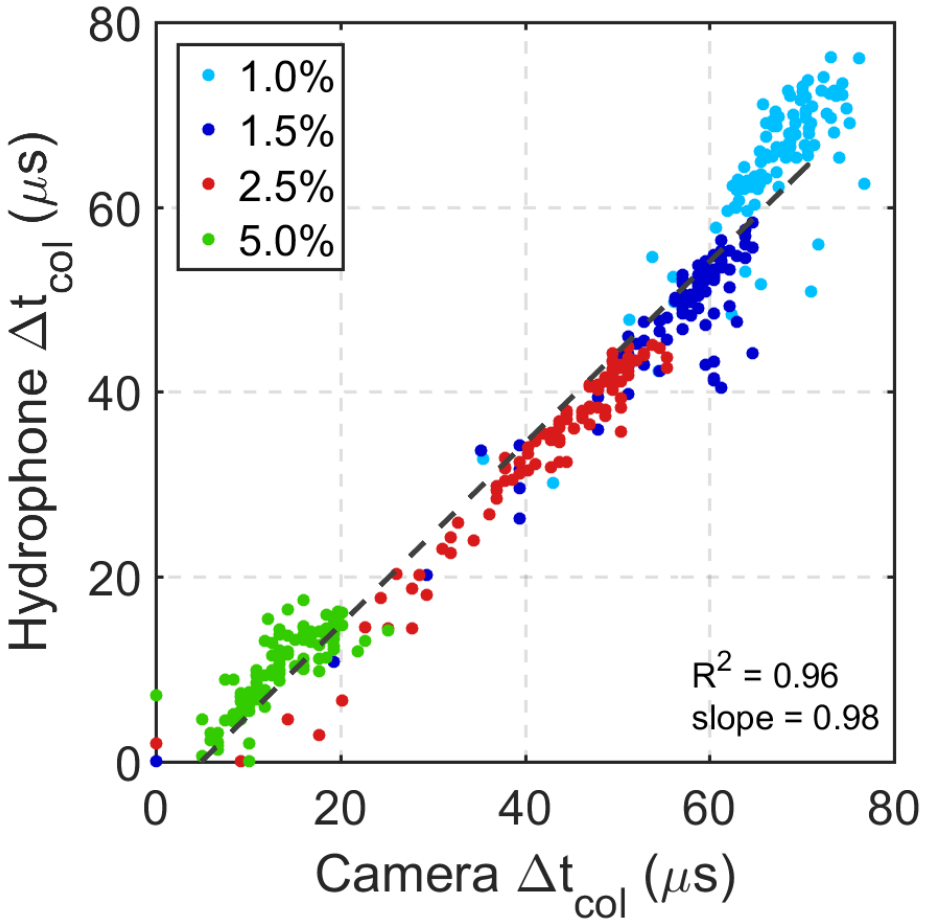

Figure 4.8: Linear correlation between measurements of changes in collapse time t_{col} in agar gels of varying concentration acquired from hydrophone and high-speed imaging data (n=6). Dotted line represents best fit line calculated using linear regression. Δt_{col} calculated from both methods match well with each other. Data from different agar concentrations are easily segmented based on their differences in collapse time.

speed videos at maximum bubble cloud size for the first and last pulses in agar samples of the four different gel stiffness levels are shown in Figure 4.7.

The t_{col} acquired with the camera were in agreement with the hydrophone data throughout the treatments of all phantoms. The mean change in t_{col} over six treatments acquired with the camera is plotted against the mean change in t_{col} acquired with the hydrophone throughout treatment for all agar concentrations in Figure 4.8. Linear regression between the two datasets indicates a strong, linear, direct correlation ($R^2 = 0.96$) with a regression line slope of 0.98.

4.3.2 Collapse Time Correlation with Red Blood Cell Phantom Destruction

The RBC phantom holder was positioned such that the top-mounted hydrophone was blocked and unable to acquire cavitation shockwave signals. However, the comparison between the side- and bottom-mounted hydrophones is shown in Figure 4.4C and indicates a strong, direct, linear correlation indicating that the two locations resulted in identical measurements of t_{col}. Optical images of the RBC layer and t_{col} measurements using the hydrophone were collected for each histotripsy pulse throughout six 100-pulse histotripsy treatments. Qualitative images of the RBC phantom destruction after 5, 15, 25, 50, 75, and 100 single-location histotripsy pulses are shown in Figure 4.9**.** The RBC phantom destruction originated at the center of the bubble cloud where the most intense bubble motion occurs. Significant, rapid increases in destruction were observed throughout the first 25 pulses with decreasing amounts of destruction occurring to 50 pulses. After 50 pulses, little to no increases in destruction based on the optical images were observed in the central part of the lesion. Fractionation of the RBC phantom was quantified for all lesions using the MLI metric and is shown in Figure 4.10. The quantitative optical analysis revealed that the majority of destruction occurred within the first 40 pulses in which logarithmic growth of the MLI metric was observed. Between 40-50 pulses, the MLI began to saturate in all cases indicating complete fractionation. Additional histotripsy pulses beyond this point resulted in essentially no increase in MLI for the center of the lesion.

The t_{col} progression in the RBC phantoms is plotted with the MLI metric data in Figure 4.10. In agreement with the MLI metric data, the t_{col} progression exhibited mono-directional, logarithmic growth until saturating at approximately 40-50 pulses. The bubble cloud for the first pulse of each treatment collapsed at 149 ± 2.4 μs. A large increase in t_{col} of approximately 50 μs

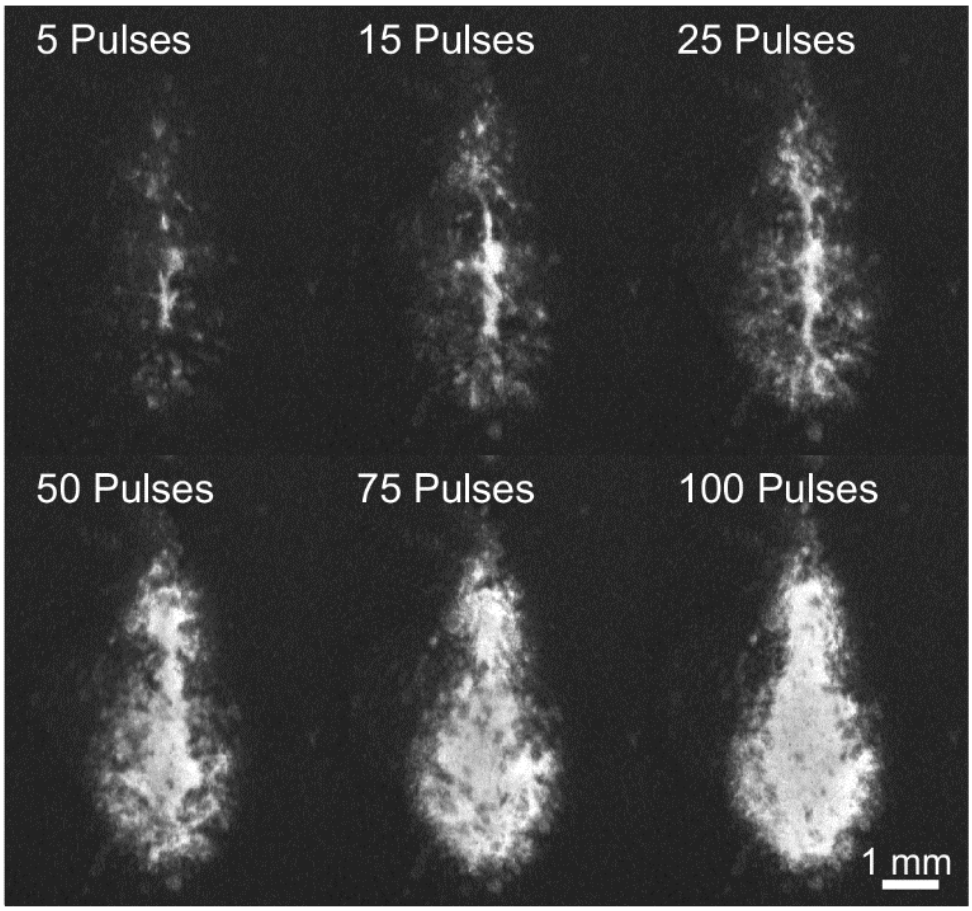

Figure 4.9: Images of RBC phantom destruction throughout one 100-pulse histotripsy treatment illustrating the changes in MLI. Dark background represents non-fractionated RBCs while lighter areas within the lesion represent destroyed areas of the RBC layer. While the central region of the lesion reached maximum MLI around 50 pulses, the extent of fractionation continued to grow outward throughout the remainder of treatment.

was observed between the first and second pulses. t_{col} increased rapidly within 20 pulses, reaching 220 μs at approximately 20 pulses. After 20 pulses, t_{col} increased more slowly until approximately 40 to 50 pulses, reaching 230 μs. No significant increases in t_{col} were observed throughout the remainder of the treatment with an average increase in t_{col} of approximately 2 μs between 50 and 100 pulses.

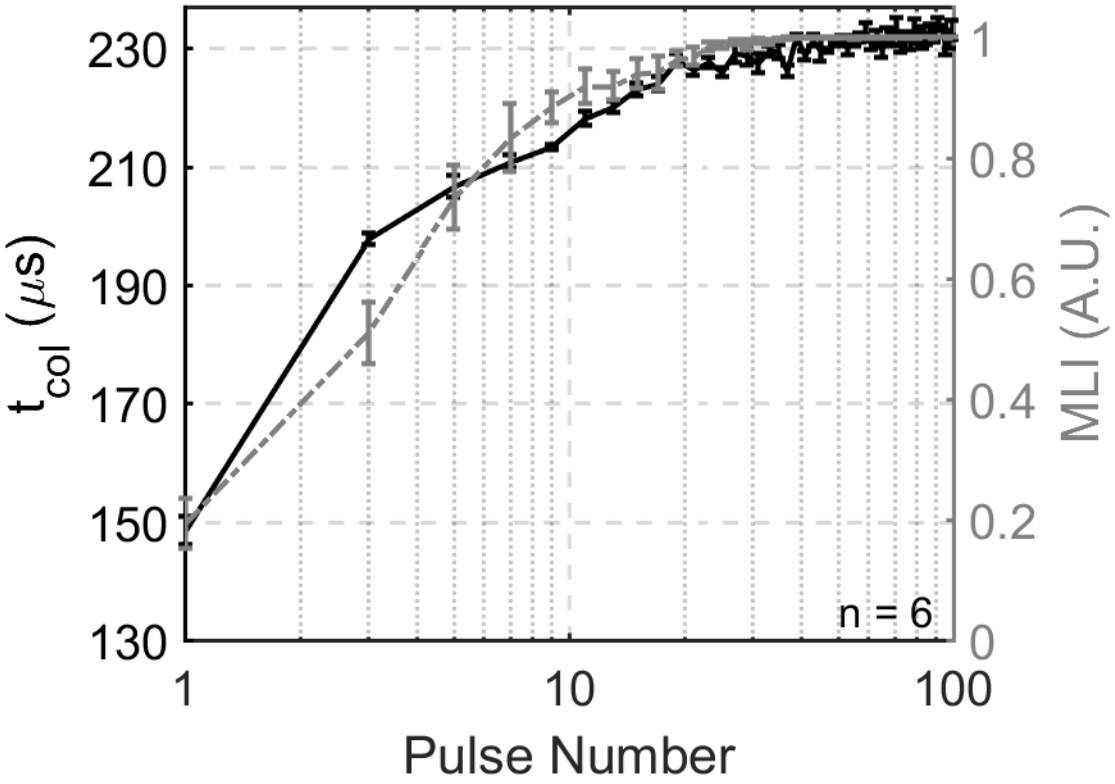

Figure 4.10: t_{col} (left y-axis) and MLI (right y-axis) vs. pulse number throughout 100 pulses. The majority of changes in t_{col} and MLI occur early in treatment and at the same time. The change in t_{col} is greater than the change in MLI in the first several pulses, but both metrics even out quickly and reach a plateau threshold around 40 pulses.

The correlation between the MLI and t_{col} metrics was computed using linear regression to indicate the validity of using the t_{col} metric as a measurement of the degree of tissue fractionation. This correlation is shown in Figure 4.11. Analysis was performed for the entire 100 pulse treatment, and it revealed that a strong linear correlation was observed between the MLI and t_{col} metrics ($R^2 = 0.87$).

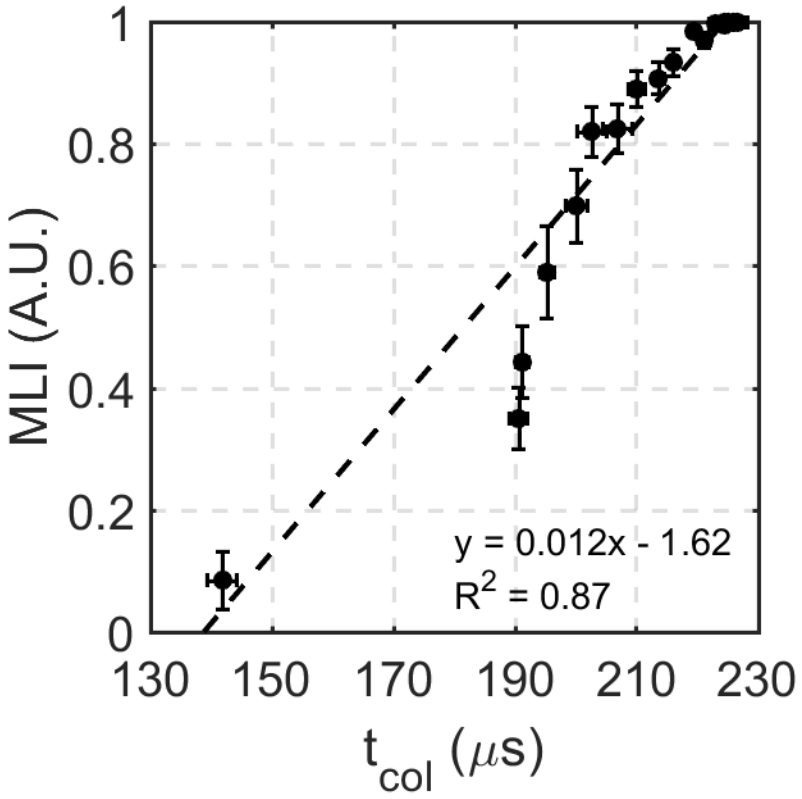

Figure 4.11: Linear correlation between tcol and MLI for 100 histotripsy pulses (n=6).

4.3.3 Ex Vivo Bovine Liver Treatment Collapse Time Monitoring

Direct, linear correlations between t_{col} measurements acquired on the three hydrophones are shown in Figure 4.4D,E. In general, the three hydrophones resulted in identical measurements of t_{col}, indicating that a hydrophone could be placed at any location and still acquire the same t_{col}. The logarithmic growth and saturation trend of t_{col} over the histotripsy treatment was validated in *ex vivo* bovine liver samples. The mean change in t_{col} observed with four *ex vivo* bovine liver treatments is shown in Figure 4.12 for the first 100 pulses (left) and for the full 1000 pulse treatment on a log scale (right). The first pulse of each treatment resulted in an average t_{col} of 153 ± 3.2 μs. During the first 25 pulses, a logarithmic, mono-directional increase in t_{col} of approximately 30 μs was observed. Between 25 and 100 pulses, only a moderate increase in t_{col} of

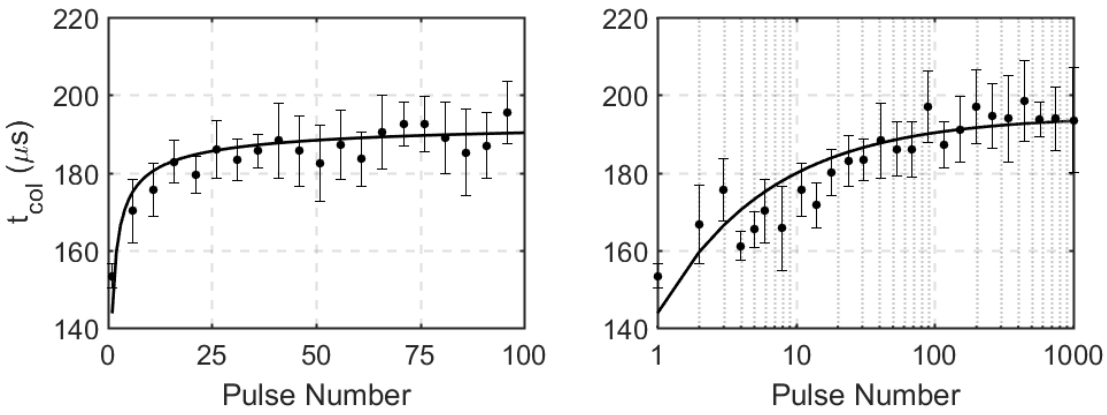

Figure 4.12: Hydrophone-measured t_{col} for first 100 pulses (left, linear scale) and 1000 pulses (right, log scale) in ex vivo bovine liver (n=4). The majority of the change in t_{col} is observed within the first 100 pulses of treatment with little to no change between pulse 100 and pulse 1000.

approximately 10 µs was observed. During the subsequent pulses between 100 and 1000 pulses, little to no substantial increase was observed with maximum t_{col} increases for any treatment of approximately 50 µs in comparison to the first pulse of each treatment. The t_{col} experienced an overall average increase of approximately 40 µs throughout treatment, and it reached this steady-state value of approximately 195 µs t_{col} around 40 to 50 histotripsy pulses.

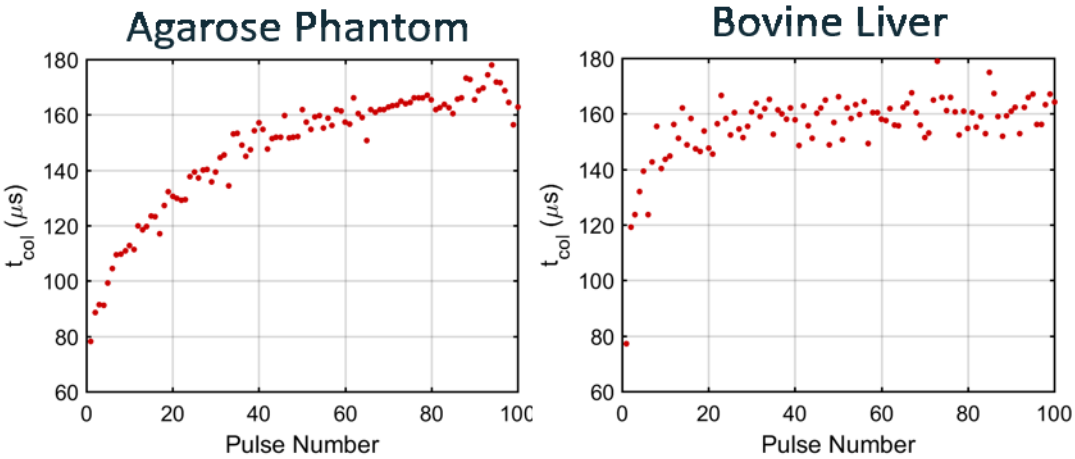

Figure 4.13: Volumetric histotripsy treatment collapse time measurements throughout 100 pulses-per-location at the central location within the lesion for an agarose phantom (left) and bovine liver sample (right).

4.3.4 Receive-Capable Histotripsy System Collapse Time Monitoring

In an ongoing study, six agarose tissue phantoms and six *ex vivo* bovine liver were treated and the collapse time was measured by acquiring shockwave signals on a receive-capable histotripsy array. Example collapse time measurements throughout the first 100 pulses of one treatment of each phantom type are shown in Figure 4.13. In both of these samples, the same logarithmic growth and saturation of the collapse time is observed. A similar trend was observed in all treated samples. These preliminary results indicate that a receive-capable histotripsy array is capable of acquiring collapse time measurements in a similar manner to a hydrophone thereby indicating that this method could be used to monitor treatment in real-time without additional imaging equipment.

4.4. Discussion

Previous work has been reported on the analysis of the cavitation collapse sequence and it's timing relative to the cavitation expansion. Early studies in cavitation physics investigated the cavitation collapse both numerically and experimentally for spherical and asymmetric bubbles to better understand the mechanisms of cavitation-induced damage and jetting [48, 49, 50, 51]. More recently, studies in the field of shock-wave lithotripsy (SWL) have used the collapse time to monitor changes in cavitation dynamics [52] and help detect the presence inertial cavitation [53], and it has been shown that t_{col} tends to increase with an increasing number of shockwaves delivered during SWL treatments [54]. It has been shown that SWL cavitation bubbles formed near the surface of a stone or in areas of more densely populated bubble clouds tend to coalesce into an aggregate larger bubble, thus resulting in a longer collapse time [55, 56].

In this study, the changes in t_{col} due to histotripsy-induced destruction of soft tissue were investigated. The data presented in Experiment 1 support our primary hypothesis that t_{col} increases

significantly with decreasing stiffness of the medium, and increases over the histotripsy treatment as the tissue stiffness is reduced with histotripsy-induced fractionation. These results agree with simulation and experimental data that have been presented previously [12, 24]. These data also support our hypothesis that we can accurately measure t_{col} on a hydrophone using the shockwave emitted by the collapse of the bubble cloud by optically validating the hydrophone data with high-speed images of the bubble cloud. However, there was a non-statistically significant difference in t_{col} measured by the optical images and the acoustic hydrophone in Experiment 1. This discrepancy is likely due to the relatively low temporal and spatial resolution of the optical imaging. In addition, the optical method measured the collapse time via the presence or absence of the bubble cloud while the hydrophone measured the arrivals of the shockwaves emitted by the expansion and first collapse of the bubble cloud. Therefore, the acoustic hydrophone measurement of t_{col} is expected to be more precise than that of optical imaging.

Our second hypothesis that the increase in t_{col} over the histotripsy treatment can be used to monitor the extent of tissue fractionation was supported by the data in Experiment 2 in which RBC phantom destruction was found to correlate linearly with the change in t_{col}. In Experiment 2, the MLI was only calculated over the central area of the lesion. While the MLI saturated by 50 histotripsy pulses, the images in Figure 4.8 indicate that there is a change in the lesion periphery throughout the remainder of the treatment. During a typical histotripsy treatment, the focus would be electronically and/or mechanically steered to other locations with each location overlapping slightly such that the periphery of each lesion is treated redundantly. Therefore, for this study, it was most important to quantify the fractionation just at the center of the lesion because the lesion periphery was not representative of the overall fractionation expected during a typical histotripsy treatment.

The increasing trend of t_{col} over the histotripsy treatment was also validated in *ex vivo* tissue in Experiment 3. The work in Chapter 2 includes a detailed histological analysis of histotripsy-induced tissue destruction in *ex vivo* bovine liver samples using the same transducer and similar treatment parameters as the present study [47]. The destruction of hepatocytes followed a similar trend to the change in t_{col} in the present study, as shown in Figure 4.14. While the destruction of

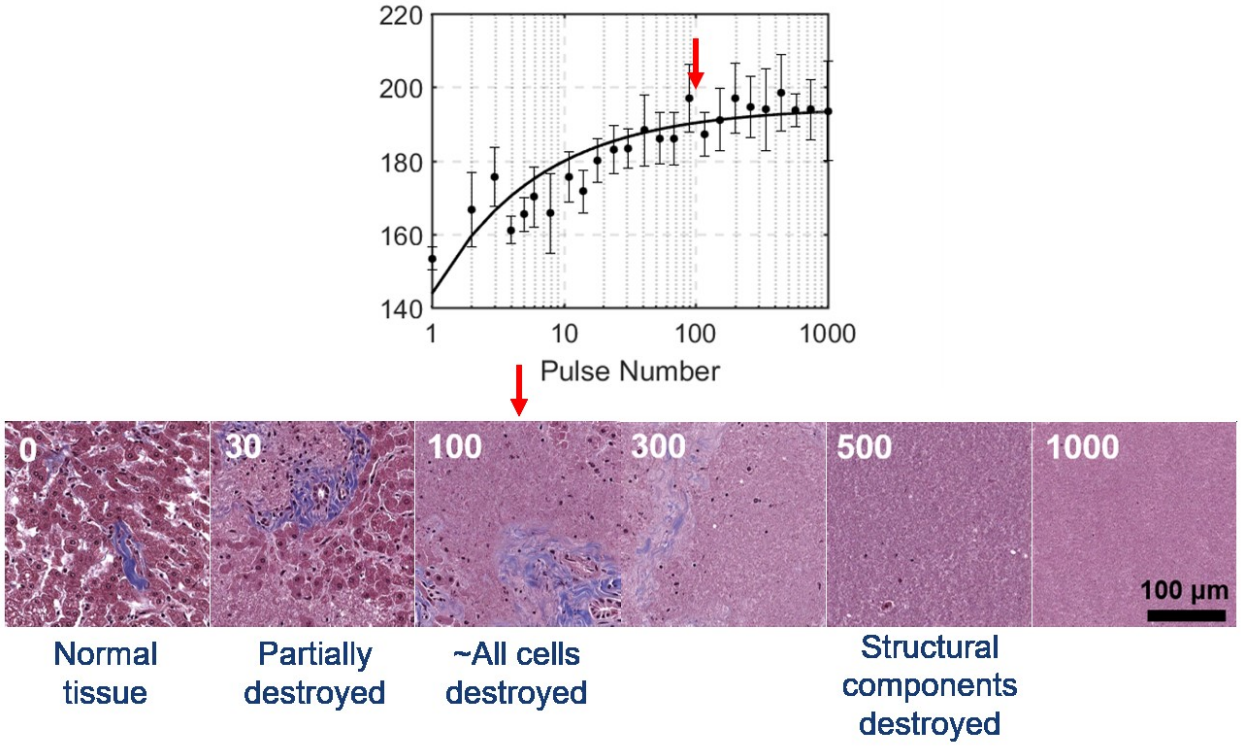

Figure 4.14: Change in collapse time throughout 1000 pulse histotripsy treatments of four *ex vivo* bovine liver samples (top) and histology of ex vivo bovine liver samples at various stages of treatment (bottom). The time at which collapse time stopped changing tended to coincide with the destruction of all hepatocytes.

hepatocytes and the change in t_{col} could not be directly correlated due to the fact that collapse time was not measured for the liver samples from which histology was taken, it was clear that the time at which t_{col} stopped changing tended to correlate with the destruction of hepatocytes. This indicates that t_{col} monitoring may be able to track the extend of cellular destruction while, as was

shown in Chapter 2, the change of the bubble-induced color Doppler profile correlates with the destruction of structural components of tissue.

The majority of hepatocytes were destroyed by 100 pulses and stronger components of the extracellular matrix such as type I and type III collagen fibers were destroyed by approximately 300-500 pulses with complete liquefaction of all tissue by 1000 pulses. In comparison, the majority of the change in t_{col} occurred within the first 50 to 100 pulses in the *ex vivo* bovine liver, thus t_{col} may be primarily influenced by cellular destruction. These data suggest that the cavitation t_{col} may be a good indicator to monitor cell destruction during histotripsy therapy.

While a similar trend in the increase in t_{col} for phantoms of varying stiffness was observed, the data in Experiment 1 indicate that phantoms with higher agar concentrations exhibit smaller and more gradual increases in t_{col} than the phantoms with lower agar concentrations. Previous work done to investigate the effects of tissue phantom mechanical properties on the efficacy of burst wave lithotripsy treatments have indicated that increased viscoelastic resistance is capable of restricting bubble growth and therefore destruction [57]. Furthermore, fatigue-based models that describe material fatigue in agar phantoms due to irreversible fractionation have also been shown to explain changing bubble dynamics throughout cavitation-based treatments [58]. Therefore, we hypothesize that the reduced destruction in higher concentration phantoms observed in this study is due to two factors. First, gels with higher concentrations are expected to take longer to treat with increased resistance to fatigue due to their increased structural integrity. Second, while the phantom may be liquefied within the lesion area, the mechanical properties of a single-focus lesion are likely still influenced by the boundary effects of surrounding intact material. Future studies will investigate differences in t_{col} profiles in varying tissues and within volumetric histotripsy

lesions to indicate if similar variations can be observed in a physiological setting and when boundary effects are eliminated.

This potential histotripsy feedback method relies on the ability to acquire signals from cavitation collapse sequence throughout treatment. Here, our data indicate that t_{col} can be measured from multiple locations with nearly identical results acquired at three separate positions. While the hydrophone that was positioned to the side of the histotripsy transducer in this study resulted in signals with the highest SNR for this setup, collapse signals were still obtainable from the other two positions and the t_{col} measurements were found to be the same across all hydrophones. Ideally, in practice, a hydrophone would not be needed to measure the collapse time despite its very small footprint. Instead, a receive-enabled histotripsy system could be used to perform the same function during treatment, and work to make this a reality is ongoing. Importantly, one major difficulty to overcome will be the fact that histotripsy elements are very narrowband in comparison to the hydrophones used in this study, which will make shockwave detection more difficult as these are broadband and high-frequency signals. However, as shown in Experiment 4, the narrowband receivers of a 112-element 500 kHz receive-capable histotripsy array are able to measure collapse time in a similar manner to a hydrophone. The fact that histotripsy arrays have hundreds of receivers makes the signal processing required to find the collapse signal within background noise a less challenging task than if there were just a single narrowband receiver. These results indicate that a receive-capable histotripsy array could perform self-monitoring of treatment progression using collapse time monitoring.

Residual cavitation nuclei are small microbubbles that persist well after the histotripsy cavitation bubble cloud has collapsed [36]. It is known that these residual nuclei may affect cavitation dynamics of subsequent bubble clouds, and these effects are known as cavitation

memory effects [34]. After the first histotripsy pulse, a portion of the target-region is liquefied while the rest is still intact. In the interstitial fluid spaces, residual cavitation nuclei will persist longer than in intact tissue [42]. While a low PRF of 1 Hz was used in all treatments of this study in an attempt to reduce cavitation memory effects, some residual cavitation nuclei may still persist, especially in the later stages of treatment when tissues and phantoms are highly liquefied or in weaker, lower concentration agar phantoms. However, the variability of t_{col} observed in this study was relatively low. Therefore, future studies will address this issue by observing t_{col} under varying treatment PRFs to indicate the impact of memory effects on t_{col} and then using these observations to gain meaningful insight from the changes of t_{col} under a variety of treatment parameters.

4.5. Conclusions

This study shows that the cavitation bubble cloud t_{col}, which can be measured directly using a broadband hydrophone, increases significantly with decreasing stiffness of the treated medium. It was found that t_{col} increases throughout histotripsy therapy in both tissue-mimicking agar phantoms and *ex vivo* bovine tissue, and it was shown that this increase in t_{col} tracks with histotripsy treatment progression. These preliminary results suggest that observing changes in the cavitation collapse signal may be used as a feedback mechanism for histotripsy-induced tissue fractionation.

4.6. References

[1] J. Macoskey, S. Choi, T. Hall, E. Vlaisavljevich, J. Lundt, E. Johnsen, C. Cain and Z. Xu, "Using the cavitation collapse time to indicate the extent of histotripsy-induced tissue fractionation," *Phys. Med. Biol.,* vol. 63, p. 155013, 2018.

[2] Z. Xu, T. Hall, J. B. Fowlkes and C. A. Cain, "Effects of acoustic parameters on bubble cloud dynamics in ultrasound tissue erosion (histotripsy)," *The Journal of the Acoustical Society of America,* vol. 122, no. 1, pp. 229-236, July 2007.

[3] W. Roberts, T. Hall, K. Ives, J. Wolf Jr., J. Fowlkes and C. Cain, "Pulse cavitational ultrasound: A noninvasive technology for controlled tissue ablation (histotripsy)," *J. Urol.,* vol. 175, pp. 734-738, 2006.

[4] J. Parsons, C. Cain and G. F. J. Abrams, "Pulsed cavitational ultrasound therapy for controlled tissue homogenization," *Ultrasound Me. Biol.,* vol. 32, pp. 115-129, 2006a.

[5] K.-W. Lin, Y. Kim, A. D. Maxwell, T.-Y. Wang, T. L. Hall, Z. Xu, B. J. Fowlkes and C. A. Cain, "Histotripsy beyond the intrinsic cavitation threshold using very short ultrasound pulses: Microtripsy," *IEEE Trans. on Ultrasonics, Ferroelectrics, and Frequency Control,* vol. 61, no. 2, pp. 251-265, February 2014.

[6] X. Zhang, J. Macoskey, K. Ives, G. Owens, H. Gurm, J. Shi, M. Pizzuto, C. CA and Z. Xu, "Non-Invasive Thrombolysis Using Microtripsy in a Porcine Deep Vein Thrombosis Model," *Ultrasound Med. Biol.,* vol. 43, no. 7, pp. 1378-90, 2017.

[7] T. Whittingham, F. Duck, Baker and S. H. AC, "The Purpose and Techniques of Acoustc Output Measurement," in *Ultrasound in Medicine*, Philadelphia, Institute of Physics Publishing, 1998, pp. 129-148 .

[8] T. Leighton, "The Forced Bubble," in *The Acoustic Bubble*, San Diego, Academic Press, Inc., 1994, pp. 287-438.

[9] Z. Xu, A. Ludomirsky, L. Y. Eun, T. L. Hall, B. C. Tran, B. J. Fowlkes and C. A. Cain, "Controlled Ultrasound Tissue Erosion," *IEEE Trans. Ultrason., Ferroelect., Freq. Control,* vol. 51, no. 6, pp. 726-736, June 2004.

[10] T. Hall, K. Kieran, K. Ives, J. Fowlkes, C. Cain and W. Robers, "Histotripsy of rabbit renal tissue in vivo: Temporal histologic trends," *J. Endoural.,* vol. 21, pp. 1159-1166, 2007a.

[11] E. Vlaisavljevich, Y. Kim, S. Allen, G. Owens, S. Pelletier, C. Cain, K. Ives and Z. Xu, "Image-guided non-invasive ultrasound liver ablation using histotripsy: Feasibility study in an in vivo porcine model," *Ultrasound Med. Biol.,* vol. 39, pp. 1398-1409, 2013.

[12] E. Vlaisavljevich, K.-W. Lin, A. Maxwell, M. Warnez, L. Mancia, R. Singh, A. Putnam, B. Fowlkes, E. Johnsen, C. Cain and Z. Xu, "Effects of ultrasound frequency and tissue stiffness on the histotripsy intrinsic threshold for cavitation," *Ultrasound Med Biol,* vol. 41, no. 6, pp. 1651-1666, June 2015a.

[13] C. Cain and T.-Z. Wang, "Imaging feedback of histotripsy treatments with ultrasound transient elastography". United States Patent US 20130102932 A1, 10 Oct 2012.

[14] R. Miller, A. Maxwell, T.-Z. Wang, J. Fowlkes, C. Cain and Z. Xu, "Real-time elastography-based monitoring of histotripsy tissue fractionation using color Doppler," in *IEEE International Ultrasonics Symposium*, Dresden, Germany, 2012.

[15] T.-Z. Wang, T. Hall, Z. Xu, J. Fowlkes and C. Cain, "Imaging feedback of histotripsy treatments using ultrasound shear wave elastography," *IEEE Trans. Ultrason., Ferroelect., Freq. Control,* vol. 59, no. 6, pp. 1167-81, 2012a.

[16] T.-Z. Wang, T. Hall, Z. Xu, J. Fowlkes and C. Cain, "Imaging feedback for histotripsy by characterizing dynamics of acoustic radiation force impulse (ARFI)-induced shear waves

excited in a treated volume," *IEEE Trans. Ultrason., Ferroelect., Freq. Control,* vol. 61, no. 7, pp. 1137-51, 2014.

[17] T. Hall, J. Fowlkes and C. Cain, "A real-time measure of cavitation induced tissue disruption by ultrasound imaging backscatter reduction," *IEEE Trans. Ultrason., Ferroelect., Freq. Control,* vol. 54, no. 3, pp. 569-75, 2007b.

[18] Z. Xu, F. Zhenzhen, T. L. Hall, F. Winterroth, B. J. Fowlkes and C. A. Cain, "Size Measurement of Tissue Debris Particles Generated from Pulsed Ultrasound Cavitational Therapy - Histotripsy," *Ultrasound Med. Biol.,* vol. 35, no. 2, pp. 245-255, February 2009.

[19] X. Yang and C. Church, "A model for the dynamics of gas bubbles in soft tissue," *J. Acoust. Soc. Am.,* vol. 118, no. 6, pp. 3595-3606, 2005.

[20] R. Gaudron, M. Warnez and E. Johnsen, "Bubble dynamics in a viscoelastic medium with nonlinear elasticity," *J. Fluid Mech.,* vol. 766, pp. 54-75, 2015.

[21] J. Estrada, C. Barajas, D. Henann, E. Johnsen and C. Franck, "High strain-rate soft material characterization via inertial cavitation," *Journal of the Mechanics and Physics of Solids,* p. accepted, 2017.

[22] J. Keller and M. Miksis, "Bubble oscillations of large amplitude," *J. Acoust. Soc. Am.,* vol. 68, no. 2, pp. 628-633, 1980.

[23] E. Vlaisavljevich, A. Maxwell, M. Warnez, E. Johnsen, C. Cain and Z. Xu, "Histotripsy-induced cavitation cloud initiation thresholds in tissues of different mechanical properties," *IEEE Trans. Ultrason. Ferroelectr. Freq. Control,* vol. 61, no. 2, pp. 341-352, 2014b.

[24] E. Vlaisavljevich, K.-W. Lin, M. Warnez, R. Singh, L. Mancia, A. Putnam, E. Johnsen, C. Cain and Z. Xu, "Effects of tissue stiffness, ultrasound frequency, and pressure on

histotripsy-induced cavitation bubble behavior," *Phys Med Biol,* vol. 60, pp. 2271-2292, February 2015b.

[25] C. Hua and E. Johnsen, "Nonlinear oscillations following the Rayleigh collapse of a gas bubble in a linear viscoelastic (tissue-like) medium," *Physics of Fluids,* vol. 25, p. 083101, 2013.

[26] C. Barajas and E. Johnsen, "The effects of elasticity on heat and mass diffusion for freely oscillating bubbles in a tissue-like medium," *J. Acoust. Soc. Am.,* vol. 141, pp. 908-918, 2017.

[27] M. Plesset, "Shockwaves from cavity collapse," *Phil. Trans. Royal Soc. A,* vol. 260, no. 1110, pp. 241-244, 1966.

[28] M. Plesset and A. Prosperetti, "Bubbly Dynamics and Cavitation," *Ann. Rev. Fluid Mech.,* vol. 9, pp. 145-185, 1977.

[29] C. Coussios, C. Farny, G. Ter Haar and R. Roy, "Role of acoustic cavitation in the delivery and monitoring of cancer treatment by high-intensity focused ultrasound (HIFU)," *International Journal of Hyperthermia,* vol. 23, no. 2, pp. 105-120, 2007.

[30] M. Gyöngy, M. Arora, J. A. Noble and C. C. Coussios, "Use of Passive Arrays for Characterization and Mapping of Cavitation Activity during HIFU Exposure," Beijing, 2008.

[31] V. Salgaonkar, S. Datta, C. Holland and T. Mast, "Passive cavitation imaging with ultrasound arrays," *J. Acoust. Soc. Am.,* vol. 126, no. 6, pp. 3071-83, 2009.

[32] J. Gateau, J. Aubry, M. Pernot, M. Fink and M. Tanter, "Combined Passive Detection and Ultrafast Active Imaging of Cavitation Events Induced by Short Pulses of High-Intensity

Ultrasound," *IEEE Trans. Ultrason., Ferroelect., Freq. Control ,* vol. 58, no. 3, pp. 517-32, 2011.

[33] J. Macoskey, J. Sukovich, T. Hall, C. Cain and Z. Xu, "Real-time acoustic-based feedback for histotripsy therapy," in *173rd Meeting of the Acoustical Society of America*, Boston, MA, 2017.

[34] A. Duryea, C. Cain, W. Roberts and T. Hall, "Removal of residual cavitation nuclei to enhance histotripsy fractionation of soft tissue," *IEEE Trans. Ultrason., Ferroelect., Freq. Control,* vol. 62, no. 12, pp. 2068-78, 2015a.

[35] J. E. Parsons, C. A. Cain and J. B. Fowlkes, "Cost-effective assembly of a basic fiber-optic hydrophone for measurement of high-amplitude therapeutic ultrasound fields," *J. Acoust. Soc. Am.,* vol. 119, pp. 1432-1440, March 2006b.

[36] T.-Z. Wang, Z. Xu, T. Hall, J. Fowlkes and C. Cain, "An efficient treatment strategy for histotripsy by removing cavitation memory," *Ultrasound Med. Biol.,* vol. 38, no. 5, pp. 753-766, 2012b.

[37] J. Sukovich, T. Hall, J. Macoskey, C. Cain and Z. Xu, "Investigation of the source of histotripsy acoustic backscatter signals," *Journ. Acoust. Soc. Am.,* vol. 141, p. 3551, 2017.

[38] R. Cleveland, O. Sapozhnikov, M. Bailey and C. LA, "A dual passive cavitation detector for localized detection of lithotripsy-induced cavitation in vitro," *J. Acoust. Soc. Am.,* vol. 107, no. 3, February 2000.

[39] V. Normand, D. Lootens, E. Amici, P. KP and P. Aymard, "New insight into agarose gel mechanical properties," *Biomacromolecules,* vol. 1, pp. 730-8, 2000.

[40] E. Vlaisavljevich, Y. Kim, G. Owens, W. Roberts, C. Cain and Z. Xu, "Effects of tissue mechanical properties on susceptibility to histotripsy-induced tissue damage," *Phys. Med. Biol.,* vol. 59, pp. 253-270, 2014a.

[41] A. Maxwell, C. Cain, T. Hall, B. Fowlkes and Z. Xu, "Probability of cavitation for single ultrasound pulses applied to tissues and tissue-mimicking materials," *Ultrasound in Med. & Biol.,* vol. 39, no. 3, pp. 449-465, 2013.

[42] A. Duryea, H. Tamaddoni, C. Cain and W. H. T. Roberts, "Removal of residual nuclei following a cavitation event: a parametric study," *IEEE Trans. Ultrason. Ferroelectr. Freq. Control,* vol. 62, no. 9, pp. 1605-1614, September 2015b.

[43] R. Miller, Z. X, M. AD, C. CA and X. Z, "Bubble-Induced Color Doppler Feedback for Histotripsy Fractionation," *IEEE Trans Ultrason Ferroelectr Freq Control,* vol. 63, no. 3, pp. 408-19, 2016.

[44] A. Maxwell, T.-Y. Wang, L. Yuan, A. Duryea, Z. Xu and C. Cain, "A tissue phantom for visualization and measurement of ultrasound-induced cavitation damage," *Ultrasound Med. Biol.,* vol. 36, pp. 2132-2143, 2010.

[45] X. Zhang, G. E. Owens, C. A. Cain, H. S. Gurm, J. Macoskey and Z. Xu, "Histotripsy Thrombolysis on Retracted Clots," *Ultrasound Med. Biol.,* vol. 42, no. 8, pp. 1903-1918, August 2016.

[46] R. Miller, "Histotripsy for Pediatric Cardiac Applications," Ann Arbor, 2014.

[47] J. Macoskey, X. Zhang, T. Hall, J. Shi, S. Beig, E. Johnsen, F. Lee Jr., C. Cain and Z. Xu, "Bubble-Induced Color Doppler Feedback Correlates with Histotripsy-Induced Destruction

of Structural Components in Liver Tissue," *Ultrasound in Med. & Biol.,* vol. 44, no. 3, pp. 602-12, 2018.

[48] R. Ivany and F. Hammitt, "Cavitation bubble collapse in viscous, compressible liquids - Numerical analysis," *J. Basic Eng.,* vol. 87, no. 4, pp. 977-985, 1965.

[49] T. Mitchell and F. Hammitt, "Asymmetric cavitation bubble collapse," *J. Fluids Eng.,* vol. 95, no. 1, pp. 29-37, 1973.

[50] M. Plesset and R. Chapman, "Collapse of an inertially spherical vapour cavity in the neighborhood of a solid boundary," *J. Fluid Mech.,* vol. 47, no. 2, pp. 283-90, 1971.

[51] C.-D. Ohl, A. Philipp and W. Lauterborn, "Cavitation bubble collapse studied at 20 million frames per second," *Ann. Physik,* vol. 507, no. 1, pp. 26-34, 1995.

[52] O. Sapozhnikov, V. Khokhlova, M. Bailey, J. Williams, J. McAteer, R. Cleveland and L. Crum, "Effect of overpressure and pulse repetition frequency on cavitation in shock wave lithotripsy," *J. Acoust. Soc. Am.,* vol. 112, no. 3, pp. 1183-95, 2002.

[53] A. Coleman, M. Choi and J. Saunders, "Detection of acoustic emission from cavitation in tissue during clinical extracorporeal lithotripsy," *Ultrasound in Med. & Biol.,* vol. 22, no. 8, pp. 1079-87, 1996.

[54] M. Bailey, Y. Pishchalnikov, O. Sapozhnikov, R. Cleveland, J. McAteer, N. Miller, I. Pishchalnikov, B. Conners, L. Crum and A. Evan, "Cavitation detection during shock-wave lithotripsy," *Ultrasound in Med. & Biol.,* vol. 31, no. 9, pp. 1245-56, 2005.

[55] X. Xi and P. Zhong, "Improvement of stone fragmentation during shock-wave lithotripsy using a combined EH/PEAA shock-wave generator - In vitro experiments," *Ultrasound in Med. & Biol.,* vol. 26, no. 3, pp. 457-67, 2000.

[56] M. Tanguay and T. Colonius, "Progress in modeling and simulation of shock wave lithotripsy (SWL)," Osaka, Japan, 2003.

[57] P. Movahed, W. Kreider, A. Maxwell, S. Hutchens and J. Freund, "Cavitation-induced damage of soft materials by focused ultrasound bursts: A fracture-based bubble dynamics model," *J. Acoust. Soc. Am.,* vol. 140, pp. 1374-1386, 2016.

[58] P. Movahed, W. Kreider, A. Maxwell, B. Dunmire and J. Freund, "Ultrasound-induced bubble clusters in tissue-mimicking agar phantoms," *Ultrasound Med. Biol.,* vol. 43, no. 10, pp. 2318-2328, 2017.

CHAPTER 5

Soft-Tissue Aberration Correction for Histotripsy Using the Acoustic Cavitation Emission Signal

This chapter has been published in and was used as the cover art (see Appendix) for *IEEE Transactions on Ultrasonics, Ferroelectrics, and Frequency Control*. 2018; 65(11):2073-2085.

5.1. Introduction

The speed of sound in biological soft-tissue can vary by over 10% between tissue types [2, 3, 4]. These variations, caused by natural heterogeneities in tissue, result in phase aberrations of ultrasound pulses. For therapeutic ultrasound, phase aberrations are the primary source of overall acoustic aberration and can cause severe decorrelation of transmit waveforms thus altering the arrival time of ultrasound pulses emitted by different portions of a therapy array [5]. This effect can reduce the treatment efficacy and, in some cases, prevents treatment altogether [6, 7].

Many aberration correction techniques have been developed for therapeutic ultrasound, and these typically fall into two categories. The first involves using an alternative imaging modality to ultrasound, e.g., magnetic resonance imaging (MRI) or x-ray computed tomography (CT), to obtain pre-operative information about the tissue overlying the target treatment area [8, 9, 10, 11]. This tissue information is then used to estimate sound speed variations across the flight-path of the therapy array and then correct for these variations by applying appropriate phase delays across the elements of a therapy array. While these techniques have been shown to be somewhat successful, especially for transcranial therapies due to the highly aberrating nature of the skull, the efficacy of aberration correction using these methods is less than desired for several reasons. First, these methods only measure the tissue thickness, so several assumptions need to be made to

estimate the sound speed. However, the speed of sound for a specific tissue (e.g., skin, skull, liver) varies across patients and even across locations within the same patient [4]. Second, the corrections acquired from these techniques degrade if the patient moves with respect to the ultrasound therapy array. The second category involves using point targets to correct for acoustic aberrations. These techniques were originally developed for ultrasound imaging [3, 12, 13, 14, 15, 16] and rely on the existence of sparse, point scatterers or sources in the area being imaged, which is not typically the case in biological tissues. By measuring the arrival time variations of sound from a point source across all elements of an ultrasound array, the overall time-of-flight variation from the location of the point source to each element can be accurately estimated. From this information, an ultrasound array can be phased to correct for these variations. It has been shown that cavitation bubbles could be used as a point source for this method [7]. However, cavitation can be difficult to control and maintain in both ultrasound imaging and thermally-based ultrasound therapies, which typically aim to reduce cavitation [17, 18]. Others have suggested a similar approach in which liquid perfluorocarbon droplets are used as point-targets via acoustic droplet vaporization (ADV) [19, 20]. However, this technique requires the injection of the droplet contrast agent, which is neither always desirable nor always feasible depending on the treatment and location. Furthermore, it is difficult to guarantee that the droplets will be in the precise location at which aberration correction is needed.

Histotripsy is a therapeutic ultrasound technique that employs the mechanical forces of highly controlled acoustic cavitation to non-invasively and non-thermally destroy unwanted target tissue [21, 22, 23, 24]. When used via the intrinsic threshold mechanism, histotripsy initiates a cloud of cavitating microbubbles by transmitting a 1-2 cycle length ultrasound pulse with a high-amplitude negative phase, which exceeds an intrinsic threshold to generate cavitation in the target

tissue (~28 MPa peak negative (rarefactional) pressure in water-based soft tissue) [25, 26]. When a histotripsy pulse arrives at the focus of the array, existing cavitation nuclei in the target medium rapidly expand to multiple orders of magnitude larger than their original size [27, 28]. For a single bubble, it is known that this rapid period of expansion emits a shockwave that is focused about the center of the bubble [29, 30, 18]. For a cloud of cavitating bubbles generated with histotripsy, the same shockwave phenomenon is observed and is known as the acoustic cavitation emission (ACE), but less is known about the nature of this construct of shockwaves [31, 32]. It is possible that the cavitation bubbles generated by histotripsy could be used as a point source for aberration correction. However, while the point-source methods for aberration correction are applicable to histotripsy, these methods would require that the histotripsy array be able to receive signals. Histotripsy arrays are traditionally transmit-only systems.

Partially due to this lack of receiver technology, little has been done to correct for acoustic aberrations for histotripsy therapy in real time without a priori knowledge of the propagation medium [33]. The majority of the work on aberration correction for histotripsy has involved placing a hydrophone at the target location and directly measuring the phase aberrations of the pulses emitted by each histotripsy element [34]. This technique has also been previously explored for aberration correction for ultrasonic hyperthermia [35, 36]. While this method has shown success for treatments in which a hydrophone can be placed at the target location such as transcranial histotripsy using a catheterized hydrophone [37], this method is infeasible for the majority of histotripsy therapies including most of those in the abdomen and also prevents histotripsy from being a non-invasive surgery. Without aberration correction, histotripsy has been used to produce lesions in in vivo large animal studies [38, 39, 40], but it is known that overlying soft-tissue causes severe acoustic aberrations resulting in focal pressure loss and reduction in

treatment efficacy [41, 42, 43, 16, 44].

Recently, we have developed receive-capable histotripsy arrays, which has enabled the exploration of aberration correction methods. Based on the fact that the histotripsy bubble cloud emits a construct of shockwaves from the target location during the initial phase of bubble cloud expansion, we hypothesize that these shockwaves can be detected by a receive-capable histotripsy array and used as a point-source signal for aberration correction. We further hypothesize that this will result in a significant recovery of pressure at the array focus and a reduction of array power required to initiate the cavitation bubble cloud. In this study, we test these hypotheses through three sets of experiments. In Experiment 1, we characterize the ACE expansion shockwaves from single bubbles and cavitation clouds generated by histotripsy via optical and acoustic measurements. In Experiment 2, we test the efficacy of using the ACE expansion shockwave from a histotripsy cavitation cloud as a point-source for aberration correction through ex vivo multi-layer heterogeneous porcine abdominal tissue. In Experiment 3, we determine the sound speed variation and attenuation variation due to scattering and absorption through heterogeneous tissue using A-line imaging with a single histotripsy element.

5.2. Materials and Methods

5.2.1 Receive-Capable Histotripsy System

A 112-element, 500-kHz histotripsy array with a 15-cm radius of curvature and 27-cm aperture [45] was used for all experiments in this study. A custom-built, 112-channel, high-voltage pulsing system that generated 1.5-cycle, 3-us sinusoidal pulses was used to drive the transmit portion of the histotripsy array. The array was fired at 1 Hz pulse repetition frequency (PRF) throughout this study. Each transducer element had a diameter of 2 cm. The 112 elements of the

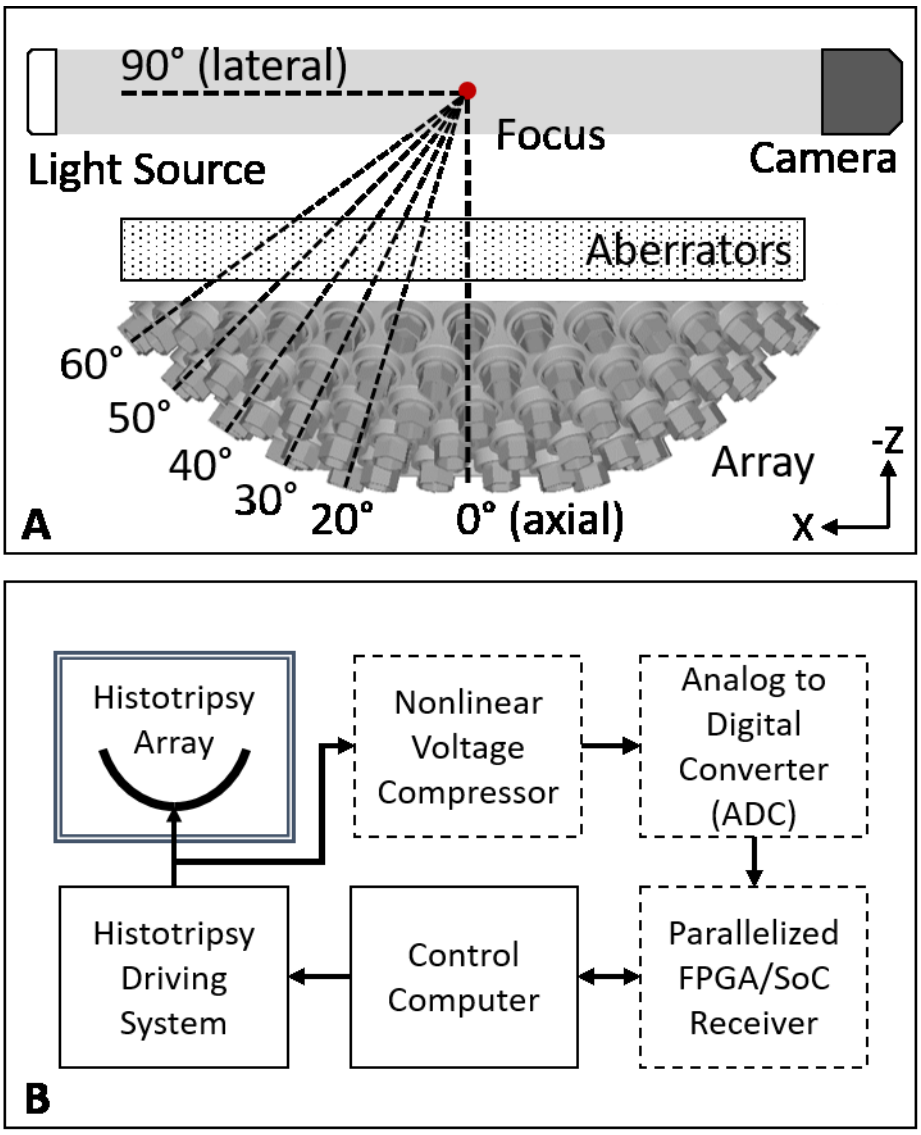

Figure 5.1: (A) 3D rendering of 112-element 500-kHz transducer with angles of each ring relative to the array axis indicated. A light source and camera were placed coaxially along the 90°-axis of the array. For all experiments, aberrators were placed between the array and the focus such that the focal region could be imaged and measured with a hydrophone. (B) High-level overview of receive-capable histotripsy system. A pre-existing histotripsy array was retrofitted with receiver components (dashed line boxes) including the nonlinear voltage compressor, ADCs, and FPGA/SoC-controlled custom receiver.

histotripsy array were organized into five rings at angles of 20, 30, 40, 50, and 60 degrees relative to the axis of the array with the 20-degree ring being the inner-most ring. From inner-most to outer-most, these five rings consisted of 12, 16, 24, 28, and 32 elements. The histotripsy array was placed

facing upwards in a tank filled with filtered, degassed, and deionized water (Figure 5.1A) with the surface of the water approximately 6.5 cm above the array focus. The driving system was controlled by a system of field programmable gate arrays (FPGAs), which allowed each array element to be individually addressable to change the phase of the firing pulse across all elements of the array. The array was calibrated using a custom-built fiber optic probe hydrophone (FOPH) with a 100-μm sensing tip [46]. The FOPH measured a free-field -6 dB focal zone beamwidth of 1.65 mm laterally and 6.50 mm axially when measured in the acoustically linear regime at 10 MPa peak-negative pressure (P-). Above this linear region, the pressure could not be measured directly due to cavitation on the FOPH tip. To estimate the P- greater than 10 MPa, the array was fired in subaperture slices that were driven and measured separately and then summed together. The minimum number of subaperture slices was chosen at each measured pressure level to prevent cavitation on the FOPH tip. This subaperture calibration was performed to better estimate the effects of nonlinear propagation at high pressure levels [47]. This calibration was performed up to the maximum output of the array, which resulted in an estimated focal P- pressure of 63 MPa. It should be noted that this focal pressure is an over-estimation as it does not completely account for non-linear propagation.

To enable the array to receive acoustic signals on all channels, the histotripsy system was retrofitted with an in-house, custom-built, 112-channel receiving system (Figure 5.1B). Each channel of the receiver was directly connected to one channel of the histotripsy array such that the receiver could record both transmit and receive signals on all channels. To protect sensitive downstream electronics in the receiver, a nonlinear voltage compression isolation circuit was placed on the front-end of each channel of the receiver to attenuate high voltage driving signals (2-3 kV/channel) while preserving low voltage ACE signals (10-20 V/channel). The first

component of the compressor was a capacitive voltage divider that attenuated all incoming signals to approximately 10%. The second component was a diode-resistor voltage divider that provided non-linear attenuation to compress signals above approximately 0.7 Volts. Unlike a typical hard-clipping diode voltage-limiting circuit, the diode-resistor simply compressed the signals thus preserving all information within the waveform. Each receiver channel was then digitized by an 8-bit analog-to-digital converter (ADC) with a 20-MHz sampling rate (ADC1175, Texas Instruments, Inc., Dallas, TX, USA). The digitized signals were received by an FPGA/System-on-a-Chip (SoC) embedded processor (Cyclone V SoC, Intel Corporation, Santa Clara, CA, USA) that was integrated with an off-the-shelf hardware platform (DE0-nano-SoC, Terasic, Inc., Hsinchu, Taiwan, China), which interfaced the FPGA/SoC with requisite peripherals and memory including Ethernet hardware. Each FPGA/SoC system was able to receive digitized signals from eight channels of the histotripsy array. Therefore, the receiver system consisted of fourteen FPGA/SoC systems running in parallel. Each FPGA/SoC was routed via Ethernet to the master control computer that was also controlling the driving system. Thus, both the driving and receiving components of this histotripsy system were controlled from one computer. In this system, the control computer was able to control triggering, sample rate, and record length of the receiver system. For all experiments in this study, 400 μs of data were recorded on all elements of the array at a 20-MHz sampling rate, and all receive channels were triggered simultaneously with the transmit pulse.

5.2.2 Experiment 1 – Acoustic Cavitation Emission Expansion Shockwave Investigation

5.2.2.1 Hydrophone Shockwave Investigation

ACE expansion shockwaves were investigated acoustically and optically. To investigate their acoustic nature, a low-frequency calibrated, broadband hydrophone (HGL-0085, Onda Corporation, Sunnyvale, CA, USA) was placed at the axial (0°) and lateral (90°) positions relative to the histotripsy array at a distance of 15-cm from the focus. Shockwaves were generated by bubble clouds that were initiated with estimated free-field focal pressures between 33 and 63 MPa (max power) P- pressure. Shockwave pressures and arrival times were recorded at all pressure levels.

5.2.2.2 Optical Shockwave Investigation

The nature of the shockwaves was investigated optically to better understand the early stages of shockwave initiation, how they change depending on the size of the bubble cloud, and the impacts of these changes on the acoustic nature of the shockwaves. To optically investigate the nature of the shockwaves, a camera (Point Grey Chameleon 3, FLIR Systems, Inc., Richmond, BC, Canada) and macro lens (Macro 100 F2.8D, Tokina Co., Ltd., Tokyo, Japan) were used to acquire shadowgraph images of the bubble cloud with an effective resolution of 14.4 μm/pixel. Shadowgraph imaging is a technique that reveals perturbations in transparent media caused by localized heterogeneities in the refractive index typically due to abrupt temperature or pressure gradients [48]. The camera was back-lit by a custom-built, collimated, high-speed LED light source with a pulse width of approximately 20 ns. Shadowgraph images of bubble clouds and shockwaves were acquired at estimated P- histotripsy focal pressures that generated single cavitation bubbles (28 MPa), multi-bubble clouds (30 MPa), and full-sized, large bubble clouds

(63 MPa). The large bubble clouds were the largest bubble clouds that could be generated by the array without risking damaging the array itself, i.e., at maximum power. It should be noted that large bubble clouds can be generated at P- pressures less than 63 MPa, but the aim of this experiment was to show a full range of possibilities across the output range of a typical histotripsy array. Fifteen shadowgraph images were acquired at each pressure level. From these images, the location of the leading-edge of the shockwaves emitted by the expansion of the bubble clouds was measured at angular increments of 10 degrees between the axial and lateral axes of the histotripsy array to investigate the propagation of different regions of the shockwaves for different types of bubble clouds. Reported distances between the focus and the measured portions of the shockwaves were normalized relative to the distance between the focus and the lateral-axis point of the shockwave to provide a metric for propagation difference across the front edge of the shockwaves. Image analysis was performed using custom image processing software (Matlab, The MathWorks, Natick, MA, USA). Differences in shockwave arrival time across all angles for the three bubble cloud types were statistically analyzed using one-way ANOVA with Tukey's HSD test.

5.2.2.3 Receive-Capable Histotripsy Array Shockwave Investigation

The nature of the ACE expansion shockwaves was also investigated using the receive-capable histotripsy array. Histotripsy bubble clouds were generated with estimated P- focal pressures between 30 and 63 MPa. Both the amplitude and phase (in cycles) of the leading shockwaves were analyzed for fifteen bubble clouds and compared across pressure levels. Amplitude was defined as the peak-to-peak pressure amplitude of the first shockwave to arrive at each element. Phase was defined as the shockwave arrival time difference across all elements of

the array converted to 500 kHz wavelength cycles. The method of phase calculation for the leading ACE shockwave is further discussed in the following section.

5.2.3 Experiment 2 – Aberration Correction Testing

5.2.3.1 Hydrophone-Based Aberration Correction

Two soft-tissue aberration correction methods were used in this study. In the first method, the same broadband, low-frequency calibrated hydrophone from Experiment 1 was placed at the focus of the histotripsy array. The time-of-flight for the ultrasound pulse to travel from each element of the histotripsy array to the focus was measured by the hydrophone, which was then used for aberration correction. To ensure placement at the focus of the array, the hydrophone was manually positioned at the area of highest pressure when firing in the linear regime at approximately 2 MPa P- pressure on the entire array combined – a pressure safe for use with this hydrophone. The correct position of the hydrophone was also optically confirmed using live images on the camera from Experiment 1 that were marked with the central location of the bubble cloud. To acquire the hydrophone-based phase aberration correction for the histotripsy array, each histotripsy element was fired individually at approximately 200 kPa P- pressure. The raw phases, φ_i, of signals, s_i, received on the hydrophone from each element, i, were determined by calculating the lag required to achieve maximum correlation between the signals, given by

$$\boldsymbol{\varphi_i = \underset{\tau}{\mathbf{argmax}}(s_i * s_{max})(\tau)\left(\frac{f_c}{f_s}\right)} \quad \textbf{(E5.1)}$$

where s_{max} is the signal from the element that generated the highest peak-to-peak pressure, τ is the cross correlation lag, and $*$ indicates the cross correlation operation. The $\underset{\tau}{\text{argmax}}()\,(\tau)$

operation, or the arguments of the maxima operation, finds the value, τ, that maximizes the argument in parentheses. Phases were converted from samples to cycles by multiplying by the array center frequency, f_c (500 kHz), divided by the sampling frequency of the hydrophone, f_s (50 MHz). The phases were then inverted such that the uncorrected histotripsy element that emitted the pulse that arrived first at the focus was fired last when aligned, given by

$$\boldsymbol{p_i = \left|\varphi_i - \max_i(\varphi_i)\right|} \textbf{ (E5.2)}$$

The inverted phases, p_i, were then used to alter the phases of the elements in the histotripsy array such that the pulses from each element in the array arrived at the focus simultaneously. This inversion is similar to that used in the time-reversal acoustics method [49]. While this hydrophone-based method is infeasible in an *in vivo* setting as a hydrophone generally cannot be placed at the target location, it was treated as our gold standard method because it should result in the optimal delays required to align the waveforms to the hydrophone location.

5.2.3.2 Acoustic Cavitation Emission Aberration Correction

The second aberration correction method employed the histotripsy receiver system and the ACE signals. By assuming the ACE expansion shockwave to be a spherical shockwave emitted from a point source, the front-edge of this shockwave received by each element of the histotripsy array can be used to correct for phase misalignment due to sound speed variations along the flight-path of each array element [3, 50, 51, 19]. Bubble clouds were generated at maximum array power. It should be noted that the array power cavitation threshold was less than the maximum output of the array in all cases in this study. Thus, a lower pressure level could have been used for ACE

aberration correction. However, maximum power bubble clouds were used here to provide the most high-intensity and consistent shockwaves possible. The round-trip time for sound to travel from the array to the focus and back was approximately 200 μs, so our signal processing was windowed to a region between 190-215 μs to ensure that the signals analyzed principally originated from the ACE expansion shockwave and not reflections in the water tank. Prior to experimentation, signals acquired between 190-215 μs when firing the array at a pressure level just below the intrinsic cavitation threshold level were checked to ensure that signals being used for aberration correction were indeed ACE signals and not reflections from the setup. The ACE shockwave signals from ten histotripsy bubble clouds were then averaged to account for minor pulse-to-pulse differences in shock arrival times due to the stochastic nature of the formation of individual bubbles within each generated bubble cloud. The raw signal phases (converted from samples to cycles) were calculated by finding arrival time of the 50% front-edge of the signal envelope acquired via the Hilbert transform, given by

$$\boldsymbol{\varphi_i = \underset{t}{\operatorname{argmin}} \left| H[s_i(t)] - \frac{1}{2}\max(H[s_i]) \right| \left(\frac{f_c}{f_r}\right)} \quad \textbf{(E5.3)}$$

where H indicates the Hilbert transform operation, and f_r is the sampling frequency of the receiver system ADCs (20 MHz). Phases were then inverted using (2) and used as the phase alignment on the histotripsy array to align the pulses at the focus. The cross-correlation method used for the hydrophone alignment method given by (1) could not be reliably used for the receiver-based aberration correction because the signals after the front-edge of the shockwave were not identical across all elements of the histotripsy array.

5.2.3.3 Comparison Between Hydrophone and Acoustic Cavitation Emission Aberration Correction Methods

The efficacy of the two aberration correction techniques was evaluated by placing aberrators between the array and the focus. Two methods are used for evaluation: 1) measuring the focal pressure through the aberrator(s) after aberration correction using the same driving voltage to the histotripsy array, and 2) measuring the histotripsy array driving system power that is required to generate cavitation through the aberrator after aberration correction. For the first method, the array was driven well below the cavitation threshold in the acoustically linear regime, and the peak-to-peak focal pressure was directly measured via low-frequency calibrated hydrophone. The percent of pressure recovered, $p_{recovered}$, was calculated by dividing the pressure difference between aberration correction, p_{AC}, and no aberration correction, p_{NAC}, through tissue by the pressure difference between the free-field pressure without pre-focal aberrators, $p_{freefield}$, and no aberration correction through tissue, given by,

$$\boldsymbol{p_{recovered} = \frac{p_{AC} - p_{NAC}}{p_{freefield} - p_{NAC}} \times 100\%} \quad \textbf{(E5.4)}$$

Beam profiles were also acquired at this pressure level in the x-, y- (lateral) and z- (axial) directions for ±5-mm in 0.5-mm increments. The (0,0,0)-mm location was set to the focus of the hydrophone-aligned pulse. For the second method, the cavitation initiation thresholds were determined for both hydrophone and ACE aberration correction methods. This threshold was defined as the driving system power required to initiate cavitation with a 50% probability [25]. To find the cavitation threshold power, the histotripsy array was pulsed at 1-Hz PRF at a driving system power well below the cavitation threshold for each method, i.e., a point at which no

cavitation was observed. The high-voltage power supply that powered the pulser was then increased in increments of 1 Volt, and 30 images were acquired at each increment with the same high-speed optical imaging setup from Experiment 1. The camera shutter was opened 50 μs prior to the arrival of the histotripsy pulse at the focus and was left open for 1 ms. The LED backlight was then triggered for each histotripsy pulse at the time corresponding to the time of maximum bubble expansion, which was determined prior to the experiment. The power was increased until cavitation was observed on all 30 frames. The percentage of frames that included cavitation in the focus for each frame was treated as the probability for cavitation at each threshold [52]. A sigmoid curve given by

$$\boldsymbol{v(t) = \frac{\alpha}{1+e^{-\beta t}}} \textbf{ (E5.5)}$$

was then fit to the cavitation probabilities at each power level with α and β being fitting parameters. The 50% probability level on the curve was determined to be the cavitation threshold [53]. Cavitation power thresholds of all aberration correction methods were reported as a percentage of the cavitation power threshold through the aberrator without aberration correction.

5.2.3.4 Acrylic Disk Testing

To test the effectiveness of our histotripsy receiver system and ACE aberration correction algorithm to correctly identify phase aberrations across the array, two polymethyl methacrylate (acrylic) discs (McMaster-Carr Supply Company, Aurora, OH, USA) were placed between the histotripsy array and the focus covering approximately 30% of the elements in the array. The discs were 6.35 mm in thickness with diameters of 152.4 mm (disc A) and 101.6 mm (disc B). With an

estimated sound speed of 2700 m/s [54, 55], we anticipated a phase shift of approximately one cycle for the covered elements. Bubble clouds were generated with maximum power, and ACE expansion shockwave signals were acquired on the histotripsy array. Phases acquired from the ACE aberration correction method were subtracted from the free-field ACE aberration correction method phases acquired using bubble clouds generated with the same pressure to identify the total phase shift on each element due solely to the acrylic discs. These phases were then projected onto a rendering of the histotripsy array to visualize the areas of aberration.

5.2.3.5 Ex Vivo Porcine Abdominal Tissue Testing

Both aberration correction techniques were tested on four *ex vivo* porcine tissue samples. Tissue was acquired from four pigs that were a part of a separate, unrelated study approved by the University of Michigan Institutional Animal Care and Use Committee. Tissue was acquired from the entire middle abdominal region of the pigs laterally to the transverse processes of the lumbar vertebrae. These samples consisted of tissue from the complete abdominal wall including skin, subcutaneous fat, muscle, connective tissue, and the peritoneum. No internal organs were included in these tissue samples. Samples ranged between 25-50 mm in thickness throughout each sample and were approximately 200 mm in length and width. Samples were placed directly on a thin sheet of flexible plastic that was fixed in the water tank just above the histotripsy array such that the samples rested directly in the aberrator region shown in Figure 5.1A. For each sample, tissue impeded the paths between all elements of the histotripsy array and the focus. All tissue samples were harvested immediately after the pigs were sacrificed and used within three days of harvest. Samples were refrigerated and stored in 0.9% sodium chloride solution, USP (Baxter Healthcare Corporation, Deerfield, IL, USA), prior to experiments.

5.2.4 Experiment 3 – Spatial Variation of Phase Aberration and Attenuation in Ex Vivo Porcine Abdominal Tissue (From discussion of paper)

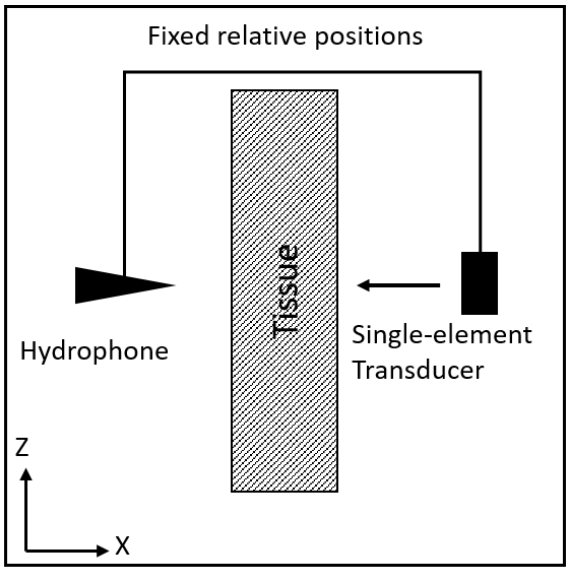

Figure 5.2: Experimental setup for measuring spatial variation of soft-tissue induced ultrasonic aberration and attenuation due to absorption and scattering via transmission A-line imaging. Setup included a low-frequency calibrated hydrophone that was co-axially aligned with and rigidly fixed to a single-element histotripsy transducer

Due to the acoustic absorption and scattering intrinsic to tissue, it is impossible to recover all lost focal pressure via phase AC. However, it is important to understand to what extend the focal pressure can be recovered via phase AC to determine the effectiveness of our AC algorithms. To briefly test the maximum possible recovery for phase AC under this particular experimental setup, one element from the histotripsy array was removed from the array scaffold and co-axially aligned with the hydrophone at a distance of approximately 15 cm. One sample of porcine abdominal tissue was placed between the single histotripsy element and the hydrophone, as shown in Figure 5.2. The hydrophone and histotripsy element were then scanned over a 40x40-mm grid with 1-mm spacing using an automated positioner, and an average of 30 pulses were acquired at each location. The same scan was also performed in the absence of tissue. The two scans were then

compared to determine both the variation of pulse arrival time (i.e., phase) and pressure measured by the hydrophone across the sample.

5.3. Results

5.3.1 Experiment 1 – Investigation of the Acoustic Cavitation Emission

5.3.1.1 Hydrophone Investigation

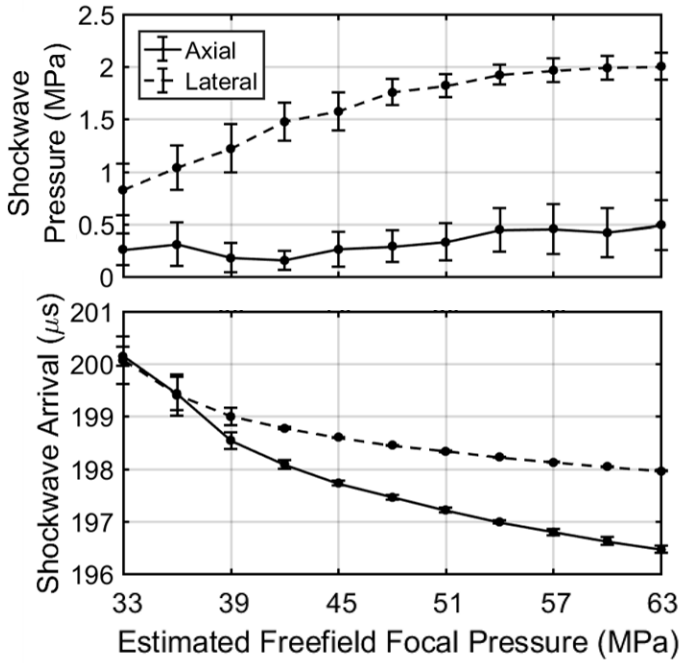

Figure 5.3: Shockwave pressure (top) and arrival time (bottom) along the axial (0°) and lateral (90°) axes of the array measured with a low-frequency calibrated hydrophone. Shockwave pressure increased significantly with increasing focal pressure along the lateral direction but not along the axial direction. The shockwaves arrived at the hydrophone increasingly earlier with increasing focal pressure along both the axial and lateral directions. The shockwave arrival time also increased in consistency from pulse-to-pulse with increasing focal pressure.

ACE expansion shockwaves generated across a range of transducer power levels were acquired via hydrophone to investigate their dependence on focal pressure. Mean ACE expansion shockwave pressures and arrival times acquired via hydrophone at the axial and lateral positions approximately 15-cm from the focus over a range of estimated free-field focal pressures are shown in Figure 5.3. At the axial position, the shockwave pressure was measured between approximately

0.25 and 0.5 MPa between estimated focal pressures of 33 and 63 MPa. At the lateral position, the shockwave amplitude started at approximately 0.8 MPa at the lowest tested focal pressure of 33 MPa and increased linearly to approximately 1.8 MPa at a focal pressure of 48 MPa. Increasing the focal pressure above this point resulted in moderate, logarithmic increases in shockwave pressure, which appeared to reach a saturation pressure of 2 MPa at a histotripsy focal pressure of 63 MPa. This indicates that increasing the focal pressure results in a compounding effect on shockwave pressure that does not occur in the axial direction.

At low amplitude, the shockwave arrival times on the hydrophone at both the axial and lateral positions were recorded at 200±0.2 μs, which is the round-trip travel time between the array elements and the focus. With increasing focal pressure and therefore increasing bubble cloud size, both hydrophone locations exhibited a decrease in arrival time of the first shockwave front. These results indicate outward growth of the portion of the bubble cloud that generates the front-edge shockwave. The axial position exhibited a larger decrease in shockwave arrival time totaling approximately 3.5 μs at a focal pressure of 63 MPa, while the lateral position exhibited a total shift of 2 μs at the same focal pressure. This is due to the larger size increase of the cavitation cloud in the axial direction than the lateral direction.

5.3.1.2 Optical Investigation

Bubble cloud shockwaves were investigated optically to analyze their spatial variations at all angles between the axial and lateral directions. Shadowgraph images of single-bubble, multi-bubble, and full-sized bubble cloud events are shown in Figure 5.4A, B, and C, respectively. In all panels, histotripsy pulses were transmitted from below the frame with the axis of the array aligned with the center of the bubble clouds. In Figure 5.4A, a single-cycle shockwave emitted by the

expansion of a single inertial cavitation bubble is observed and appears to be perfectly circular indicating that the bubble emitted a spherical shockwave during its initial expansion. The remainder of the histotripsy pulse propagating past the focus is observable as low frequency oscillations in the background of the frame. In the multi-bubble case (Figure 5.4B), which appears to include approximately 10-20 cavitation bubbles in a well-confined region, there are approximately 10-20 circular shockwaves surrounding the bubble cloud. However, the shockwaves are not co-aligned to one central location. The first arrival of the shockwave front to the array element location is consistently from the outer-most bubble (closest to the histotripsy array). Furthermore, the distance between the inner-most (closest to the bubble cloud) and front-edge shockwaves is larger in the axial direction than the lateral direction. In the robust bubble

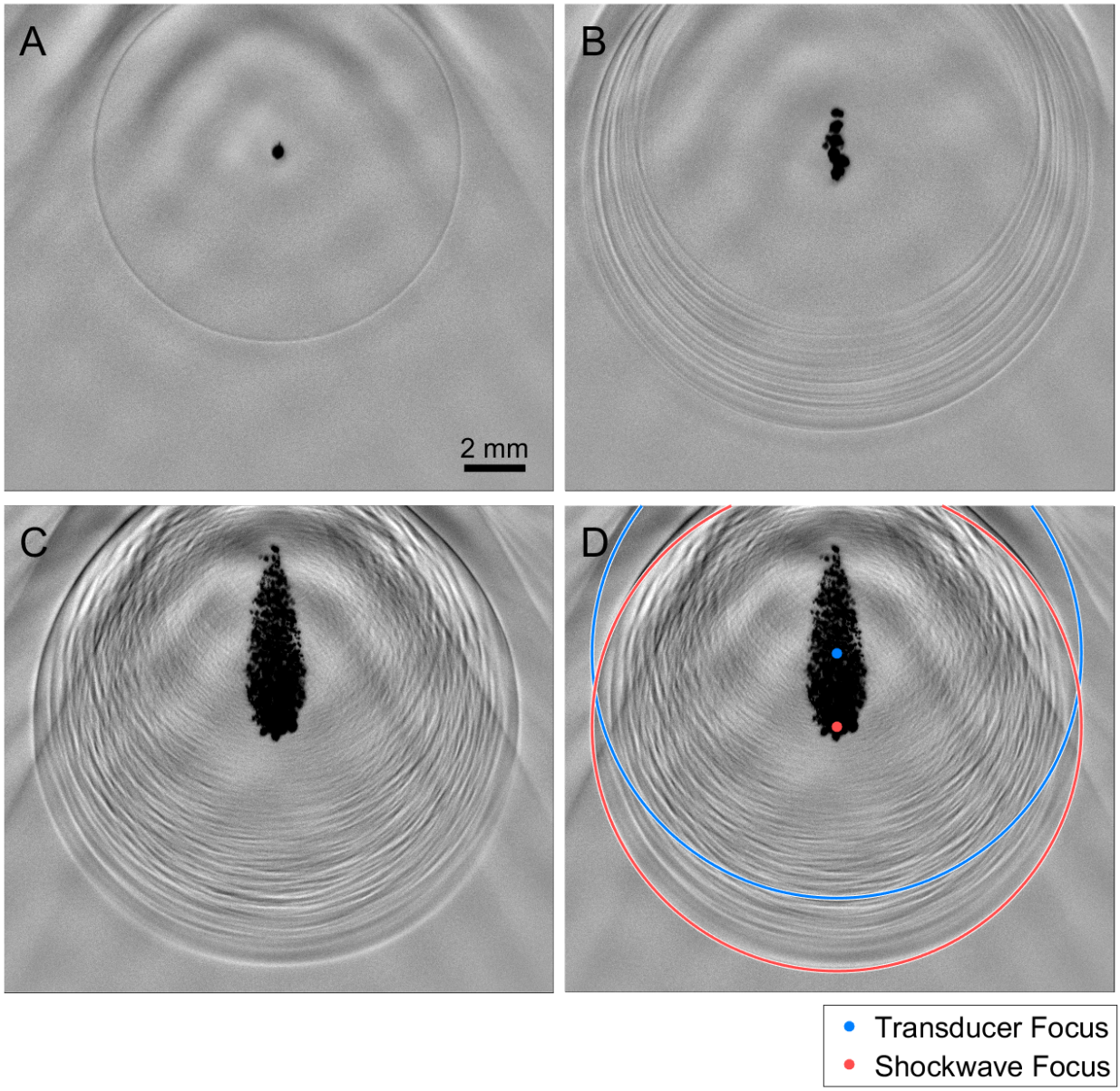

Figure 5.4: Representative shadowgraph images of histotripsy-induced (A) single-bubble (28 MPa P-), (B), multi-bubble (30 MPa P-), and (C) robust bubble clouds (63 MPa P-) in the free-field with no pre-focal aberration medium. Single-cycle shockwaves released by the expansion of cavitation bubbles are shown as circular rings centered about the cavitation bubble that generated them. In the single-bubble case, only one shockwave is visible. (D) A ring centered about the transducer focus (blue) at the radius of the front edge of the expansion shockwaves and a ring centered about the estimated focus of the front edge of the expansion shockwave (red) are overlaid onto the robust bubble cloud shadowgraph image in (C).

cloud case (Figure 5.4C), which includes hundreds to thousands of bubbles densely packed into a confined area, a complex, layered shockwave construct surrounds the bubble cloud. The front-

edge shockwave is not centered about the center of the bubble cloud, which is also the geometric center (focus) of the histotripsy array. Instead, it appears to be centered about the lowest portion of the bubble cloud (the portion closest to the histotripsy array). A high-speed video that captures the development of the bubble cloud in Figure 5.4C and resulting shockwave construct is available in the online edition of this manuscript. In Figure 5.4D, a blue circle indicates the expected location of the shockwave from Figure 5.4C at this time point if the shockwave was emitted from the focus of the array. The actual location of the front-edge of the shockwave construct is fit with a red circle with the center of that circle is also indicated in red. In this panel, it is clear that the front edge of the shockwave construct appears to have been emitted from the frontal region of the bubble cloud with an axial shift of approximately 2.5 mm from the geometric focus. The layers of shockwaves following in the wake of the front-edge shockwave vary continuously between the axial and lateral axes of the array indicating that highly varied signals are expected to be acquired by the elements of the histotripsy array after the signal generated by the front-edge shockwave. These results corroborate the hydrophone results and indicate that shockwave arrival times for larger bubble clouds correspond to an emission from the outer-most bubbles closest to the histotripsy array.

Shadowgraph images were then quantitatively analyzed. The location of the front-edge of the bubble cloud shockwaves acquired from shadowgraph images of 15 bubble clouds for single-bubble, multi-bubble, and full-sized bubble cloud events are shown in Figure 5.5. Distances between the geometric focus of the array and the front-edge of the shockwave construct were normalized relative to the lateral axis such that the lateral portion of the shockwave was at a distance of 0 mm. This was done to allow for a more direct comparison of shockwave distances between the different bubble cloud sizes. For single bubbles, no significant difference ($p=0.992$) in shockwave distance relative to the 90° axis of the array was observed across all angles measured.

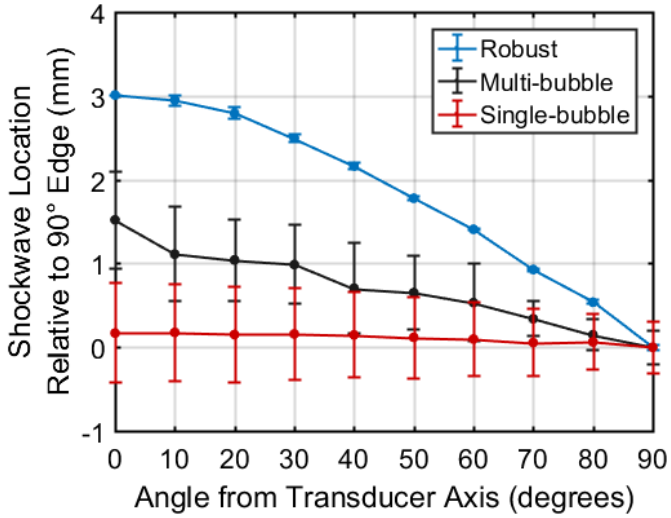

Figure 5.5: Optically measured location of the front edge of the cavitation expansion shockwave relative to the 90° axis of the histotripsy transducer. Single-bubble cavitation exhibited no significant change in shockwave edge across all measured angles but also exhibited high standard deviation due to inconsistency of the location of cavitation initiation. The multi-bubble cloud exhibited slight increase in shockwave front edge location and with increasing angle from transducer axis but also exhibited relatively high standard deviation across all angles. The robust (63 MPa P-) histotripsy cloud exhibited significant increase in shockwave edge distance with decreasing angle from axial direction of the transducer also exhibited very low standard deviation of shockwave location across all angles.

However, all angles exhibited a high standard deviation of shockwave distance at each angle (≥0.31 mm). This was due to the fact that the single bubbles were rarely initiated at exactly the same location. Rather, they were initiated randomly in a small region near the focus (approximately ±0.5 mm axially and laterally) thus resulting in inconsistent shockwave locations. For the multi-bubble clouds, the front-edge of the shockwave was measured to be approximately 1.5 mm farther from the array focus at the 0° axis than the 90° axis indicating a pre-focal shift of the front edge of the shockwave construct. However, all angles still exhibited a relatively high standard deviation (≥0.19 mm). No neighboring angle measurements, e.g., 0° vs 10°, exhibited significant difference in shockwave distance ($p>0.972$). For the large cloud, the shockwave location exhibited a 3-mm difference between the 0° and 90° axes and decreased linearly between 20° and 60°. The standard deviation of the shockwave location was relatively small (≤0.07 mm)

across all measured angles for the large bubble cloud. In the case of the robust bubble cloud, shockwave formation was highly consistent and resulted in nearly identical front-edge shockwave propagation from one cloud to the next. Importantly, a significant difference in shockwave arrival time was observed between all angles ($p<0.001$) thus indicating that each ring of the histotripsy array is expected to exhibit a significant difference in arrival time between all rings.

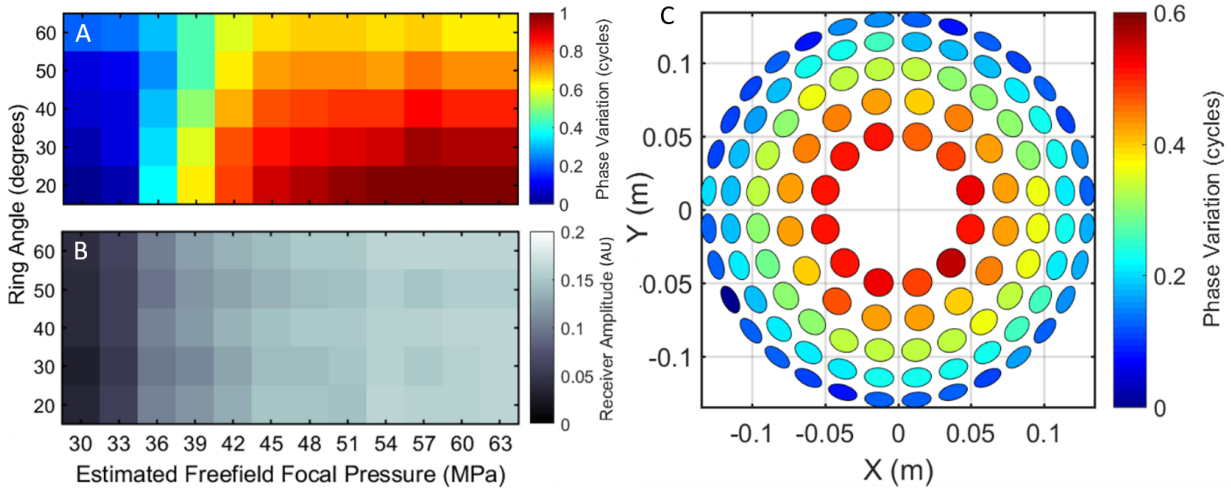

Figure 5.6: Free-field histotripsy receiver phase variation (A) and amplitude (B) across rings at varying histotripsy focal pressures. Receiver amplitude increased linearly across all rings of the histotripsy array with increasing focal pressure, but shockwave arrival increased non-linearly with increasing focal pressure with upwards of a half-wavelength difference between the outer- and inner-most rings at the highest focal pressure. Phase differences in shockwave arrival (generated with a 63 MPa focal pressure bubble cloud) are projected onto a rendering of the histotripsy array (C). Each ring exhibited low phase variance indicating a pre-focal shift of origin of the front edge of the shockwave.

5.3.1.3 Receive-Capable Histotripsy Array Investigation Results

Bubble cloud shockwaves were measured with the histotripsy array to confirm the hydrophone and optical shockwave investigations. Shockwave phase variations measured with the receive-capable histotripsy array for estimated free-field focal pressures between 30 and 63 MPa are shown in Figure 5.6A. For reference, a full one-cycle phase shift equals a 2-us temporal shift

in water at 500 kHz. The receiver indicated that shockwave phases increased on all array elements with increasing focal pressure (i.e., the shockwaves arrived earlier). However, this increase was nonlinearly correlated between elements on different rings of the array, and the elements in the inner-most ring exhibited the largest phase increases. No differences in arrival time were observed between elements within the same ring for all focal pressures. For focal pressures at and above 48 MPa, the mean phases of each ring of the array were significantly different from all other rings ($p<0.001$). This is due to the fact that the shockwave front is formed by the outer-most bubbles that are closest to the array, and the elliptical-shaped cavitation cloud has a larger width in the axial direction than the lateral direction.

Shockwave peak-positive amplitude variations measured with the array at estimated focal pressures between 30 and 63 MPa are shown in Figure 5.6B. The receiver amplitude was found to increase linearly across all elements of the array with the highest receive amplitudes at the highest free-field focal pressure of 63 MPa. At any given focal pressure, the shockwave amplitude differences between all array elements were insignificant. This indicates that shockwave signal intensity is expected to be the same on all elements of the array at any focal pressure.

To visualize the phase variation across the array at high focal pressures, the phase data from the 63 MPa estimated focal pressure bubble cloud data in Figure 5.6A is projected onto a rendering of the array in Figure 5.6C. The mean shift across all elements in each ring at this pressure level was found to be 0.51±0.03, 0.43±0.02, 0.33±0.02, 0.21±0.03, and 0.12±0.04 cycles for rings one (20°) through five (60°), respectively. This further supports the notion that the shockwaves from bubble clouds generated at higher focal pressures are emitted from a pre-focal location without much shift in the transverse plane.

5.3.2 Experiment 2 – Aberration Correction Testing

5.3.2.1 Acrylic Disk Testing

The ability of the receive-capable histotripsy array and ACE aberration correction algorithm to accurately detect phase aberrations was first tested by placing two acrylic discs aberrators between the array and the focus covering approximately 30% of the elements. The acrylic discs were expected to result in a phase shift of approximately 1 cycle for covered elements with normal incidence with the discs. The phase shifts of the ACE expansion shockwaves due to the discs are projected onto a rendering of the histotripsy array in Figure 5.7. The mean phase shift of the elements covered by the discs was 1.04 ± 0.2 cycles with a median of 1.13 cycles. No completely uncovered elements exhibited a significant change in phase. These results indicate that the receiver system can accurately measure phase aberrations.

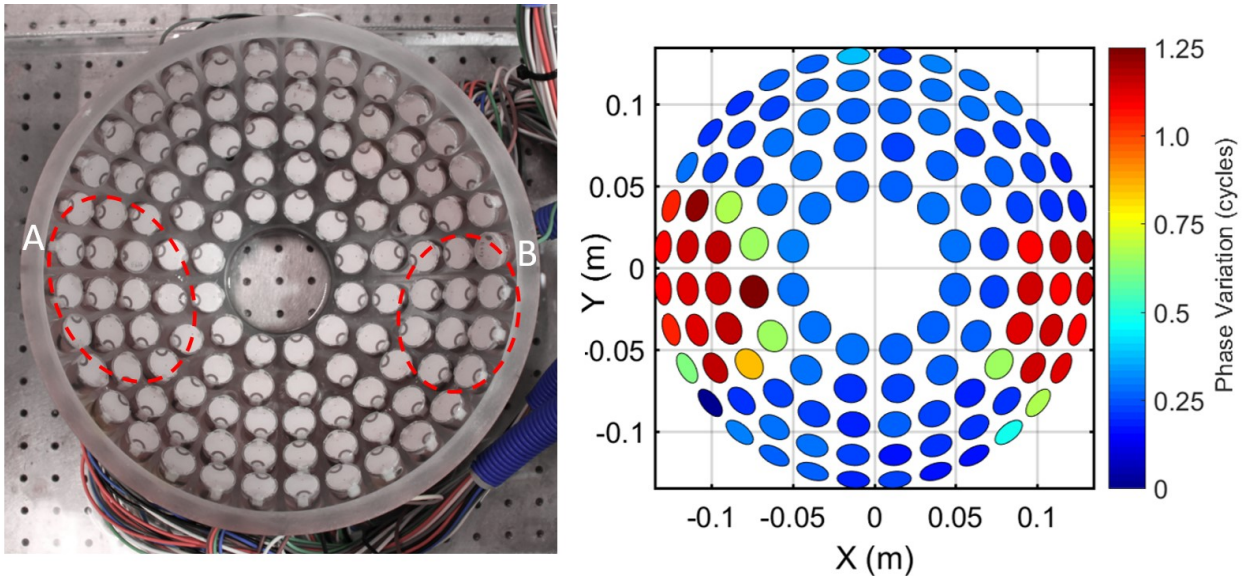

Figure 5.7: Picture of histotripsy array (left) with areas covered by acrylic discs outlined and phase projection (right) of ACE emission signal arrival time difference between disk phantom and free field measurements illustrating the resulting phase aberration. Both disc phantoms were circular with a thickness of 6.35 mm. Diameters of discs A and B were 152.4 mm and 101.6 mm, respectively.

5.3.2.2 Ex Vivo Porcine Abdominal Tissue Testing

Both aberration correction methods were then tested using four porcine abdominal tissue samples. The average maximum phase shift across all tissue samples was 1.5 ± 0.16 cycles for both AC methods. Both aberration correction methods resulted in significant increases in focal pressure through the porcine tissue using the same transducer driving power compared to the focal pressure without aberration correction. Focal pressures and the percent pressure recovered with each aberration correction method, given by (4), are summarized in Table I. In the absence of tissue or any other aberrating medium, the array produced a peak-to-peak focal pressure of 2.19 MPa when tested at a sub-cavitation threshold array power level. At the same power level, this pressure level dropped to 1.09 ± 0.05 MPa in the presence of tissue, a reduction of approximately 50%. Using the hydrophone aberration correction method, the focal pressure recovered to 1.70 ± 0.10 MPa recovering approximately 55% of the lost pressure. When using the ACE-based aberration correction method, the focal pressure was found to be 1.32 ± 0.03, which corresponds to a pressure recovery of approximately 21%. Beam profiles (Figure 5.8) tested at the same focal

Table 5.1: Focal Pressures Through Tissue

Treatment method	Focal Pressure (MPa)	% Recovered
Baseline pressure without tissue[a]	2.19	100.00%
No Aberration Correction	1.09 ± 0.05	0.00%
With Hydrophone AC	1.70 ± 0.10	55.50%
With ACE AC	1.32 ± 0.03	20.90%

[a]Pressure at the focus of the histotripsy array aligned with the hydrophone method in the free-field without any pre-focal aberration medium

Table 5.2: Percent of Power Required to Induce Cavitation Through Tissue Aberrators

Without Aberration Correction	100%
Hydrophone	49.8 ± 6.8%
ACE	68.5 ± 12.9%
Free-field baseline power[a]	33.20%

[a]Power required to induce cavitation in the free-field without pre-focal aberration media relative to average power required to induce cavitation through tissue without aberration correction

pressure level indicated that the ACE aberration correction method shifted the focus to a pre-focal location by 2-3 mm. Little to no shift in the x- and y-directions was observed.

The electric power input to the array required to generate cavitation was recorded for the case with the tissue aberrator in place for 1) without aberration correction, 2) using hydrophone aberration correction, and 3) with ACE aberration correction (Table II). The hydrophone and ACE methods both resulted in a statistically significant decreases in cavitation threshold power through the porcine tissue compared to that without aberration correction ($p<0.001$, $p=0.007$, respectively). The array power required to generate cavitation without aberration correction was normalized and

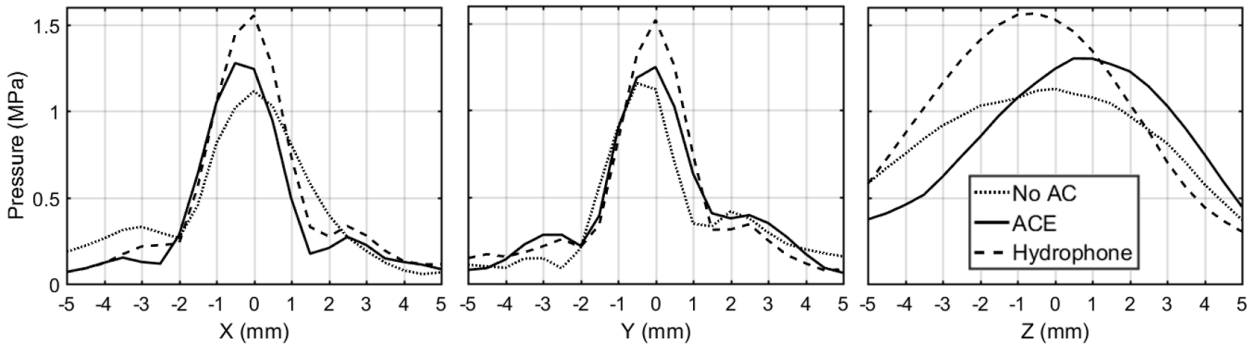

Figure 5.8: Sub-cavitation threshold beam profiles in x-, y-, and z-directions with no aberration correction (AC), ACE AC, and hydrophone AC acquired through one tissue sample acquired with a low-frequency calibrated hydrophone.

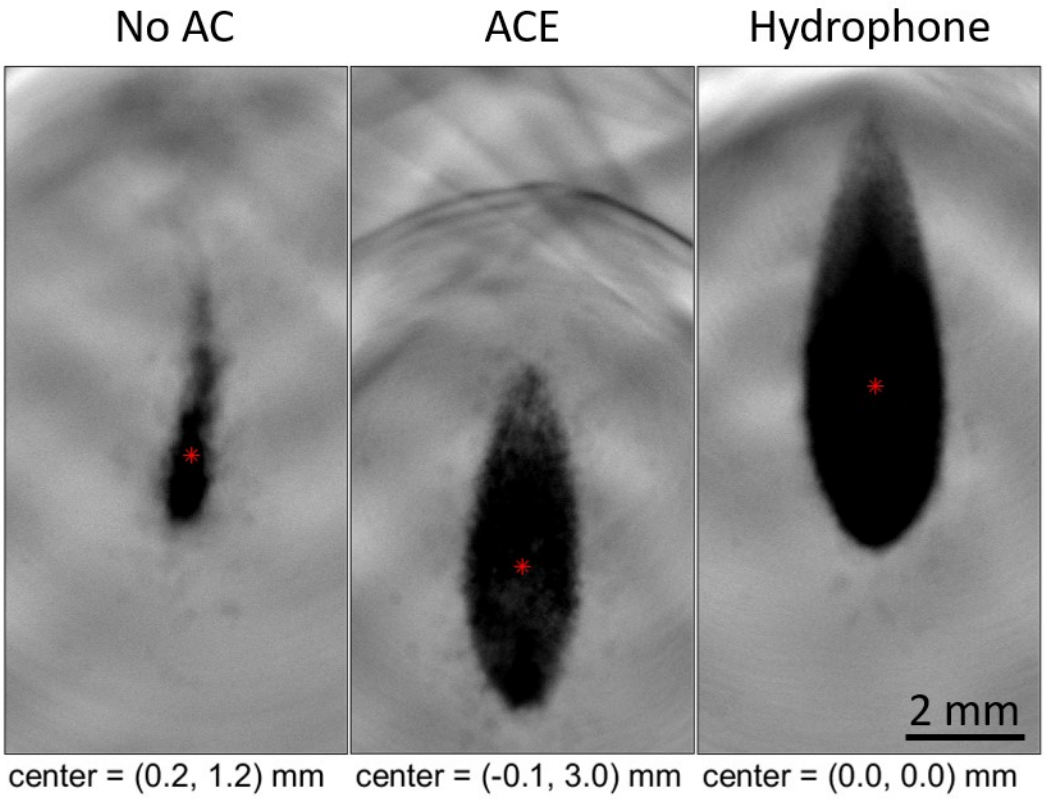

Figure 5.9: Average of 30 images of bubble clouds generated through one tissue sample at an estimated free-field P- pressure of 63 MPa using no aberration correction (AC), ACE AC, hydrophone AC. Bubble cloud foci are shown in red and are relative to the hydrophone-aligned bubble cloud center. The ACE-aligned bubble cloud exhibited a 3-mm pre-focal shift. Both aberration correction methods resulted in significantly larger bubble clouds than the unaligned treatment with the hydrophone method producing the largest, followed by ACE.

referred to as 100% power. The hydrophone method reduced the cavitation threshold power to approximately 49.8% while the ACE method reduced this threshold to approximately 68.5%. For comparison, in the absence of tissue, cavitation threshold power was 33.2% relative to the normalized 100% power with tissue and no aberration correction. Therefore, since the hydrophone aberration correction reduced the threshold power to approximately 50%, a majority of the increase in cavitation threshold through tissue was due to phase aberrations and not scattering or absorption.

Representative average bubble cloud images generated through a tissue aberrator are shown in Figure 5.9 for 1) without aberration correction, 2) using hydrophone aberration

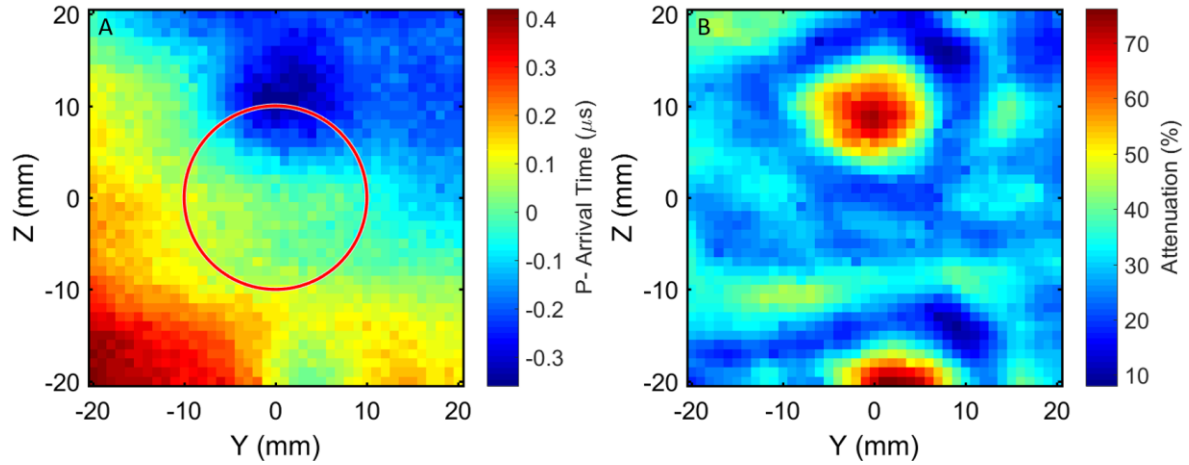

Figure 5.10: The hydrophone-transducer construct was scanned over a 40x40-mm area using an automated positioning system. The resulting raster scan image (B) indicates significant variation in sound speed across this area. The red circle indicates the size of one 20-mm histotripsy element from the 112-element array used in this study. When compared to the same measurements in the absence of tissue, the acoustic attenuation across this section of tissue (C) was found to vary between approximately 10-75%.

correction, and 3) with ACE aberration correction. Using the same electric power to drive the histotripsy array, the cavitation clouds generated without aberration correction were observed to be much smaller than the cavitation clouds generated using hydrophone and ACE aberration correction methods. This difference is due to the lower pressure and defocusing without aberration correction. The cavitation cloud generated after aberration correction using the hydrophone and ACE methods were more characteristic of a bubble cloud formed in the free-field (e.g., Figure 5.4C). However, the cavitation clouds generated by ACE aberration correction exhibited a pre-focal shift of approximately 3 mm.

5.3.3 Experiment 3 – Spatial Variation of Phase Aberration and Attenuation in Ex Vivo Porcine Abdominal Tissue

Arrival times of the P- portion of the average pulse from the single element at each location are shown in Figure 5.10A and are overlaid with a red circle indicating the size of one histotripsy

element. The percent acoustic attenuation at each location relative to the same measurements in the absence of tissue are shown in Figure 5.10B. From this preliminary experiment, we can see that there is close to a 1-μs worst-case difference in P- arrival time across the face of one 2-cm histotripsy element. The average percent attenuation shown in Figure 5.10B was found to be 30.6±10.3%. From the *ex vivo* porcine tissue AC testing in Experiment 2, it was found that the focal pressure through tissue using the hydrophone-based aberration correction (1.70±0.1 MPa) exhibited approximately a 22% attenuation from the freefield measurement (2.19 MPa). These data therefore indicate that the majority of remaining pressure loss after hydrophone-based aberration correction is likely due purely to attenuation due to absorption and scattering rather than phase aberration due to sound speed variations.

5.4. Discussion

In this study, we developed and tested the first receive-capable histotripsy array to measure shockwaves emitted by the initial expansion of inertially cavitating bubbles generated by histotripsy to correct for phase aberrations due to ultrasound propagation through heterogeneous tissue without additional imaging equipment such as secondary ultrasound images, CT, or MRI. Furthermore, rather than simply receiving reflections of ultrasound from pre-existing bubbles or point scatterers, the array in this study was used to generate a point-source construct of shockwaves at a specific location that were received and analyzed for aberration correction. These techniques could potentially be used for all cavitation-based ultrasonic therapies including histotripsy.

Experiment 1 revealed that the front edge of the ACE signal originates from the bubbles of the cavitation cloud closest to the transducer rather than the geometric focus of the histotripsy array when initiating a robust bubble cloud. This result supports previous findings that the source of the acoustic emission from the bubble cloud is due to emitted shockwaves [31]. This phenomenon is

important for bubble cloud localization and aberration correction, as the arrival time of shockwave to each element of the histotripsy array is determined by the distance between these cavitation bubbles and each element. Although it can be expected that the front edge of the shockwave construct will be emitted prefocally, it is difficult to estimate the extent of this shift (i.e., size of the cavitation cloud) without optical imaging. A single bubble would be the ideal point source for aberration correction. However, Experiment 1 shows that the location of the single bubble generation is not consistently at the geometrical focus of the histotripsy array, and the shockwave amplitude from the single bubble emission is low. Therefore, the benefit of using a robust bubble cloud is that the central location of shockwave formation is more consistent from one cloud to the next as opposed to the single bubbles. Another benefit of using a robust bubble cloud is that higher pressure shockwaves are emitted and are thus more easily detected through tissue. We hypothesize that the higher pressure is due to a layering effect of shockwaves that only occurs at non-axial locations. Due to the nature of the formation of the bubble cloud, the front-edge shockwave appears to experience constructive interference in the non-axial direction that increases the overall amplitude as more shockwaves are generated with more bubbles. Therefore, a robust cavitation cloud is used for ACE aberration correction for this study.

In Experiment 2, using robust bubble clouds, we hypothesized that the front edge of the shockwave construct can be used as a point source for aberration correction through soft tissue aberrators by calculating a phase correction using a receive-capable histotripsy system. Results showed significant pressure loss was induced by the 2.5- to 5-cm thick, multi-layered soft tissue aberrators. The phase aberrations appear to have a larger impact on histotripsy focal pressure than attenuation due to absorption and scattering because the hydrophone method was able to recover approximately 55% of the lost pressure in the linear regime. By correcting the phase aberrations,

we were able to regain a significant amount of pressure and significantly reduce the overall power required to induce cavitation.

The ACE method recovered approximately 21% of the lost pressure in the linear regime. This demonstrates the proof-of-concept method of using cavitation shockwaves and a receive-capable histotripsy array for aberration correction, but the regained pressure was much less compared to the hydrophone method. We hypothesized that the primary reason for this discrepancy is due to the size of the elements in this histotripsy array. The aperture of the hydrophone used in this study was 85 μm in diameter while each histotripsy element was 2 cm in diameter. Therefore, because tissue sound speed may vary significantly over a small area, the hydrophone should allow for a much finer resolution correction. This hypothesis was tested in Experiment 3. It was found that the phase variation across the face of one histotripsy element could be upwards of 1-μs (Figure 5.10A). The 1-μs difference could erroneously put a 500-kHz histotripsy element completely out of phase. Furthermore, this effect could worsen *in vivo* with more overlying tissue and less consistent surface geometries. While it appears that, in general, the phase aberration changes gradually across tissue, this effect will likely worsen *in vivo* when there is even more overlying tissue. Therefore, smaller elements are likely to drastically improve the abilities to use the ACE method for aberration correction. The average percent attenuation shown in Figure 5.10B was found to be approximately 30% under normal incidence depending on the location. These data, in conjunction with the data from Experiment 2, support the notion that the hydrophone-based aberration correction method recovered virtually all of the attenuation due to phase aberration with the remainder being due to absorption and scattering. Therefore, the hydrophone-based method acts as a suitable gold-standard against which to compare the ACE-based aberration correction.

While the estimated P- focal pressure for the robust bubble clouds was reported to be 63 MPa, this is likely an over-estimation of the actual focal pressure with pre-focal tissue aberrators. This pressure was used to cover the range of cavitation events that can be used for aberration correction, but this high level of pressure used to generate a large, dense bubble cloud, is not necessary to perform the proposed ACE aberration correction. The results in this study suggest that the most important feature of the bubble clouds used for ACE aberration correction is that they are consistent from one cloud to the next, thus emitting consistent shockwaves.

When used *in vivo* where severe phase aberrations occur resulting in poorly formed bubble clouds, this method may reduce treatment times and improve the range of electronic focal steering [56] thereby increasing the ability of histotripsy to treat larger and deeper targets. The reduction in array power to initiate cavitation is also important for reducing unwanted tissue heating.

The ACE aberration correction method resulted in a pre-focally generated bubble cloud. For the majority of histotripsy therapies, this is not a problem as the desired treatment volume typically consists of 1000 or more treatment locations. Therefore, treating a 2-3 mm boundary around a target area, e.g., a liver tumor, would likely not introduce any major complication. However, for histotripsy therapies that require very high precision, e.g., thrombolysis or brain therapies, one potential solution to get a better estimation of pre-focal shockwave formation could be to use a B-mode ultrasound imager to estimate the bubble cloud size. This could then be used to apply a more appropriate phase calibration to shift the ACE-corrected bubble cloud back to the focus. Another option for bubble cloud refocusing is to subtract the phase delays that would be used to steer the array prefocally. Since this method would only apply an axial shift, it may over-generalize the phase correction on the array thus reducing focal pressure and bubble cloud size.

However, it would likely increase the accuracy of bubble cloud placement. These methods and others will be explored in future studies.

A different method for reducing the effects of the pre-focal shockwave formation is to use the shockwave from a single bubble as a point source for aberration correction rather than a large bubble cloud. Currently, this potential method has two problems. First, as shown in Figure 5.5, when the histotripsy array is fired at the cavitation threshold where a single bubble is only formed approximately 50% of the time, the bubble tends to move about the focus substantially (~±0.5 mm). While this motion is bounded to within the dimensions of the transducer focus, this results in an inconsistent formation of the shockwave making it difficult to correct to one specific location. Second, the pressure of the single-bubble shockwave was found to be less than half the pressure of the shockwave emitted by the large bubble cloud. Due to attenuation in the tissue, single-bubble shockwaves were nearly impossible to detect with our current array hardware. These issues could be solved via hardware improvements and more advanced signal processing methods, which will both be explored in future studies.

5.5. Conclusions

This study demonstrated that the shockwaves generated by the initial expansion of inertially cavitating microbubbles received by a histotripsy array can be used for the ACE aberration correction. It was found that phase aberration induces significant reduction of histotripsy focal pressure. These results show that the ACE aberration correction method can be used for phase aberration correction to recover substantial pressure loss for histotripsy through soft-tissue.

5.6. References

[1] J. Macoskey, T. Hall, J. Sukovich, S. Choi, K. Ives, E. Johnsen, C. Cain and Z. Xu, "Soft-Tissue Aberration Correction for Histotripsy," *IEEE Transactions on Ultrasonics, Ferroelectrics, and Frequency Control,* vol. 65, no. 11, pp. 2073-85, 2018.

[2] F. Fry and J. Barger, "Acoustic properties of the human skull," *J. Acoust. Soc. Am.,* vol. 63, no. 5, pp. 1576-90, 1978.

[3] S. Flax and M. O'Donnell, "Phase-aberration correction using signals from point reflectors and diffuse scatterers: basic principles," *IEEE Trans. Ultrason., Ferroelect., Freq. Control,* vol. 35, no. 6, pp. 758-67, 1988.

[4] F. A. Duck, "Acoustic Properties of Tissue at Ultrasonic Frequencies," in *Physical Properties of Tissue: A Comprehensive Reference Book*, San Diego, CA, Academic Press Inc., 1990, pp. 73-135.

[5] K. Vortman and S. Vitek, "Tissue aberration corrections in ultrasound therapy". United States Patent 8,088,067, 2012.

[6] M. Pernot, J.-F. Aubry, M. Tanter, J.-L. Thomas and M. Fink, "High power transcranial beam steering for ultrasonic brain therapy," *Phys. Med. Biol.,* vol. 48, pp. 2577-89, 2003.

[7] M. Pernot, G. Montaldo, M. Tanter and M. Fink, ""Ultrasonic stars" for time-reversal focusing using induced cavitation bubbles," *Applied Physics Letters,* vol. 88, p. 034102, 2006.

[8] J. Sun and K. Hynynen, "Focusing of therapeutic ultrasound through a human skull: A numerical study," *J. Acoust. Soc. Am.,* vol. 104, no. 3, pp. 1705-15, 1998.

[9] J. Sun and K. Hynynen, "The potential of transskull ultrasound therapy and surgery using the maximum available skull surface area," *J. Acoust. Soc. Am.,* vol. 105, no. 4, pp. 2519-27, 1999.

[10] F. Marquet, M. Pernot, J.-F. Aubry, G. Montaldo, L. Marsac, M. Tanter and M. Fink, "Non-invasive transcranial ultrasound therapy based on a 3D CT scan: Protocol validation and in vitro results," *Phys. Med. Biol.,* vol. 54, pp. 2597-613, 2009.

[11] J.-F. Aubry, M. Tanter, M. Pernot, J.-L. Thomas and M. Fink, "Experimental demonstration of noninvasive transskull adaptive focusing based on prior computed tomography scans," *J. Acoust. Soc. Am.,* vol. 113, no. 1, pp. 84-93, 2003.

[12] D. Zhao and G. Trahey, "Comparisons of image quality factors for phase aberration correction with diffuse and point targets: Theory and experiments," *IEEE Trans. Ultrason. Ferroelect. Freq. Control,* vol. 38, no. 2, pp. 125-132, 1991.

[13] M. Fink, "Time reversal of ultrasonic fields - Part I: basic principles," *IEEE Trans. Ultrason. Ferroelect. Freq. Control,* vol. 39, no. 5, pp. 555-66, 1992.

[14] D.-L. Lui and R. Waag, "Correction of ultrasonic wavefront distortion using backpropagation and a reference waveform method for time-shift compensation," *J. Acoust. Soc. Am.,* vol. 96, no. 2, pp. 649-660, 1994.

[15] S. Krishnan, P.-C. Li and M. O'Donnell, "Adaptive compensation of phase and magnitude aberrations," *IEEE Trans. Ultrason. Ferroelect. Freq. Control,* vol. 43, no. 1, pp. 44-55, 1996.

[16] M. Tabei, T. Mast and R. Waag, "Simulation of ultrasonic focus aberration and correction through human tissue," *J. Acoust. Soc. Am.,* vol. 113, no. 2, pp. 1166-76, 2003.

[17] R. Apfel and C. Holland, "Gauging the likelihood of cavitation from short-pulse, low-duty cycle diagnostic ultrasound," *Ultrasound Med. Biol.,* vol. 17, no. 2, pp. 179-85, 1991.

[18] M. Gyöngy, M. Arora, J. A. Noble and C. C. Coussios, "Use of Passive Arrays for Characterization and Mapping of Cavitation Activity during HIFU Exposure," Beijing, 2008.

[19] O. Kripfgans, J. Fowlkes, M. Woydt, O. Eldevik and P. Carson, "In vivo droplet vaporization for occlusion therapy and phase aberration correction," *IEEE Trans. Ultrason., Ferroelect., Freq. Control,* vol. 49, no. 6, pp. 726-36, 2002.

[20] K. Haworth, J. Fowlkes, P. Carson and O. Kripfgans, "Towards aberration correction of transcranial ultrasound using acoustic droplet vaporization," *Ultrasound Med. Biol.,* vol. 34, no. 3, pp. 435-45, 2008.

[21] Z. Xu, A. Ludomirsky, L. Y. Eun, T. L. Hall, B. C. Tran, B. J. Fowlkes and C. A. Cain, "Controlled Ultrasound Tissue Erosion," *IEEE Trans. Ultrason., Ferroelect., Freq. Control,* vol. 51, no. 6, pp. 726-736, June 2004.

[22] W. Roberts, T. Hall, K. Ives, J. Wolf Jr., J. Fowlkes and C. Cain, "Pulse cavitational ultrasound: A noninvasive technology for controlled tissue ablation (histotripsy)," *J. Urol.,* vol. 175, pp. 734-738, 2006.

[23] Z. Xu, T. Hall, J. B. Fowlkes and C. A. Cain, "Effects of acoustic parameters on bubble cloud dynamics in ultrasound tissue erosion (histotripsy)," *J. Acoust. Soc. Am.,* vol. 122, no. 1, pp. 229-236, July 2007.

[24] A. Maxwell, C. Cain, A. Duryea, L. Yuan, H. Gurm and Z. Xu, "Noninvasive thrombolysis using pulsed ultrasound cavitation therapy - histotripsy," *Ultrasound Med. Biol.,* vol. 35, no. 12, pp. 1982-94, 2009.

[25] A. Maxwell, C. Cain, T. Hall, J. Fowlkes and Z. Xu, "Probability of cavitation for single ultrasound pulses applied to tissues and tissue-mimicking materials," *Ultrasound Med. Biol.,* vol. 39, no. 3, pp. 449-65, 2013.

[26] K.-W. Lin, Y. Kim, A. D. Maxwell, T.-Y. Wang, T. L. Hall, Z. Xu, B. J. Fowlkes and C. A. Cain, "Histotripsy beyond the intrinsic cavitation threshold using very short ultrasound pulses: Microtripsy," *IEEE Trans. Ultrason., Ferroelect., Freq. Control,* vol. 61, no. 2, pp. 251-265, February 2014.

[27] T. Leighton, "The Forced Bubble," in *The Acoustic Bubble*, San Diego, Academic Press, Inc., 1994, pp. 287-438.

[28] T. Whittingham, F. Duck, Baker and S. H. AC, "The Purpose and Techniques of Acoustic Output Measurement," in *Ultrasound in Medicine*, Philadelphia, Institute of Physics Publishing, 1998, pp. 129-148.

[29] M. Plesset, "Shockwaves from cavity collapse," *Phil. Trans. Royal Soc. A,* vol. 260, no. 1110, pp. 241-244, 1966.

[30] M. Plesset and A. Prosperetti, "Bubbly Dynamics and Cavitation," *Ann. Rev. Fluid Mech.,* vol. 9, pp. 145-185, 1977.

[31] J. Sukovich, T. Hall, J. Macoskey, C. Cain and Z. Xu, "Investigation of the source of histotripsy acoustic backscatter signals," *Journ. Acoust. Soc. Am.,* vol. 141, p. 3551, 2017.

[32] J. Macoskey, S. Choi, T. Hall, E. Vlaisavljevich, J. Lundt, E. Johnsen, C. Cain and Z. Xu, "Using the cavitation collapse time to indicate the extent of histotripsy-induced tissue fractionation," *Phys. Med. Biol.,* vol. 63, p. 155013, 2018.

[33] Y. Kim, "Acoustic aberration in non-invasive histotripsy therapy," *Doctoral dissertation,* 2013.

[34] Y. Kim, T. Hall, Z. Xu and C. Cain, "Transcranial histotripsy therapy: A feasibility study," *IEEE Trans. Ultrason. Ferroelect. Freq. Control,* vol. 61, no. 4, pp. 582-93, 2014.

[35] H. Wang, E. Ebbini, M. O'Donnell and C. Cain, "Phase aberration correction and motion compensation for ultrasonic hyperthermia phased arrays: experimental results," *IEEE. Trans. Ultrason. Ferroelectr. Freq. Control,* vol. 41, no. 1, pp. 34-43, January 1994.

[36] R. Seip, P. VanBaren and E. Ebbini, "Dynamic focusing in ultrasound hyperthermia treatments using implantable hydrophone arrays," *IEEE Trans. Ultrason. Ferroelectr. Freq. Control,* vol. 41, no. 5, pp. 706-713, September 1994.

[37] T. Gerhardson, J. Sukovich, A. Pandey, T. Hall and C. Cain, "Catheter hydrophone aberration correction for transcranial histotripsy treatment of intracerebral hemorrhage: proof-of-concept," *IEEE Trans. Ultrason. Ferroelect. Freq. Control,* vol. 64, no. 11, pp. 1684-97, 2017.

[38] E. Vlaisavljevich, Y. Kim, S. Allen, G. Owens, S. Pelletier, C. Cain, K. Ives and Z. Xu, "Image-guided non-invasive ultrasound liver ablation using histotripsy: Feasibility study in an in vivo porcine model," *Ultrasound Med. Biol.,* vol. 39, pp. 1398-1409, 2013.

[39] J. Sukovich, Z. Xu, Y. Kim, T.-S. Nguyen, A. Pandey, T. Hall and C. Cain, "Targeted lesion generation through the skull without aberration correction using histotripsy," *IEEE Trans. Ultrason. Ferroelectr. Freq. Control,* vol. 63, no. 5, pp. 671-682, 2016.

[40] X. Zhang, J. Macoskey, K. Ives, G. Owens, H. Gurm, J. Shi, M. Pizzuto, C. CA and Z. Xu, "Non-Invasive Thrombolysis Using Microtripsy in a Porcine Deep Vein Thrombosis Model," *Ultrasound Med. Biol.,* vol. 43, no. 7, pp. 1378-90, 2017.

[41] T. Varslot and G. Taraldsen, "Computer simulation of forward wave propagation in soft tissue," *IEEE Trans. Ultrason. Ferroelect. Freq. Control,* vol. 52, no. 9, pp. 1473-82, 2005.

[42] U. Haberkorn, G. Layer, V. Rudat, I. Zuna, A. Lorenz and G. Kaick, "Ultrasound image properties influenced by abdominal wall thickness and composition," *J. Clin. Ultrasound,* vol. 21, pp. 423-9, 1993.

[43] L. Hinkelman, D.-L. Lui, L. Metlay and R. Waag, "Measurements of ultrasonic pulse arrival time and energy level variations produced by propagation through the abdominal wall," *J. Acoust. Soc. Am.,* vol. 95, no. 1, pp. 530-41, 1994.

[44] Y. Kim, E. Vlaisavljevich, G. Owens, S. Allen, C. Cain and Z. Xu, "In vivo transcostal histotripsy therapy without aberration correction," *Phys. Med. Biol.,* vol. 59, pp. 2553-68, 2014.

[45] A. Duryea, H. Tamaddoni, C. Cain and W. H. T. Roberts, "Removal of residual nuclei following a cavitation event: a parametric study," *IEEE Trans. Ultrason. Ferroelectr. Freq. Control,* vol. 62, no. 9, pp. 1605-1614, September 2015b.

[46] J. Parsons, C. Cain and G. F. J. Abrams, "Pulsed cavitational ultrasound therapy for controlled tissue homogenization," *Ultrasound Me. Biol.,* vol. 32, pp. 115-129, 2006a.

[47] E. Vlaisavljevich, T. Gerhardson, T. Hall and Z. Xu, "Effects of f-number on the histotripsy intrinsic threshold and cavitation bubble cloud behavior," *Phys. Med. Biol.,* vol. 62, pp. 1269-90, 2017.

[48] G. Settles, Schlieren and Shadowgraph Techniques: Visualizing Phenomena in Transparent Media, Berlin: Springer, 2012.

[49] M. Fink, "Time reversal of ultrasonic fields - part I: Basic principles," *IEEE Trans. Ultrason. Ferroelect. Freq. Control,* vol. 39, no. 5, pp. 555-66, 1992.

[50] L. Nock, G. Trahey and S. Smith, "Phase aberration correction in medical ultrasound using speckle brightness as a quality factor," *J. Acoust. Soc. Am.,* vol. 85, no. 5, pp. 1819-33, 1989.

[51] P. Freiburger and G. Trahey, "Parallel processing techniques for the speckle brightness phase aberration correction algorithm," *IEEE Trans. Ultrason., Ferroelect., Freq. Control,* vol. 44, no. 2, pp. 431-44, 1997.

[52] E. Vlaisavljevich, O. Aydin, K.-W. Lin, Y. Durmaz, J. Fowlkes, M. ElSayed and Z. Xu, "The role of positive and negative pressure on cavitation nucleation in nanodroplet-mediated histotripsy," *Phys. Med. Biol.,* vol. 61, pp. 663-82, 2016.

[53] E. Vlaisavljevich, K.-W. Lin, A. Maxwell, M. Warnez, L. Mancia, R. Singh, A. Putnam, B. Fowlkes, E. Johnsen, C. Cain and Z. Xu, "Effects of ultrasound frequency and tissue stiffness on the histotripsy intrinsic threshold for cavitation," *Ultrasound Med Biol,* vol. 41, no. 6, pp. 1651-1666, June 2015a.

[54] B. Hartmann, "Polymer sound speeds and elastic constants," Naval Ordnance Laboratory, White Oak, Silver Spring, MD, USA, 1972.

[55] J. Lochab and V. Singh, "Acoustic behaviour of plastics for medical applications," *Indian Journal of Pure & Applied Physics,* vol. 42, pp. 595-9, 2004.

[56] X. Zhang, G. E. Owens, C. A. Cain, H. S. Gurm, J. Macoskey and Z. Xu, "Histotripsy Thrombolysis on Retracted Clots," *Ultrasound Med. Biol.,* vol. 42, no. 8, pp. 1903-1918, August 2016.

5.7. Appendix – IEEE TUFFC Cover Art

IEEE TRANSACTIONS ON

ULTRASONICS, FERROELECTRICS, AND FREQUENCY CONTROL

A PUBLICATION OF THE IEEE ULTRASONICS, FERROELECTRICS, AND FREQUENCY CONTROL SOCIETY

NOVEMBER 2018 VOLUME 65 NUMBER 11 ITUCER (ISSN 0885-3010)

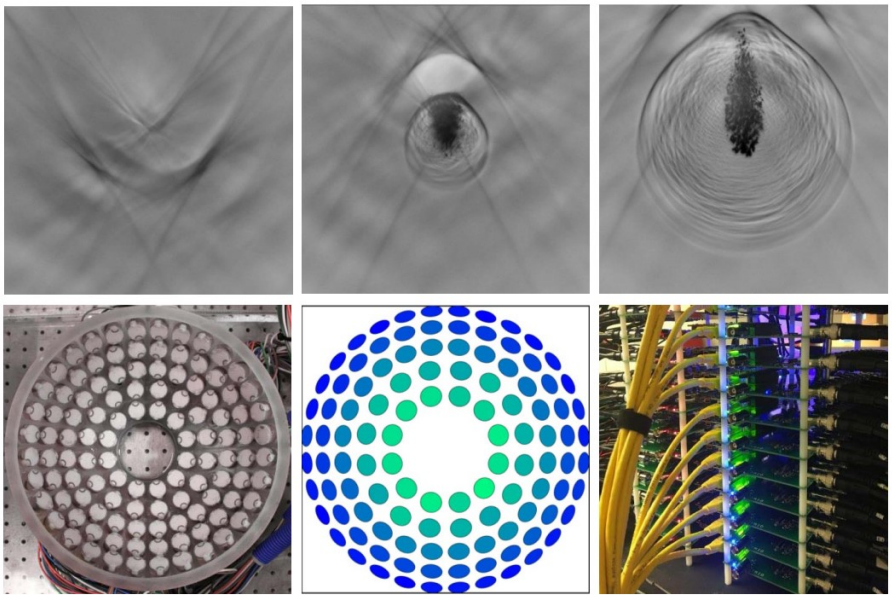

DOI http://dx.doi.org/10.1109/TUFFC.2018.2878075

CHAPTER 6

Summary and Future Work

6.1. Summary

This dissertation investigates acoustic feedback mechanisms for histotripsy that improve treatment efficacy by monitoring the extent of treatment progression and by improving the amount of acoustic energy delivered to the desired focal zone. In particular, this dissertation investigates the feasibility of histotripsy systems that are capable of both transmitting and receiving ultrasound and the ways in which receive-enabled histotripsy enables various feedback mechanisms. In general, this research focused broadly on methods to improve histotripsy efficacy by understanding more about each particular treatment such that even existing histotripsy systems can operate more efficiently and effectively. It is our hope that this work will open the door to the next generation of histotripsy therapy research in which quantitative ultrasonic methods are used to improve patient outcomes.

1) Technological Advancement: Histotripsy systems have classically been designed as transmit-only systems. Before the research in this dissertation, no receive-capable histotripsy systems existed, and it was thought that the implementation of such a system would likely be too expensive or technologically challenging to be practical. Furthermore, the use of additional imaging equipment such as B-mode imaging was a requirement for all *in vivo* histotripsy treatments because the histotripsy transducers themselves had no capability of self-monitoring. The work in this dissertation describes the iterative process of developing and testing experimental prototypes as we honed in on a continuously improved receive-capable histotripsy design. The

technological advancement of this dissertation concludes with a design of a state-of-the-art histotripsy system with receive capability that is able to drive a histotripsy transducer of at least 512 channels with receive capability on all channels. It is our hope that this design will enable new avenues of histotripsy research that were previously impossible and that this design will serve as a foundation upon which future researchers can design further improved systems while avoiding the pitfalls of failed early iterations.

2) Improved Histotripsy Treatment Monitoring: Two feedback mechanisms for monitoring the extent of histotripsy treatment progression were investigated in this dissertation. The first, bubble-induced color Doppler, was an existing feedback method that was invented by previous researchers in this group. The work in this dissertation furthered the understanding of this mechanism by understanding the relationship between the change in the BCD profile and the destruction of various components of tissue. *Ex vivo* bovine liver samples were treated with histotripsy, and BCD signals were acquired throughout 1000-pulse-per-location treatments. At select times throughout these treatments, therapy was halted and the tissue was fixed and histologically analyzed. It was found that the change in the BCD profile correlated linearly with the destruction of structural components in liver tissue. Importantly, it was found that the BCD profile did *not* correlate closely with cell lysing, which occurs much earlier than the destruction of structural components such as type I and type III collagen. Two conclusions can be drawn from these results. First, the oscillatory flow of tissue after the expansion and collapse of the histotripsy bubble cloud that is detected by Doppler ultrasound appears to be highly dependent upon the microstructure of tissue. Second, histotripsy destroys the cells within liver tissue earlier than it destroys the structural components. From the first conclusion, we hypothesize that BCD is highly dependent on the mechanical properties of tissue. This may indicate that BCD could be used to

understand the mechanical properties during histotripsy treatment in a similar fashion to the previous work done using ARFI for histotripsy monitoring [1] [2]. From the second conclusion, we find that histotripsy may be able to de-cellularize tissue while leaving the structural extracellular matrix at least partially in-tact. This would result in better patient outcomes due to improved healing. Further investigation of this phenomenon should be undertaken.

The second feedback mechanism, cavitation collapse time monitoring, was invented in the course of this dissertation. In Chapter 4, the change of collapse time was estimated with a hydrophone by measuring the time between the shockwaves emitted by the rapid expansion and collapse of histotripsy bubble clouds. It was found that 1) the collapse time can be measured acoustically, which was validated optically, 2) the collapse time increases throughout treatment in agarose tissue phantoms, and 3) the same trend is observed in the treatment of *ex vivo* bovine liver tissue. Furthermore, it was found that the collapse time tended to cease changing at the time when all hepatocytes were observed to be destroyed in the histological analysis of tissue destruction in Chapter 2. This suggests that cavitation physics are more dependent on cellular integrity in contrast to BCD, which appears to be more dependent upon the structural components in tissue. While BCD is an effective feedback mechanism for monitoring tissue integrity during histotripsy therapy, it requires additional imaging equipment. Monitoring the change of collapse time is easily performed with a passive ultrasonic receiver, and this method does not require large amounts of data nor processing power to perform in real-time. While this dissertation did not explore the ability for a receive-capable histotripsy system to monitor collapse time, this should be a relatively trivial extension given a receive-capable histotripsy system.

3) Aberration Correction for Soft Tissue: Prior to the work in this dissertation, little work had been done to address the issues associated with acoustic aberrations and their effects on

histotripsy treatment efficacy. In fact, much work had previously been done to show that histotripsy does not require aberration correction to be effective, e.g., [3] [4]. Furthermore, any pre-existing work in the field of histotripsy aberration correction had been focused on transcranial histotripsy and the challenges of correcting for aberrations due to the skull [5] [6]. However, as was shown in Chapter 5, soft tissue results in significant amounts of acoustic aberration that reduces the pressure delivered to the focus by over 50% through even a relatively thin sample of abdominal tissue.

To implement aberration correction for histotripsy through soft tissue, a receive-capable histotripsy array developed in Chapter 3 was used to collect shockwave data emitted by the rapid expansion of the histotripsy bubble cloud. The nature of this shockwave construct allowed it to be used as a point source guidestar, which can be used for aberration correction by estimating the overall phase variation due to tissue sound speed variations, which thereby allows the implementation of time reversal acoustics. Using this noninvasive method, over 20% of the lost pressure due to phase aberrations was recovered. This was the first time that a noninvasive method was used for histotripsy aberration correction, as opposed to an invasive method in which an ultrasonic receiver, e.g., a hydrophone, is placed within a patient and these phase delays are measured directly.

6.2. Future Work

6.2.1 Improved Receive-Capable Histotripsy Arrays

While the receive-capable histotripsy arrays discussed in this dissertation are the current state-of-the-art from both a transmit and receive perspective, there is always room for improvement. Primarily, we propose three future improvements to these systems. First, the FPGA/SoCs used in these systems were embedded on a development platform that provided

simple integration of multiple different hardware units including memory, Ethernet peripherals, FPGA I/O, and USB programming. This is all not to mention the various supporting hardware that is required to effectively run the FPGA/SoC chips before data handling even begins. However, these benefits also come with downsides. The main downside is that using this platform reduces the overall capabilities of the FPGA/SoC chip. The DE10-Nano comes with approximately 72 GPIO pins with ten usable LVDS pairs, but the specific Cyclone V SoC chip from Intel actually has 224 GPIOs with 28 LVDS pairs. While the engineering effort required to develop our own circuit boards that are able to support the Cyclone V SoC chip without the DE10-Nano would be substantial, the benefits would be more flexible, lighter weight systems that are able to control more than 8 channels per FPGA.

The second proposed improvement to these systems would be to provide better receiver bandwidth. The histotripsy elements are relatively narrowband receivers, but the real problem behind the receive bandwidth actually lies with the driver. While the driver used in this system uses a transformer rather than an inductor, as was used in previous drive systems, the secondary coil in the transformer essentially acts as an inductor and significantly reduces the bandwidth outside the driver frequency. Due to the fact that the receive circuitry is directly coupled to the driver, this also reduces the bandwidth of the receiver. Improved bandwidth would improve the measurement of ACE signals, which are broadband shockwaves. This would likely improve the aberration correction methods discussed in Chapter 5.

The third proposed improvement to these systems could potentially eliminate the need to increase the driver bandwidth. Typical ultrasound imaging systems use an electronic device called a transmit-receive switch (T/R switch) or duplexer. Using a T/R switch allows you to switch the transducers connection between the transmit and receive circuitry, which means that the transducer

is only connected to the driver circuit when the user wants to emit sound from the transducer, and the transducer is only connected to the receive circuitry when the user wants to receive sound. Using this method would completely isolate the inductance of the driver from the receiver and would drastically improve bandwidth. However, the T/R switches used in medical ultrasound imaging do not switch between several thousand Volts. Therefore, a custom T/R switch would likely have to be built for this application.

6.2.2 Automatic Treatment Monitoring and Completion

The work discussed in chapters 2 and 4 aimed at developing acoustic feedback mechanisms that monitored the extent of treatment in real time. Additionally, the work in Chapter 4, specifically, was aimed at developing a method that would allow a receive-capable histotripsy array to self-monitor treatment completion. While the receive-capable arrays of Chapter 3 were not yet complete at the time of the collapse time monitoring study, the technology now exists for histotripsy arrays to determine the extent of treatment in real time and then halt treatment upon completion without human intervention. If successful, a method that could stop treatment as soon as treatment is completed could improve patient outcomes by reducing the amount of over-treating, thus reducing post-op healing times. Implementing real-time treatment monitoring and completion would take histotripsy one step further towards clinical translation.

6.2.3 Real-Time Bubble Cloud Tracking

An obvious application of receive-capable histotripsy arrays is bubble cloud location tracking and detection of incident cavitation in unwanted places. Accurate and precise measurements of bubble cloud location will be required for clinical translation due to the

potentially harmful effects of cavitation in unwanted places. By tracking the locations of initiated bubble clouds, one could then cross-correlate these locations with a tissue destruction feedback method, e.g., collapse time monitoring, and then map the estimated dosage to the target volume. Additionally, having the ability to track bubble cloud movement could also enable the tracking of breathing motion, which is another important task for clinical translation.

6.2.4 Advanced ACE Aberration Correction Techniques

While the ACE-based aberration correction methods described in Chapter 5 were successful in that they significantly increased the amount of pressure delivered to the focus and increased bubble cloud size, there is still much room for improvement. When compared to the gold standard hydrophone method, which recovered over 50% of the overall attenuation and approximately 100% of the attenuation due to phase-based aberration, the ACE-based method clearly has not yet been perfected. We see several avenues for improvement. First, better receive systems with higher bandwidths, better resolution, and higher sampling frequencies will undoubtedly result in better aberration correction using the exact same method. Through certain portions of tissue, the ACE signals were drastically attenuated to the point where they were just above the noise floor of some of the histotripsy elements. Increasing the overall sensitivity of the system would result in more accurate shockwave arrival time estimates and therefore better aberration correction phase calibrations. Second, we foresee several more advanced algorithms for processing the ACE data to acquire an optimal phase calibration. In particular, we hypothesize that a deep learning algorithm could be trained to automatically identify an optimal phase calibration. Using the existing receive-capable histotripsy arrays, artificial amounts of aberration could be introduced by applying phasing to steer the array to random locations within its steering range.

The known phase calibration could then be used to train the neural network to automatically identify the proper phasing to steer the array back to the focus. In this way, the ACE aberration correction method could be made to be robust against a multitude of tissue types and treatment scenarios, thus, again, bringing histotripsy much closer to clinical translation.

6.3. References

[1] T.-Z. Wang, T. Hall, Z. Xu, J. Fowlkes and C. Cain, "Imaging feedback of histotripsy treatments using ultrasound shear wave elastography," *IEEE Trans. Ultrason., Ferroelect., Freq. Control,* vol. 59, no. 6, pp. 1167-81, 2012a.

[2] T.-Z. Wang, T. Hall, Z. Xu, J. Fowlkes and C. Cain, "Imaging feedback for histotripsy by characterizing dynamics of acoustic radiation force impulse (ARFI)-induced shear waves excited in a treated volume," *IEEE Trans. Ultrason., Ferroelect., Freq. Control,* vol. 61, no. 7, pp. 1137-1151, 2014.

[3] Y. Kim, T.-Y. Wang, Z. Xu and C. Cain, "Lesion generation through ribs using histotripsy therapy without aberration correction," *IEEE Trans. Ultrason. Ferroelec. Freq. Control,* vol. 58, no. 11, pp. 2334-43, 2011.

[4] J. Sukovich, Z. Xu, Y. Kim, T.-S. Nguyen, A. Pandey, T. Hall and C. Cain, "Targeted lesion generation through the skull without aberration correction using histotripsy," *IEEE Trans. Ultrason. Ferroelectr. Freq. Control,* vol. 63, no. 5, pp. 671-682, 2016.

[5] T. Gerhardson, J. Sukovich, A. Pandey, T. Hall and C. Cain, "Catheter hydrophone aberration correction for transcranial histotripsy treatment of intracerebral hemorrhage: proof-of-concept," *IEEE Trans. Ultrason. Ferroelect. Freq. Control,* vol. 64, no. 11, pp. 1684-97, 2017.

[6] J. Sukovich, Z. Xu, T. Hall, J. Macoskey and C. Cain, "Transcranial histotripsy acoustic-backscatter localization and aberration correction for volume treatments," in *173rd Meeting of the Acoustical Society of America*, Boston, MA, 2017.

Appendix

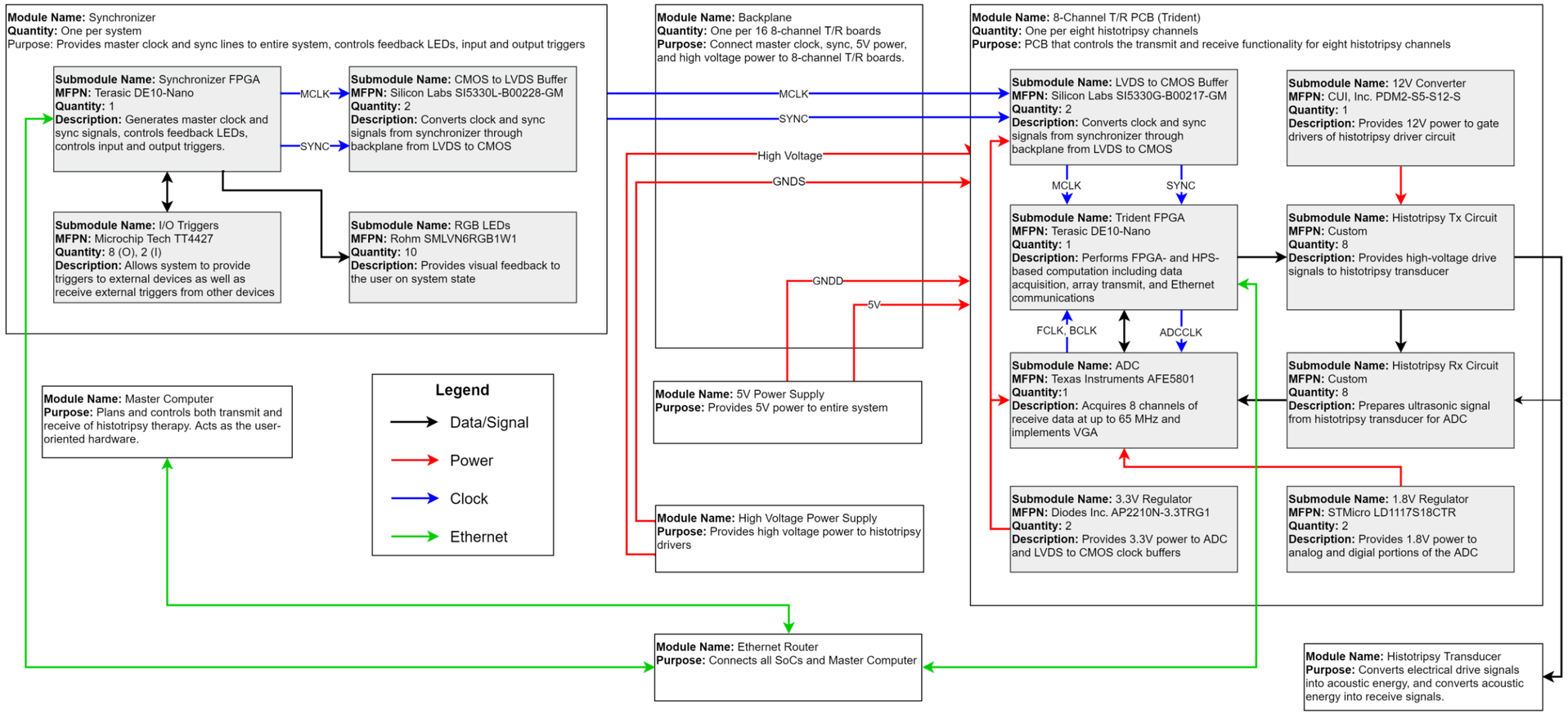

Figure A.1: Integrated transmit-and-receive-capable histotripsy system hardware block diagram.

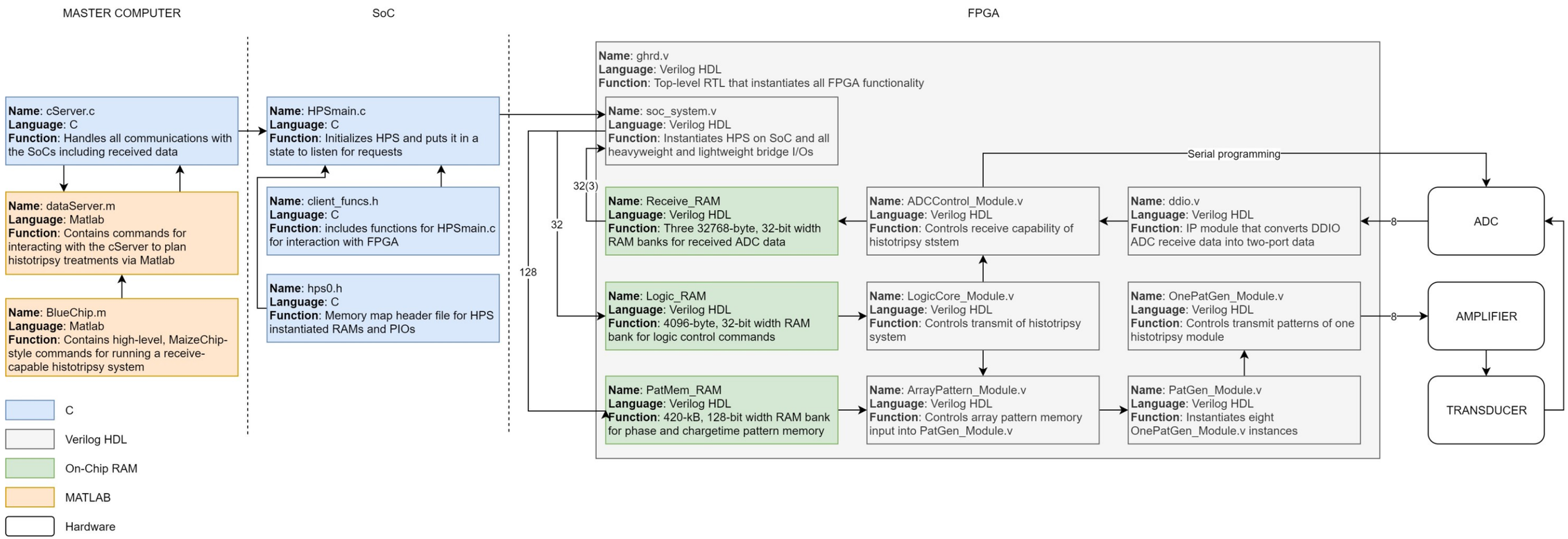

Figure A.2: Integrated transmit-and-receive-capable histotripsy system software block diagram

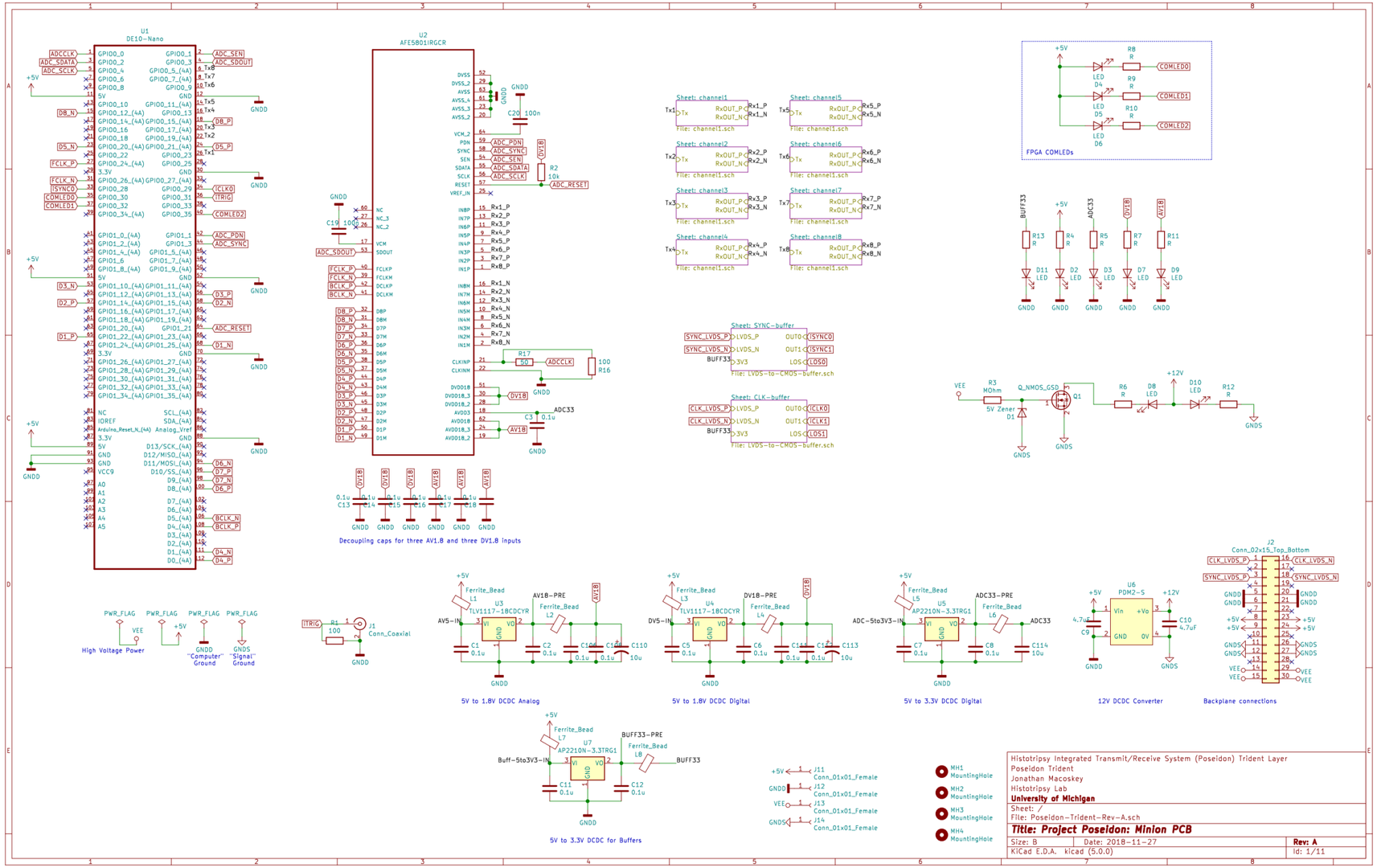

Figure A.3: Top-level electrical schematic for the 8-channel transmit-and-receive-capable driving system (Poseidon Trident)

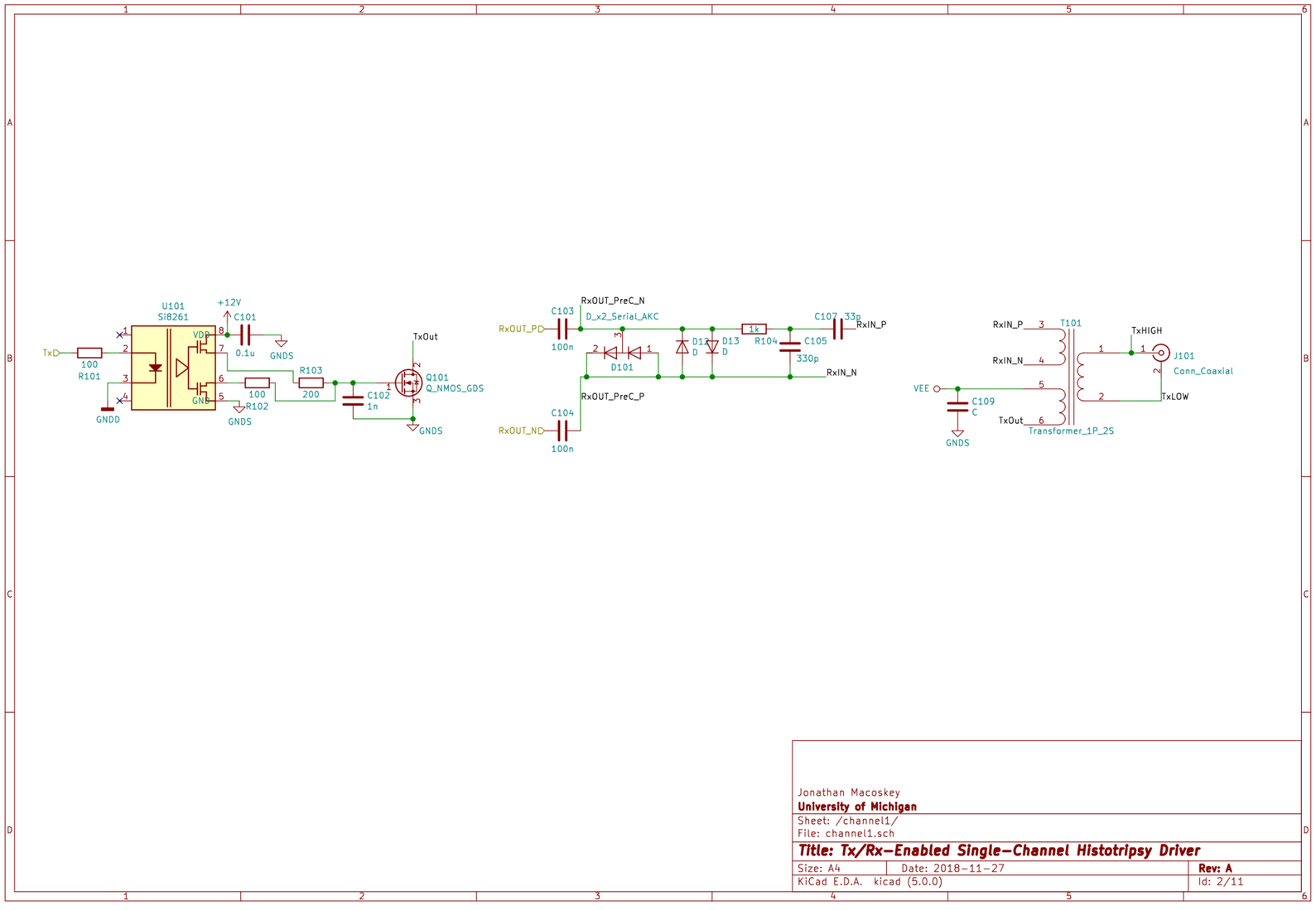

Figure A.4: Electrical schematic for the driver and receiver analog electronics for the Poseidon system. Each Trident board incorporates three of these circuits on one PCB.

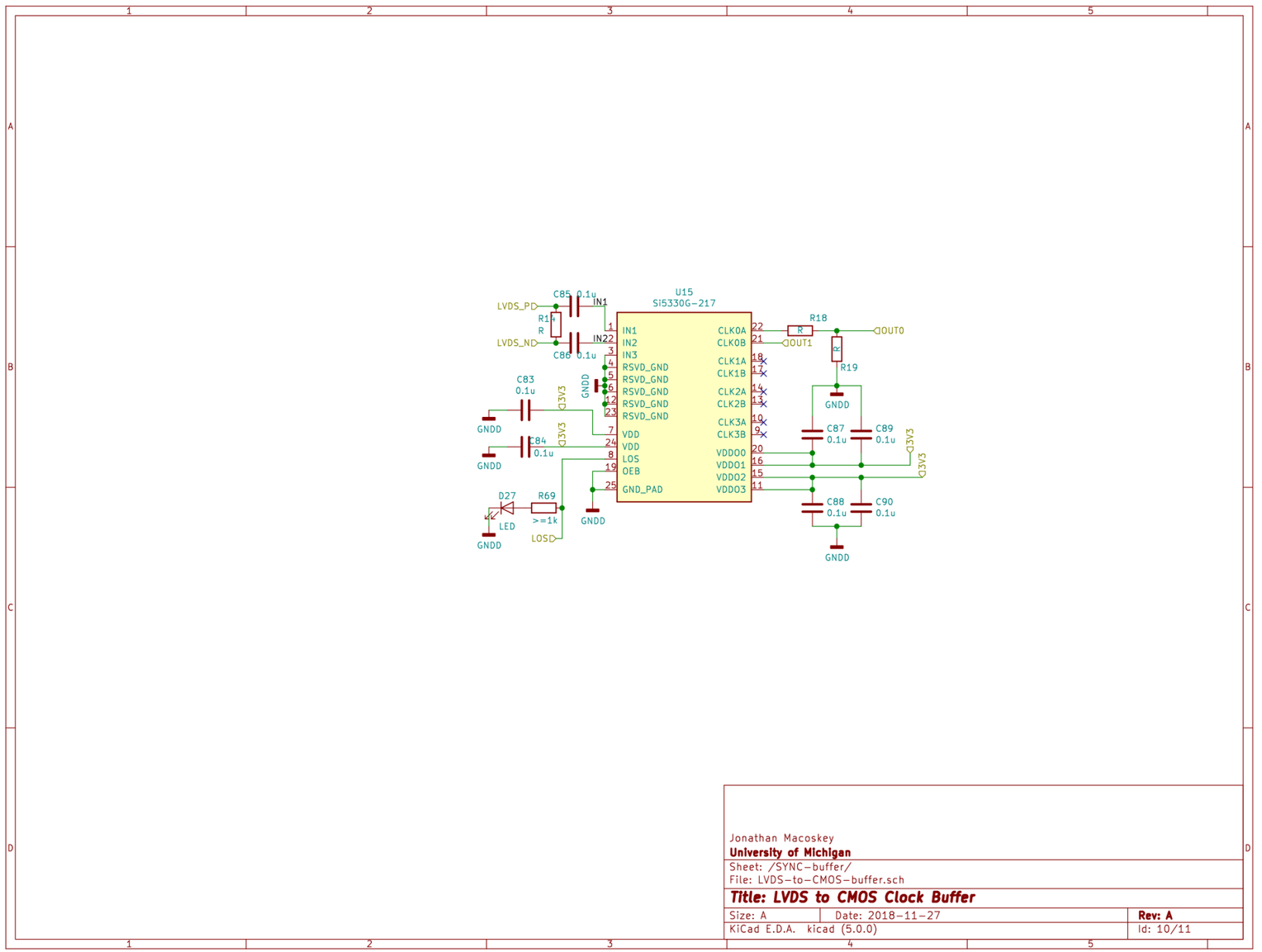

Figure A.5: Clock buffer schematic used for Poseidon system. Each Trident board uses two of these buffers to convert the CLOCK and SYNC lines from LVDS to CMOS.